Global Emission Inventory

A Revision of Global Emission Inventory Models for Climate Impact Analysis

Najib Jahjah

Delft University of Technology

TU Delft

Global Emission Inventory

A Revision of Global Emission Inventory Models for Climate Impact Analysis

by

Najib Jahjah

to obtain the degree of Master of Science
at the Delft University of Technology,
to be defended publicly on Friday August 29, 2025 at 10:00 AM.

Student number: 4653351

Thesis committee:

Prof. dr. A. Gangoli Rao,	TU Delft, chair
Dr. F. Yin,	TU Delft, supervisor
Dr. J. Sun	TU Delft, examiner

Cover: Photo by Johannes Krupinski on Unsplash (Modified)
Style: TU Delft Report Style, with modifications by Daan Zwaneveld

An electronic version of this thesis is available at `http://repository.tudelft.nl/`.

TU Delft

Abstract

The aviation sector has set goals to reduce its carbon footprint, as the industry continues to grow. To capture the climate impact of millions of flights, climate models play a crucial role in this task. However, these climate models depend on information about the concentration and distribution of emissions around the globe. To provide such data, bottom-up emission inventories are used. These inventories model aircraft flight performance and engine emission characteristics to provide the best estimate of the geographical distribution of emissions due to aviation.

The research presented in this thesis aims to critically evaluate and improve existing implementations of global aviation emission inventories, with the ultimate goal of achieving more representative estimations of aircraft emissions and their distribution. The goal should be achieved without compromising on computational efficiency and the flexibility of the model. This work builds upon an existing emission inventory.

In order to achieve the goal of this study, revisions to the information, performance and emission models are incorporated. The first revision involves a more accurate representation of the actual engine equipped for each flight analysed. Next, flight trajectory correction factors (lateral inefficiency) are improved by using data provided in literature, derived from a large set of ADS-B trajectory data. Furthermore, the latest version of EUROCONTROL's Base of Aircraft Data (BADA) performance model is implemented for all the aircraft which it covers (89% of total flown distance). For emission modelling, the Boeing Fuel Flow Method 2 (BFFM2) is kept for gaseous emissions; however, an updated method (MEEM), validated on a large set of engine manufacturer data and more recent measurement campaigns, is utilised for nvPM estimates.

Compared to existing global inventories for 2019, the updated model estimates total fuel burn at 250 Tg, slightly lower than the earlier estimate (254 Tg) and significantly below estimates by Teoh et al. (283 Tg) and Quadros et al. (297 Tg). On a per-kilometre basis, however, the fuel burn estimate is 2% lower than Rik Kroon's but 9.6% higher than Teoh et al. The nitrogen oxides (NO_x) emission index closely aligns with benchmarks by Teoh et al. and Quadros et al., differing by less than 2.5%, yet is 11% lower than Rik Kroon's due to performance model corrections. For nvPM emissions, notable discrepancies arise: mass emission estimates are higher by 62% and 39% compared to Rik Kroon and Quadros et al., respectively, but 43% lower than Teoh et al. Conversely, nvPM number emission estimates exceed those by Teoh et al. and Quadros et al. by approximately 60% and 54%, respectively. Geographically, emission hotspots align with previous studies, though data limitations cause under-representation in certain southern hemisphere routes, highlighting areas for future improvement.

Sensitivity analysis revealed that the performance model results are highly sensitive to the parameters used to determine cruise altitude and initial fuel mass estimate, with up to ±4% changes in nvPM emissions and fuel burn observed for heavy-weight aircraft. The uncertainty analysis using Monte Carlo simulations showed total uncertainties of ±9% for fuel consumption and emission indices uncertainties ranging from ±8% for NO_x to ±40% for nvPM number and ±95% for nvPM mass, reflecting the significant impact of methodological assumptions and limited validation data on nvPM emissions.

The thesis concludes by confirming that the updates provided lead to an improvement in the estimation of the quantity and distribution of aviation emissions. Limitations related to the coverage of annual flights, the estimation of the take-off mass, and the uncertainty related to nvPM emissions are also identified. This work can serve as a baseline for future work in those aspects.

Acknowledgements

This thesis marks the culmination of my educational journey at the TU Delft. Along the way, I have not only acquired valuable knowledge and skills essential to becoming an engineer, but also, beyond academics, this journey has taught me the value of perseverance, how to learn from setbacks, and how to adapt to challenges, lessons that will stay with me far beyond my professional life. Thankfully, from the start of my Bachelor's to this day, I have not had to go through this journey alone, and I would like to thank those who have been a part of it.

First and foremost, I would like to thank my daily supervisor, Dr. Feijia Yin, and the chair, Prof. dr. Arvind Gangoli Rao, for giving me the opportunity to work on a topic of great interest to me, allowing me the time and space to explore ideas, and most of all, providing invaluable guidance to steer me in the right direction. I would also like to thank Harjot Saluja, whose presence at all my meetings and willingness to assist whenever needed, at every step of the thesis, helped me deliver my best work.

Next, I would like to thank my family, without whom my journey at the TUDelft would never have been possible. They provided me with the support and trust I needed to complete this degree, while giving me the space to go through this journey at the pace that suited me best.

I owe special thanks to my friends, some of the most important companions on this journey, who were by my side almost every day. I would like to begin with those who started this journey alongside me during our bachelor's studies: Prateek, Matt, Keval, Benji, and Dani. Together, we shared countless study sessions and projects, as well as great times outside of university. Along the way, I was fortunate to meet many others, including Farouk, Luc, Eash, Alexis, and Evan, whose presence both in and out of university made this time more memorable. I am especially grateful to Farouk and Prateek, with whom I shared many ups and downs along this journey, but their constant support has kept me going to this day. No acknowledgements would be complete without mentioning my housemates, some of whom I've already named. But I'd like to add special thanks to Arjun, Joanna, Letizia, and Fernando, for all the great moments we've shared together during this journey.

Last, but by no means least, I would like to thank Eleni. Thank you for being there for me every day, both at my best and my worst. The moments we shared away from university helped me let go of stress, find joy in the little things, and truly recharge, reminding me of the importance of balance during this journey. During my time at university, through moments of stress, self-doubt, and long hours of work, you provided me with a constant source of emotional support and motivation, reminding me to believe in myself and keep going. Είμαι αιώνια ευγνώμων.

Najib Jahjah
Delft, August 2025

Contents

List of Figures

List of Tables

Nomenclature

Abbreviations

Abbreviation	Definition
ADS-B	Automatic Dependent Surveillance–Broadcast
AFR	Air-to-Fuel Ratio
ATR	Average Temperature Response
AIAA	American Institute of Aeronautics and Astronautics
AIC	Aviation-Induced Cloudiness
AMOC	ATFM Modelling Capability
ATFM	Air Traffic Flow Management
BADA	Base of Aircraft Data
BC	Black Carbon
BFFM	Boeing Fuel Flow Method
BPR	Bypass Ratio
CAS	Calibrated Airspeed
CCD	Climb Cruise & Descent
CH_4	Methane
CO	Carbon Monoxide
EASA	European Union Aviation Safety Agency
EDB	Engine Databank
ETMS	Enhanced Traffic Management System
EI	Emission Index
FAA	Federal Aviation Administration
GMD	Geometric Mean Diameter
GWP	Global Warming Potential
HC	Hydrocarbons
H_2O	Water Vapour
KDE	Kernel Density Estimate
ICAO	International Civil Aviation Organisation
IPCC	Intergovernmental Panel on Climate Change
ISA	International Standard Atmosphere
LHV	Lower Heating Value
LTO	Landing and Take-Off
MTOM	Maximum Take-Off Mass
NO_x	Nitrogen Oxides
nvPM	non-volatile Particulate Matter
O_3	Ozone
OEM	Operating Empty Mass
PDF	Probability Density Function
PM	Particulate Matter
RF	Radiative Forcing
ROC	Rate of Climb
ROCD	Rate of Climb/Descent
TAS	True Airspeed
TEM	Total Energy Model
TOM	Take-Off Mass
TSFC	Thrust Specific Fuel Consumption

Symbols

Symbol	Definition	Unit
C	Concentration	[kg/m^3]
C_D	Drag coefficient	[-]
C_L	Lift coefficient	[-]
C_T	Thrust coefficient	[-]
D	Drag	[N]
EI	Emission index	[g/kg fuel]
FF	Fuel flow	[kg/s]
L	Lift	[N]
M	Mach number	[-]
M_f	Fuel mass	[kg]
M_{payload}	Payload mass	[kg]
Q	Specific exhaust volume	[m^3/kg]
R	Universal gas constant	
T	Thrust	[N]
T_{amb}	Ambient temperature	[K]
T_{fl}	Flame temperature	[K]
T_s	Surface temperature	[K]
T_3	Combustor inlet temperature	[K]
T_4	Turbine inlet temperature	[K]
V	Velocity	[m/s]
W	Weight	[N]
a	Speed of sound	[m/s]
d	Distance	[km]
g	Gravitational acceleration	[m/s^2]
h	Altitude	[m]
k_{slm}	System loss correction factor	[-]
m	Mass	[kg]
p	Pressure	[Pa]
Π	Pressure Coefficient	[-]
α	Angle of attack	[rad]
β	Bypass ratio	[-]
γ	Flight path angle	[rad]
γ	Ratio of specific heats	[-]
δ	Pressure ratio	[-]
η	Efficiency	[-]
θ	Temperature ratio	[-]
λ	Climate sensitivity parameter	[-]
π_{00}	Operating pressure ratio	[-]
ρ	Air density	[kg/m^3]
σ	Standard deviation	[-]

1

Introduction

The aviation industry has experienced exponential growth over the past few decades, becoming a crucial component of the global transportation system. In 2019, commercial airlines carried over 4.5 billion passengers worldwide [22]. Although the demand for air travel took a hit due to the COVID-19 pandemic, with a 66% reduction in revenue passenger kilometre (RPK) in 2020 [22], the demand in late 2023 had reached 93% of 2019 pre-covid levels [23]. Furthermore, air travel is projected to double by 2040 relative to 2019 [23]. This growth has also resulted in significant environmental concerns, particularly related to emissions, which will continue to grow if the appropriate actions are not taken. Aviation emissions contribute to approximately 2-3% of global CO_2 emissions [31] and are responsible for releasing other pollutants such as NO_x and particulate matter, which exacerbate air pollution and climate change. As the demand for air travel continues to rise, it is imperative to develop and implement effective strategies to mitigate the environmental impact of aviation.

For these strategies to be implemented effectively, there is a need for the accurate and comprehensive accounting of emissions, achieved through emission inventories. Emission inventories are essential tools that compile a database for the amount and types of pollutants released into the atmosphere by various sources, in this case, aviation. As early as the 1970s, attempts to quantify emissions began with research measuring pollutants from aircraft engines to understand their contribution to local air quality [48]. However emission inventories as we know them have only been developed since the 1990s [4], when the focus shifted more to global climate change and CO_2 and NO_x emissions [32]. These inventories provide the foundation for understanding emission patterns, assessing environmental impacts, and formulating regulatory policies. Thus, enhancing the precision and reliability of these inventories is of paramount importance.

The research presented in this thesis aims to critically evaluate and improve the existing implementations of aviation emission inventories. By identifying and addressing gaps in the current model, this research seeks to achieve more representative emission estimations and their geographical distribution. The thesis emphasises computational efficiency and flexible frameworks to facilitate reproducibility and adaptability in future research. The report begins by providing a detailed background on emissions, climate impact, emission inventories, and associated modelling approaches in Chapter 2. Next, Chapter 3 highlights the research gaps identified in the various models through the use of an ideal emission inventory as benchmark. Once the gaps are identified, Chapter 4 outlines the research goals and methodologies, including sensitivity and uncertainty analyses. The next chapters focus on answering the research questions posed in Chapter 2. The first of these is Chapter 5, which discusses the sensitivity of the various inputs to the performance model. Chapter 6 presents the inputs which propagate uncertainty through the model, and presents the uncertainty range for the various emissions. Finally, Chapter 7 provides the final results of the updated emission inventory.

2

Background

This chapter gives an overview of aircraft emissions and their climate effects, as well as approaches to quantify them. An overview of the various species emitted by aviation and their climate impact will be discussed in section 2.1. Bottom-up emission inventories, including how they are generally built and their main purpose, will be discussed in section 2.2.

2.1. Emissions and Climate Impact

Air travel contributes to atmospheric pollution in different ways. Indeed, the combustion of jet fuel has a variety of byproducts stemming from actual combustion. These various byproducts are individual species of emissions, and each affects the atmosphere in different ways, ultimately leading to an imbalance in the planet's temperature. This change happens through radiative forcing of certain components, which is explained later in this section. Figure 2.1 gives an overview of the aircraft emissions and their climate impact [32]. More details on the specific species and their effect on the atmosphere are discussed further in this section.

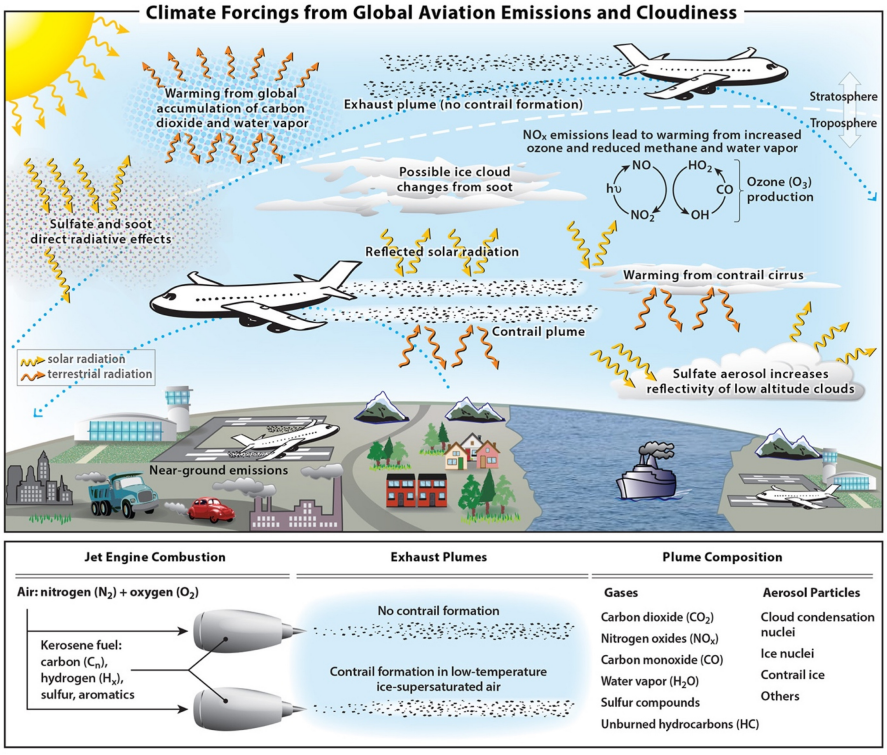

Figure 2.1: An illustration of the various byproducts of commercial aircraft combustion, the atmospheric processes they are involved in and their impacts. Figure taken from Lee et al. [31].

2.1.1. Climate Metrics

To begin with, it is important to understand the concept of radiative forcing. Firstly, when a given emission is produced, it changes the concentration of this species in the atmosphere, so it is perturbed. This causes a change in the radiation flux in the atmosphere, referred to as radiative forcing. This radiative forcing occurs in different ways, for example, contrails induce imbalances in reflection and absorption of radiation, whereas Nitrogen Oxides (NO_x) form a complex chemistry chain resulting in a change in radiative flux. Radiative forcing is often used to assess the climate change effect of a given species. A relation exists between the change in global average equilibrium surface temperature (ΔT_s) and the radiative forcing (RF) of the species with a climate sensitivity parameter (λ), Equation 2.1 [11].

$$\Delta T_s \approx \lambda \cdot RF \tag{2.1}$$

Currently, a more commonly used measure is the Effective Radiative Forcing (ERF). Effective radiative forcing extends the concept of RF by including the rapid adjustments in the atmosphere and surface that occur in response to a forcing agent. ERF provides a more accurate representation of the impact of a forcing agent on the Earth's energy balance because it accounts for all tropospheric and land surface adjustments, as opposed to only stratospheric adjustments in the case of RF. However, determining ERF is more complicated and requires the integration of climate models [28].

There also exist time-integrated climate metrics, which account for the evolution of the climate impact of an emission over a given time horizon rather than only its instantaneous effect. This is important because different species not only cause varying levels of radiative forcing but also have greatly differing atmospheric lifetimes [8].

The most commonly used by the IPCC is the Global Warming Potential (GWP), defined as the time-integrated radiative forcing of the emission of a given species relative to that of CO_2 over a chosen time horizon [8]. However, for aviation, the Average Temperature Response (ATR) has been found to be more suitable [33]. Unlike GWP, which integrates radiative forcing, ATR integrates the global mean surface temperature change over the time horizon, as temperature change is a more direct measure of global climate behaviour [8]. Megill et al. [33] perform an extensive trade-off highlighting the benefits of ATR over GWP.

2.1.2. Species of Emissions

As shown in Figure 2.1, the actual combustion of jet fuel leads to byproducts which have an impact on climate change.

To begin with, Carbon Dioxide (CO_2) is one of the most important greenhouse gases, as it is the most emitted by volume and has a long lifetime [27]. The exact lifetime is complicated as (CO_2) is part of multiple processes, but the main sinks are the biosphere and ocean, which, according to the IPCC, remove 50% within 30 years, however the rest may take centuries, with almost 20% remaining in the atmosphere for a millennium [26]. For this reason, CO_2 is often used as a reference for other greenhouse gases or emissions, which are sometimes quantified as CO_2 equivalent.

Nitrogen Oxides (NO_x), including Nitric Oxide (NO) and Nitrogen Dioxide (NO_2), are not direct greenhouse gases but significantly impact atmospheric processes that influence climate change. In the short term, NO_x contributes to the formation of tropospheric Ozone (O_3), a greenhouse gas, through photolysis of NO_2. In the long term, however, it leads to a reduction in stratospheric ozone and water vapour, stemming from the breakdown of Methane (CH_4). It also affects the atmospheric lifetime of methane, another potent greenhouse gas with a lifetime in the order of years [26], by altering the chemical pathways that break down methane in the atmosphere. Overall, NO_x plays a critical indirect role in climate dynamics by leading to a positive radiative forcing [32].

Water vapour (H_2O) is also a greenhouse gas involved in multiple processes affecting aerosols, clouds and contrails. H_2O itself is a greenhouse gas, which leads to positive radiative forcing, higher than that of CO_2 and CH_4. However, it is unique in the sense that it can condense and precipitate, and thus has a limited residence time of around ten days [53]. This contributes to cloud and contrail formation. These have both a cooling and warming effect on the climate, although the warming effect is thought to be stronger [31]. The cooling effect, also known as the albedo effect, comes from the reduction in short-wave radiation reaching Earth's surface due to the cloud/contrail cover. The greenhouse effect comes from the trapped long-wave radiation unable to escape the low Earth atmosphere [49].

Non-volatile Particulate Matter (nvPM) refers to the non-gaseous product of incomplete combustion, often referred to as soot and Black Carbon (BC) [6]. The term nvPM is the current regulatory term and measurement standard, put into effect in 2017 [51]. It is almost entirely composed of BC, thus the terms are often used interchangeably in research (with BC used more frequently prior to 2017) [16]. These particles have a direct positive radiative forcing effect, as they absorb short-wave radiation (solar radiation) [31]. Particulate matter emissions also have indirect RF impacts, as these particles provide what is called a condensation nucleus for water vapour particles, which facilitates contrail and cloud formation, the effect of which is already discussed in this section [19].

Besides the global warming potential of many of these emissions, there are also health considerations. Some of the byproducts of aircraft engine combustion have various impacts on human health:

- **Soot (Black Carbon):** Soot particles are tiny particulates that can penetrate deep into the lungs and bloodstream, exacerbating respiratory and cardiovascular diseases. They are also carcinogenic and can contribute to conditions like asthma and bronchitis [42].
- **Sulfur Oxides (SOx):** Exposure to sulfur oxides can irritate the respiratory system and exacerbate pulmonary diseases, particularly in children and the elderly. SOx can also react in the atmosphere to form fine particulate matter and sulfate aerosols, which have further health impacts [63].
- **Unburned Hydrocarbons (UHC)**: Similary to soot and sulfur oxides, unburned hydrocarbons include compounds that could contribute to chronic respiratory diseases by irritating the respiratory tract and reducing lung function. Compounds such as benzene, an aromatic hydrocarbon, have been linked to numerous blood cancers, including acute myeloid leukemia and acute nonlymphocytic leukemia [21].
- **Carbon Monoxide (CO):** CO reduces the blood's ability to carry oxygen, leading to reduced oxygen delivery to the body's organs and tissues. It is particularly harmful to people with cardiovascular diseases, and high levels of exposure can be lethal [62].
- **Nitrogen Oxides (NO_x):** NO_x contributes to the formation of ground-level ozone and fine particulate matter, both of which are harmful to respiratory health. NO_2 exposure can lead to conditions such as asthma, bronchitis, and can reduce lung function [34].

2.1.3. Climate Impact

A very brief overview of the climate impact of aviation can be seen in Figure 2.2 [31]. It illustrates the effective radiative forcing of various species of emissions. As discussed earlier, and shown in Equation 2.1, the change in temperature is dependent on this radiative forcing, and the climate sensitivity parameter of the species in question.

Although the confidence levels may be low in some cases, this clearly shows an overall global warming effect on the planet. Indeed, even when taking the minimum values of the uncertainties, this is still the case, which illustrates the importance of climate research in the field of aviation.

Another important aspect to consider when assessing aviation's non-CO_2 climate effects is the strong dependency on flight level. This is commonly expressed with an altitude-specific forcing factor $s_i(h)$ that rescales the radiative forcing (RF) per unit emission of species i relative to a reference case ($s_i = 1$). While CO_2's RF per kilogram of fuel is effectively independent of altitude, several short- and long-lived species show pronounced altitude sensitivity, as illustrated in Figure 2.3 [8].

This illustrates the importance of not only accurately estimating the quantity of various emission species, but also their altitude and location.

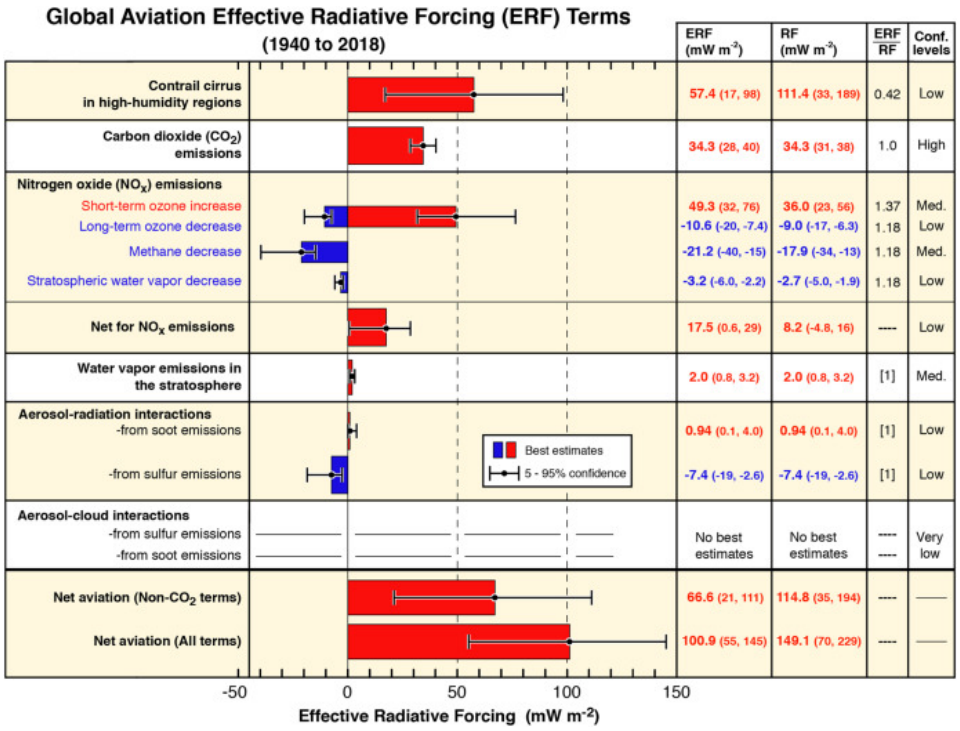

Figure 2.2: Schematic illustration of the global radiative forcing of various emitted species from air travel. Figure taken from Lee et al. [31]

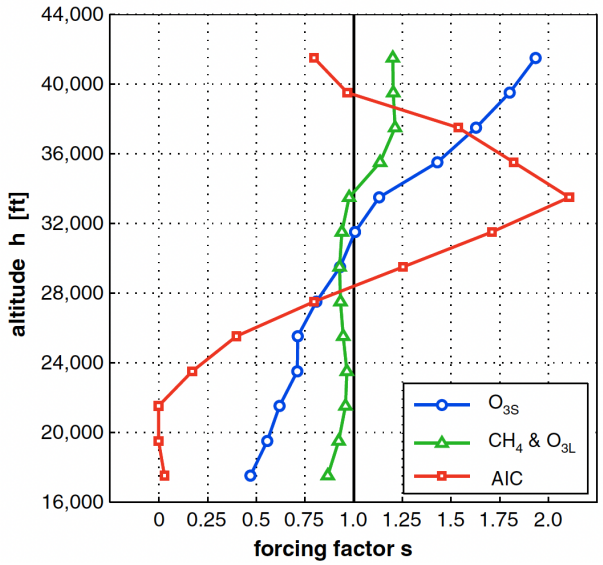

Figure 2.3: Altitude dependence of forcing factors $s(h)$ for short-lived ozone from NO_x (O_{3S}), the long-lived methane+ozone response ($CH_4 + O_{3L}$), and Aviation-Induced Cloudiness (AIC). Taken from Dallara et al. [8].

2.2. Emission Inventory

An emission inventory is a comprehensive database that describes the emissions of pollutants released into the atmosphere. It details the types and amounts of pollutants emitted over a specific period and geographic area, serving as a crucial tool for environmental management and policy-making. Emission inventories are fundamental for tracking pollution trends, informing air quality and climate models, supporting the development of targeted emission reduction strategies, and assessing progress towards environmental regulations and climate change mitigation goals. Inventories are built for numerous industries and can be top-down or bottom-up. In this research, the focus is on 3D (longitude, latitude, and altitude) bottom-up inventories for global civil aviation.

Such emission inventories have been an area of research for over three decades, starting with NASA's emission inventory for the year 1992, which analysed NO_x, CO and HC [4]. Over the years research has brought about new and updated emission inventories. AERO2k in 2004 [17] and a tool by Owen et al. in 2010 [38] were used to analyse the emissions for forecasts for 2025 and for IPCC scenarios for 2050 and 2100, respectively. In more recent years, research at the TUDelft has led to an emission inventory for the years 2017 to 2020, also including insight into the COVID-19 pandemic [44]. One of the most up-to-date emission inventories (a 4-D inventory as it includes a time component) available was developed by Teoh et al. in 2023 [60], and includes an extensive analysis of emissions for flights from 2019 to 2021, also incorporating insights from the COVID-19 pandemic. The latest in the recent series of emission inventories was developed in 2023 and published in 2024 by Klener et al. [29]. In this inventory, similar to that of Quadros et al. and Teoh et al., the year 2019 is analysed, but in this case, the emphasis is put on the domestic and international flights based on the departure country. The countries analysed are those that have ratified the United Nations Framework Convention on Climate Change (*UNFCCC*). In some cases, these countries don't frequently disclose their share of global aviation emissions; thus, this paper attempts to shed light on the matter of national share of global aviation emissions using a high-resolution emission inventory. Finally, the emission inventory developed by Rik Kroon for the year 2019 will serve as the base model for this study. This inventory is characterised by its high computational efficiency when compared to contemporary emission inventories [30].

Alongside the base inventory used for this study, the inventories developed by Teoh et al.[60] and Quadros et al. [44] will also be used as references, as they pertain to the same year. These inventories are built up of three main models: an information model; a performance model; and an emission model, which will be discussed here in more detail.

2.3. Information Models

Information models involve gathering air traffic data, including flight schedules, trajectories and aircraft information. The data is usually sorted and processed such that incomplete information or duplicate information is either completed or deleted. For trajectories, historically only air traffic schedules were used, where origin and destination airports are provided. This data has been available through OAG Aviation Worldwide ltd.[1] for decades, and used in numerous inventories, from NASA in 1996 [4] to Simone et al. in 2013 [54] and Quadros et al. in 2022 [44]. The trajectory is then assumed as the great circle distance between these two points [4]. Over time these began to be complemented by actual trajectory data, when available, to better assess the flight position, altitude, and time, first with radar such as the Enhanced Traffic Management System (ETMS) and AMOC, an air traffic flow management tool, then with ADS-B (Automatic Dependent Surveillance–Broadcast) data [17][44][60]. This has been applied in the form of lateral inefficiency factors [52], essentially a multiplier to the great circle distance, illustrated in Figure 2.4, or by taking the waypoints directly from the ADS-B data [60]. Trajectory data from ADS-B data is usually only commercially available from companies such as FlightRadar24,[2]; however, it is becoming increasingly available as open-source data [56]. The open-source data can be retrieved from OpenSKY Network,[3], although it still lacks global coverage when compared to FlightRadar24 [44].

In Rik Kroon's inventory used as the base for this study, the information model uses schedule data provided by FlightRadar24, as opposed to the ADS-B data used in both the works of Teoh et al.[60] and Quadros et al. [44]. From this data, commercial and business flights are analysed, as military aviation data is hard to come by, and general aviation mostly includes small planes using piston engines, for which emission data is not measured by the International Civil Aviation Organisation (ICAO) [25]. For each route, the great circle trajectory is taken, corrected by a lateral inefficiency factor. To maintain

[1] https://www.oag.com

[2] https://www.flightradar24.com/data/flights

[3] https://opensky-network.org

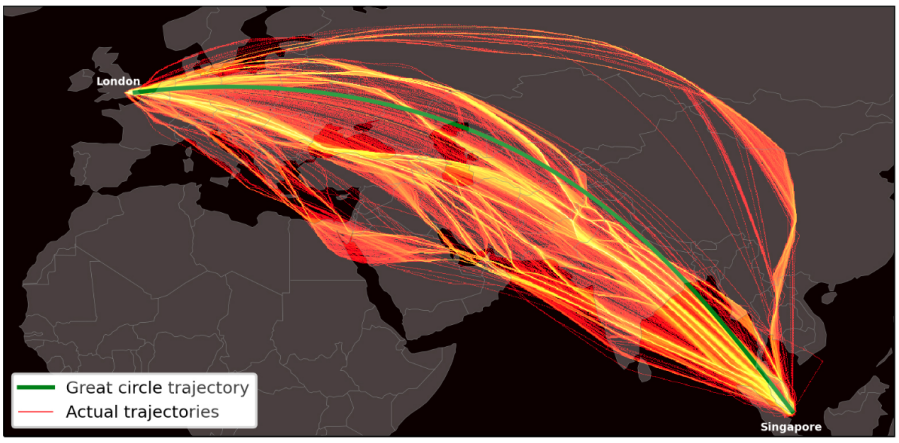

Figure 2.4: An example of the great circle trajectory compared to the actual flight trajectories for the route LHR - SIN. Figure taken from Teoh et al. [60].

computational efficiency, rather than analyse each flight individually, it was decided by the author to use a representative week. This representative week was chosen to represent an average week of air travel in a year, thus it was not taken in the high-season or low-season. In fact, the mean flights per week was found, and the week with the closest number of flights to the annual global mean was selected, as shown in Table 2.1. This week corresponds to Week 21 of the 2019 calendar year (May 20 - May 26).

Table 2.1: Number of commercial flights in the representative week compared to the yearly mean and median for 2019 in current work, by Rik Kroon [30].

Parameter	# Flights
Mean	806,631
Median	800,627
Representative week	808,637

On the other hand, Teoh et al. [60] analyse each flight of the year 2019 for which they have sufficient data. For each flight, Teoh et al. retrieve the actual trajectory using ADS-B data, providing precise information on both the flight path and altitude profile. Waypoints are sampled at intervals of approximately 40–60 seconds, and great circle interpolation is applied between them, resulting in a high-resolution reconstruction of each flight's movement through space. 77.6% of jet flights have full trajectory coverage, whereas the rest are reconstructed from the available waypoints and information. This enables not only accurate estimation of fuel burn and emissions but also accurately represents their spatial distribution [60].

Quadros et al. also incorporate ADS-B data; however, the actual trajectories are not used directly in their model. Instead, they use the great circle trajectory between the origin and destination airports and apply a lateral inefficiency factor. This factor is based on a regression analysis conducted by Seymour et al., who estimate a lateral inefficiency value of $d_{fp} = 1.0387 \cdot d_{gc} + 40.5$ [52]. In terms of flight altitude, Quadros et al. set a fixed cruise altitude per aircraft type, selected as the most common altitude observed per aircraft type in the first 70 days of 2020 [44] from ADS-B data. This holds for flights longer than 200 nautical miles, below which the average flight altitude per 50NM bin is taken. While this approach accounts for the increased distance flown compared to the shortest possible path, and the difference in flight altitude of various aircraft, it does not capture the full variation in altitude or routing due to airspace constraints, weather, or traffic, and therefore offers a coarser spatial representation of emissions [44].

2.4. Performance Models

Performance models are required in emission inventories as they are used to determine the fuel consumption of the aircraft in the flights analysed within the inventory. The most common method used in emission inventories is to measure the point performance of the aircraft at various waypoints along the trajectory. Most emission inventories use EuroControl's Base of Aircraft DAta (BADA) [37] for

their performance model. Among the recent global inventories (Quadros et al. [44], Teoh et al. [60], Klener et al. [60] and Rik Kroon [30]), all use BADA for climb, cruise and descent phases. BADA is based on the Total Energy Model (*TEM*), which functions by balancing potential and kinetic energy changes, providing a simplified representation of aircraft dynamics [36]. This is shown by Equation 2.2, where T is the thrust force, D is the aerodynamic drag, V_{TAS} is the true airspeed, m is the aircraft mass, and h is the altitude. The left-hand side represents the net energy available from the engine thrust, while the right-hand side represents the sum of potential energy change (due to altitude) and kinetic energy change (due to velocity). For each aircraft, a set of aerodynamic coefficients is provided to estimate lift and drag at each flight phase, and speed is determined based on altitude and flight phase, following a speed schedule (based on calibrated airspeed or Mach number). Thrust is determined differently based on flight phase. In cruise, it is equal to drag, whereas in climb and descent, BADA specifies a thrust setting determined empirically. The fuel consumption is then determined based on the thrust specific fuel consumption (TSFC) and calculated thrust [36].

$$(T - D)V_{\text{TAS}} = mg\frac{dh}{dt} + mV_{\text{TAS}}\frac{dV_{\text{TAS}}}{dt} \tag{2.2}$$

In cruise, the change in potential energy is 0, as horizontal flight is assumed. However, in climb and descent, the aircraft will climb or descend at a certain rate of climb or descent (ROCD). This ROCD is derived from the energy balance equation. The full methodology of the TEM is described further in Section 4.3.

In the case of Landing and Take-Off (LTO) emissions, the ICAO has an engine emission databank (EDB) which provides fuel flow and time spent at four thrust settings, corresponding to idle, approach, climb, and take-off, illustrated in Figure 2.5 [24]. These can be used in combination with BADA to get a full estimate of the total fuel used during the flight [30][44].

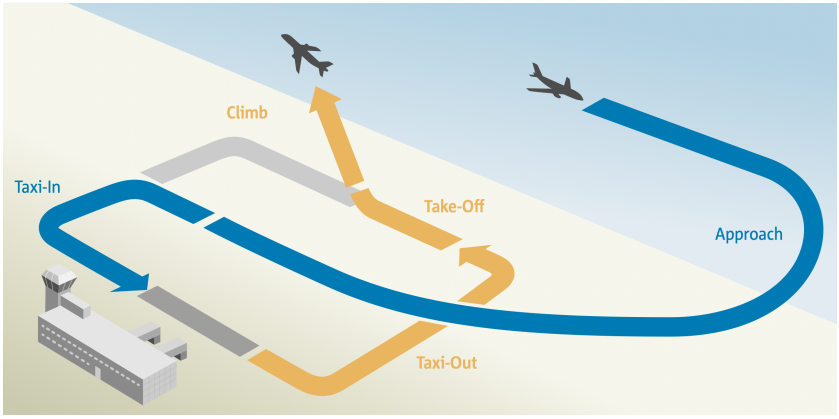

Figure 2.5: Illustration of the LTO-Cycle, with orange being departure LTO, and blue arrival LTO. ("Climb" refers to "Climb-Out" in the illustration). Figure taken from ICAO [1].

In Table 2.2, it should be noted that the total idle time is split into *idle out* (representing the taxi-out phase) and *idle in* (representing the taxi-in phase), 1140 s and 420 s, respectively.

Table 2.2: Thrust setting and time spent in each of the four LTO phases provided in the ICAO databank.

Flight phase	Thrust setting [%]	Time [s]
Idle	7	1560
Approach	30	240
Climbout	85	132
Take-off	100	42

There exist other performance models, such as PianoX, a commercial tool for flight analysis [17], and OpenAP, an open aircraft performance model [58], but their use is limited compared to BADA in global emission inventories. There is research being performed at the TUDelft on the use of OpenAP with OpenSky Network to develop emission inventories with open source data [57]. Finally, a last method

for estimating fuel burn is the Poll-Schumann method [41]. This method uses Reynolds number and atmospheric conditions to determine a flight altitude and Mach number pair that provides the minimum fuel burn [41]. However, BADA remains the go-to performance model for use in emission inventories, as it is accurate and efficient, with errors in the modelled fuel consumption reported to be lower than 5% compared to in-flight measurements and data provided to EUROCONTROL by aircraft manufacturers [37].

The base inventory model in this study also uses BADA, more specifically BADA3, to determine non-LTO point performance, and the ICAO databank is used to determine LTO point performance. The procedure followed in the current model is as follows:

1. Start with the estimation of the Take-Off Mass (TOM) of the given flight.
2. Determine the departure LTO fuel consumption from the ICAO EDB.
3. Determine the fuel consumption in climb, cruise, and descent using BADA.
4. Determine the arrival LTO fuel consumption from the ICAO EDB.

The TOM is estimated using the Operational Empty Mass (OEM), the fuel mass (M_f), and the payload mass ($M_{payload}$), the sum of which equals TOM. The OEM is simply taken as a fraction of the Maximum Take-Off Mass (MTOM). A load factor determines the payload mass with respect to the maximum payload mass in BADA. Finally, the fuel mass is determined by estimating the total fuel burn required to cruise from the departure airport to the arrival airport, at an assumed cruise altitude. The flight distance is taken as the great circle distance multiplied by a factor, as flights rarely fly the great circle route [12].

The LTO fuel consumption is determined as mentioned earlier in this section, with the ICAO engine emission database. For non-LTO climb, cruise and descent, the fuel consumption is determined at each segment of the constructed trajectory, using the geodesic path between departure and arrival. At each segment, the mass and altitude (in climb and descent) is updated based on fuel burn and ROCD, and using these two parameters, speed, ROCD (in climb and descent) and fuel consumption are determined. Given that the analysis assumes ISA conditions, performance tables provided for each aircraft within BADA are used. Cruise altitude is determined by assigning a threshold on ROC, below which the aircraft transitions from climb to cruise. In the case that the specific altitude or mass is not listed in the table, linear interpolation is performed between the nearest values.

The performance model used by Quadros et al. [44] works similarly to the baseline for this study. Both use BADA and ICAO as mentioned previously, and both assume geodesic flight paths between departure and arrival airports (the distance itself multiplied by a lateral inefficiency factor stemming from an analysis of ADS-B trajectories [52]). Where the models differ is in the cruise altitude determination and the use of MERRA-2 wind data, which affects the performance of the aircraft, and thus its fuel consumption. The cruise altitude is fixed for each aircraft type for flights above 200NM. It is taken as the most common cruise altitude observed through ADS-B data in the first 70 days of the year 2020 [44].

There also exists a more recent version of BADA, namely BADA4. This version is used in Teoh et al.'s inventory [60], in combination with BADA3, as BADA4 has improved accuracy, whereas BADA3 has higher coverage [40]. The working principle of BADA4 remains the same; Equation 2.2 is still used. The difference comes from the updated empirical relations and coefficients for aerodynamic performance, thrust and fuel consumption. Furthermore, when using ADS-B data, the speed at each waypoint is known, thus it becomes an input to the performance model in BADA. Similarly to the performance model in Quadros et al. [44], wind data is also implemented, albeit from a different source (ERA5 HRES [7]). The cruise altitude is taken from the telemetry data, and is unique for each route. Finally, the aircraft mass is determined through iteration, with the initialisation run using MTOW, following a method developed by Wasiuk et al. [64]. Afterwards, a mission fuel is determined, and the TOM is calculated by summing the OEM, payload mass, and fuel mass. This process is reiterated until the mission fuel reaches convergence [64].

2.5. Emission Models

Emission models are the final building block of most emission inventories. It involves determining the emission indices of various species of emissions. Emission indices simply relate the amount of a specific gas emitted to a kilogram of fuel. Aside from the products of complete combustion calculated from stoichiometry (CO_2 and H_2O, most importantly) from the complete combustion equation:

$$4C_{12}H_{23} + 71O_2 \rightarrow 48CO_2 + 46H_2O,$$

the most common form of emission modelling for gaseous non-CO_2 emissions is the fuel flow method [15] [46].

2.5.1. Fuel Flow Methods

These methods are commonly used as they are computationally efficient and do not require proprietary engine information, and thus can be generalised easily for global emission inventories. The main functioning of these fuel flow methods is to take the fuel flow determined in the performance model of the inventory and use a database with engine details and emission indices to interpolate the given emission index at the given fuel flow. The Boeing Fuel Flow Method 2 (BFFM2) [15] is widely accepted as the go-to method for determining these non-CO_2 emissions throughout the years. It has been used in NASA's inventory for 1992 [4], Owen et al.'s analysis of IPCC scenarios [38] and the recent emission inventories by Quadros et al. [44], Teoh et al. [60], Klener et al. [29] and the inventory developed by Rik Kroon used in this study [30]. The general principle of the fuel flow method is illustrated in Figure 2.6. It shows how the fuel flow from the performance discipline is converted from in-flight to ground reference conditions. This is because the ICAO databank includes the Emission Index (EI) for these species of emissions at ground conditions for four thrust settings.

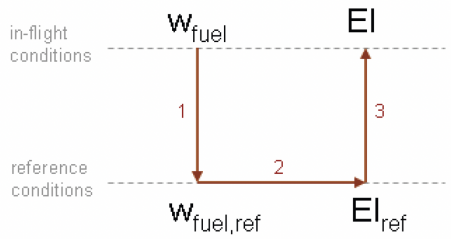

Figure 2.6: Working principle of the Boeing fuel flow method. Figure taken from Schaefer et al. [46].

A small airframe correction factor is applied to the fuel flow due to bleed air [4]. The relevant emission index is interpolated for the ground reference conditions and then corrected back to in-flight conditions. The fuel is corrected to ground conditions using the correction shown in Equation 2.3, where W_f and W_{ff} are the fuel flows at in-flight altitude and sea level, respectively, M is the Mach number and T_{amb} and p_{amb} are the ambient temperature and pressure, respectively [46].

$$W_{ff} = \frac{W_f}{\delta_{amb}} \cdot \theta_{amb}^{3.8} \cdot e^{0.2 \cdot M^2} \quad \text{where } \theta_{amb} = \frac{T_{amb}}{288.15\ \text{K}} \text{ and } \delta_{amb} = \frac{p_{amb}}{101325\ \text{Pa}} \tag{2.3}$$

For determining EI(NO_x) a linear interpolation is performed on the logarithmic values of the EI and fuel flow, whereas bilinear interpolation is used to determine EI(CO) and EI(HC), as illustrated in Figure 2.7 [15] [46].

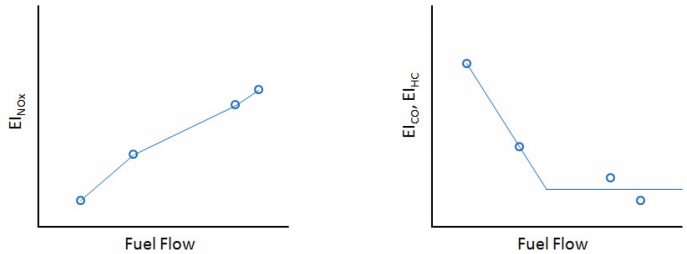

Figure 2.7: Linear interpolation of log(EI(NO_x)) vs fuel flow, and log(EI(CO)) and log(EI(HC)) vs fuel flow in BFFM2 method. Figure taken from Schaefer et al. [46].

The emission indices are corrected back to in-flight conditions using Equations 2.4 and 2.5 for CO and HC, respectively, and Equation 2.6 for NO_x. The term H in the equation represents a humidity correction term. This term is determined empirically and is dependent on the relative humidity. This value is set to 0.6 in the BFFM2, as it corresponds to a humidity ratio of 0.00634 [kg H_2O/kg dry air] assumed by the ICAO [15], but can be replaced with the actual relative humidity if weather data is available.

$$\mathrm{EI(CO)} = \mathrm{EI_{ref}(CO)} \cdot \frac{\theta_{amb}^{3.3}}{\delta_{amb}^{1.02}} \tag{2.4}$$

$$\mathrm{EI(HC)} = \mathrm{EI_{ref}(HC)} \cdot \frac{\theta_{amb}^{3.3}}{\delta_{amb}^{1.02}} \tag{2.5}$$

$$\mathrm{EI(NO_x)} = \mathrm{EI_{ref}(NO_x)} \cdot \sqrt{\frac{\theta_{amb}^{3.3}}{\delta_{amb}^{1.02}}} \cdot e^{H} \tag{2.6}$$

AERO2k in 2004 uses the DLR fuel flow method [17]. The DLR method and BFFM2 methods differ slightly in their altitude correction and, most importantly, in their NOx interpolation method. Unlike the BFFM2, which performs a linear interpolation in logarithmic scale between each point, as shown in Figure 2.7, the DLR method uses a parabolic trendline between the four ICAO points [46].

Similar to these methods, there exists a so-called P3-T3 method. This method is generally more accurate than the commonly used fuel flow methods, with the downside being that it requires proprietary engine information [15]. However, for RQL engine types, the most common in the market, the fuel flow methods show similar results to the P3-T3 method, within 10% to 15% when it comes to NO_x [15] [46]. Given their advantage when it comes to accessibility, they are preferred over the P3-T3 method.

Rik Kroon uses the BFFM2 in their emission model [30]. The same holds for Quadros et al. [44] and Teoh et al. [60], although the latter use the relative humidity from ERA5 weather data.

2.5.2. Methods for nvPM Emissions

Another species of emissions considered in emission inventories is non-volatile Particulate Matter (nvPM) or Black Carbon (BC), often used interchangeably [44]. Indeed, before 2020, the ICAO Databank did not include measurements for nvPM emissions, and rather, fine particulate matter emissions were discussed in terms of black carbon. However, this overlooks the fact that even a small mass of black carbon can contain a large number of particles. Ultimately, nvPM consists almost entirely of black carbon [16]. Therefore, not all engines in the ICAO engine emissions databank include measurement data for nvPM emissions, thus multiple methods exist for estimating the emission index, as regulations were originally set on the Smoke Number (SN) of the aircraft, leading to the inclusion of Smoke Number measurements in the ICAO EDB over particulate matter measurements [2].

FOA3.0 & Peck et al.

The inventory of Rik Kroon [30] uses a method developed by Peck et al. [39]. This method provides two ways to determine the nvPM emission index, one for the engines which have EI nvPM measurements in the ICAO EDB, and those which have a smoke number instead. In both cases, the method starts as follows:

1. Determine, from the cruise altitude and Mach number, the total atmospheric pressure and temperature using ISA relations.
2. Determine the cruise thrust setting. A linear interpolation is performed between the fuel flow and thrust setting for the four ICAO points. The fuel flow is first converted from in-flight conditions to sea level conditions, using Equation 2.3.
3. The combustor inlet pressure P_3 at cruise is determined using the cruise thrust setting determined previously $\frac{F}{F_{00}}$ and the overall pressure ratio π_{00} as in Equation 2.7.

$$\frac{P_{3,\mathrm{cruise}}}{P_{t,\,\mathrm{cruise}}} = 1 + \left[\frac{F}{F_{00}}\right]_{\mathrm{cruise}} (\pi_{00} - 1) \tag{2.7}$$

4. The combustor inlet temperature T_3 is determined next using the pressure P_3 as described by Equation 2.8, where the compressor efficiency is assumed to be $\eta_{\mathrm{comp}} = 0.85$

$$\frac{T_{3,\mathrm{cruise}}}{T_{t,\,\mathrm{cruise}}} = 1 + \frac{1}{\eta_{\mathrm{comp}}} \left\{ \left(\frac{P_{3,\mathrm{cruise}}}{P_{t,\,\mathrm{cruise}}} \right)^{\frac{\gamma-1}{\gamma}} - 1 \right\} \tag{2.8}$$

5. Fixing the combustor inlet temperature at ground reference conditions as in flight conditions ($T_{(3,ref)} = T_3$), the ground reference $P_{3,\text{ref}}$ is calculated in Equation 2.9.

$$\frac{P_{3,\text{ ref}}}{P_{\text{ground}}} = \left\{1 + \eta_{\text{comp}} \left(\frac{T_{3,\text{ ref}}}{T_{\text{ground}}} - 1\right)\right\}^{\frac{\gamma}{\gamma-1}} \tag{2.9}$$

6. Finally, the ground reference thrust setting is determined using the ratio of reference combustor inlet pressure over ground level ambient pressure P_{ground} and overall pressure ratio as shown in Equation 2.10.

$$[F/F_{00}]_{\text{ref}} = \frac{\frac{P_{3,\text{ ref}}}{P_{\text{ground}}} - 1}{\pi_{00} - 1} \tag{2.10}$$

If nvPM EI measurements are present, a cubic interpolation is performed between the nvPM EI and the thrust setting, using the reference thrust setting as calculated in Equation 2.10. Otherwise, SN is used. In this case, the emission index is calculated based on a relation between the SN and the EI(BC). The reference EI(BC) is taken as 14.8 times the reference SN. Then the cubic interpolation is performed. And once the reference emission index is determined, the following steps are taken to convert this to in-flight conditions:

1. The EI(BC) is converted to BC concentration $C_{\text{BC,ref}}$ as shown in Equation 2.11, where $\dot{Q}$ is the volumetric flow rate per kg of fuel burnt at the given thrust setting, as per Equation 2.12. In this equation, β is equal to the Bypass Ratio (BPR) of the engine.

$$C_{\text{BC,ref}} = \frac{\text{EI}_{\text{ref}}(\text{BC})}{\dot{Q}} \tag{2.11}$$

$$\dot{Q} = 86.37e^{-0.9136(F/F_{00})}(1 + \beta) + 0.877 \tag{2.12}$$

2. Then the concentration is corrected to in-flight conditions. This is done using the Döpelheuer and Lecht approximation involving the equivalence ratio, combustor inlet pressure and adiabatic flame temperature at in-flight and reference conditions [14]. The Döpelheuer and Lecht correlation is given in Equation 2.13, where the adiabatic flame temperature is calculated in Equation 2.14. The equivalence ratio Φ is taken as 1 for both ground reference and in-flight conditions.

$$C_{BC} = C_{BC,ref}\left(\frac{\phi}{\phi_{ref}}\right)^{2.5}\left(\frac{P_{3,\text{cruise}}}{P_{3,\text{ref}}}\right)^{1.35}\left(\frac{e^{-\frac{20,000}{T_n}}}{e^{-\frac{20,000}{T_{n,ref}}}}\right) \tag{2.13}$$

$$T_{fl} = 2281\left(P_3^{0.009375} + 0.000178P_3^{0.055}(T_3 - 298)\right) \tag{2.14}$$

3. Finally, the in-flight EI(BC) is determined by multiplying the in-flight concentration and volumetric flow rate per kg of fuel burnt, as shown in Equation 2.15.

$$\text{EI(BC)} = \text{C}_{\text{BC}}\dot{Q} \tag{2.15}$$

Quadros et al. [44] follows the same method for nvPM mass emissions, with the exception of the SN relation. Instead they use the updated FOA4.0 method.

FOA4.0

The First Order Approximation (FOA4.0) methodology is used to estimate the nvPM emissions index, in the case where no nvPM EI measurement is present in the ICAO EDB. The approach consists of the following steps:

1. Extracting the soot number (SN) from the ICAO EDB to determine the particle concentration C_k.

$$C_k = \frac{684.4 \cdot e^{0.0766 \cdot SN_k}}{1 + e^{-1.098 \cdot (SN_k - 3.064)}} \tag{2.16}$$

2. Using the air-to-fuel ratio (AFR) and bypass ratio (BPR) to obtain the specific exhaust volume Q_k.

$$Q_k = 0.777 \cdot AFR_k \cdot (1 + \beta) + 0.767 \quad (\text{in } m^2/kg) \tag{2.17}$$

3. Applying the concentration and BPR to derive the system loss correction factor $k_{\text{slm},k}$.

$$k_{\text{slm},k} = \ln\left(\frac{3.219 \cdot C_k \cdot (1+\beta) + 312.5}{C_k \cdot (1+\beta) + 42.6}\right) \tag{2.18}$$

The resulting nvPM emissions index is calculated using Equation 2.19.

$$\text{EI}_{\text{nvPM,mass}} = k_{\text{slm},k} \cdot Q_k \cdot C_k \tag{2.19}$$

Following from the nvPM mass emission index, the nvPM number emission index can be found using Equation 2.20.

$$\text{EI}_{\text{nvPM,number}} = \frac{\text{EI}_{\text{nvPM,mass}} \cdot N_r}{\frac{\pi}{6} \cdot \rho \cdot \text{GMD}^3 \cdot e^{4.5(\ln\sigma)^2}} \tag{2.20}$$

where:

- ρ = 1000 [kg/m3], nvPM particle effective density,
- σ = 0.8 , assumed geometric standard deviation of the nvPM particle size distribution,
- $N_r = 10^{24}$, unit scale factor (kg nm3/g m3).

Unlike the method of Peck et al. [39], the FOA4.0 provides a value for the nvPM number emission index. Indeed Rik Kroon lacks this specific emission estimate in their inventory [30]. In the case where the nvPM number measurement is provide by the ICAO databank, Quadros et al. simply employ a linear interpolation [18].

T4T2 method

Teoh et al. [60] use an internally developed method, called the T4/T2 method [61], to estimate these emissions in the case where the ICAO EDB includes the nvPM measurements (63.3% of flights). This new method is validated through measurements from the ECLIF II/ND-MAX measurement campaign of both ground and cruise nvPM emissions, albeit for one aircraft and engine [47]. T4/T2 is used as a non-dimensional measure for engine thrust setting. Based on the four ICAO measurement points per engine, a linear interpolation is then performed relative to the ratio T4/T2. T4 and T2 must be determined however, and Figure 2.8 shows the methodology for determining each. In red the thrust setting is highlighted. This is determined using Equation 2.21, where MSL represents mean sea level, and the fuel flow at sea level is converted from cruise using the BFFM2 relation [15].

$$\frac{F}{F_{00,\max}} = \frac{\dot{m}_f^{MSL}}{\dot{m}_{f,\max}} \quad \text{where} \quad \dot{m}_f^{MSL} = \dot{m}_f^{\text{Cruise}} \left(\frac{T_{\text{amb}}}{T_{MSL}}\right)^{3.8} \left(\frac{p_{MSL}}{p_{\text{amb}}}\right) e^{0.2M^2} \tag{2.21}$$

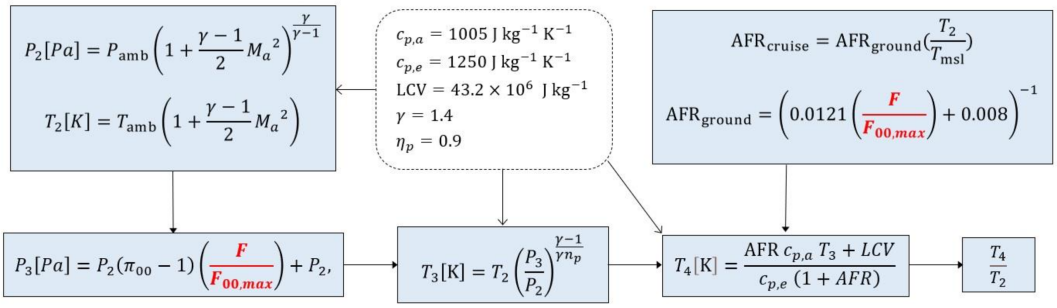

Figure 2.8: Method used by Teoh et al. et determine the ratio T4/T2 in the nvPM EI estimation. Figure taken from Teoh et al. [59].

In the case the engine has a lean technology combustor such as DAC or TAPS, the method incorporates a step change after 30% thrust setting, where the nvPM mass and number EIs are simply taken as a constant equal to the average of 85% and 100% [59]. This is following a study analysing BC measurements on a DAC combustor, which shows a drop in the emission index of nvPM mass and number after the pilot stage (Figure 2.9), conducted by Boies et al. [5] on a CFM-5B4-2P engine.

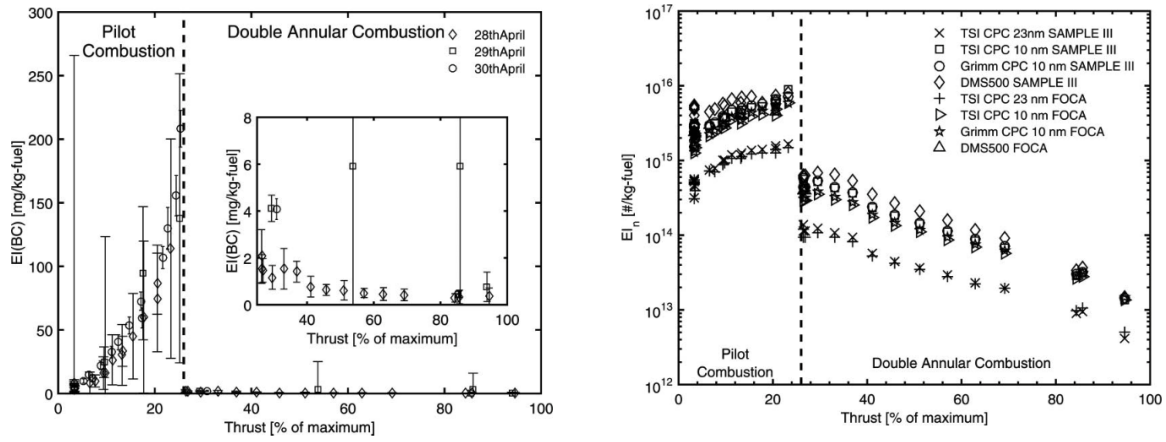

Figure 2.9: Measurement data of EI(BC) vs thrust setting (left) and particle number vs thrust setting (right). Figure taken from Boies et al. [5].

The nvPM measurements may not be available in the ICAO databank for a given engine, in which case Teoh et al. [60] make use of the FOX and ImFOX methods for estimating nvPM mass emissions, and the Fractal Aggregates Method for converting nvPM mass to nvPM number. The fractal aggregates method works similarly to Equation 2.20, in that it uses the geometric mean diameter of the particles, in this case a function of T4/T2 [59].

FOX & ImFOX

The FOX method is based on the formation and oxidation rates of soot, removing the dependence on the SN from ICAO. The black carbon concentration is then approximated by Equation 2.22, which models formation rate as fuel mass flow rate $\dot{m}_f$ multiplied by a constant A_{form} equal to 356 and an exponential term containing the flame temperature T_{fl}, and the oxidation rate, based on the concentration of air, as the product of the fuel mass flow rate, the air-to-fuel ratio, a constant A_{ox} equal to 608 and another exponential based on the flame temperature [55].

$$C_{\text{BC}} = \dot{m}_f \left(A_{\text{form}} \cdot e^{-6390/T_{fl}} - A_{\text{ox}} \cdot \text{AFR} \cdot e^{-19778/T_{fl}} \right). \tag{2.22}$$

The flame temperature is predicted using a linear relation with combustor inlet temperature T_3, as shown in Equation 2.23.

$$T_{fl} = 0.9T_3 + 2120. \tag{2.23}$$

The ImFOX method is simply an improved FOX method developed by Abrahamson et al. [2]. Using proprietary information from a common RQL combustor engine on which they perform measurements, updated relations are provided to the FOX method. Based on measurements, two new relations for AFR based on thrust setting,

$$\text{AFR}_{\text{gr}} = 71 - 35.8 \left(\frac{\dot{m}_f}{\dot{m}_{f,\text{max}}} \right), \tag{2.24}$$

$$\text{AFR}_{\text{cr}} = 55.4 - 30.8 \left(\frac{\dot{m}_f}{\dot{m}_{f,\text{max}}} \right), \tag{2.25}$$

the former for ground and and the latter for cruise. Furthermore, the formation rate constant is substituted it with a third order relation to thrust setting,

$$A_{\text{form}} = 1013 - 4802 \left(\frac{\dot{m}_f}{\dot{m}_{f,\text{max}}} \right) + 7730 \left(\frac{\dot{m}_f}{\dot{m}_{f,\text{max}}} \right)^2 - 3776 \left(\frac{\dot{m}_f}{\dot{m}_{f,\text{max}}} \right)^3, \tag{2.26}$$

which leads to the updated concentration relation in Equation 2.27, where the flame temperature is substitute by the turbine inlet temperature T_4, and a fuel hydrogen mass content factor H is added.

$$C_{\text{BC}} = \dot{m}_f \cdot e^{(13.6-H)} \left(A_{\text{form}} \cdot e^{-6390/T_4} \right) - A_{\text{ox}} \cdot \text{AFR} \cdot e^{-19778/T_4} \tag{2.27}$$

In both cases to convert the concentration to emission index, the specific exhaust volume is used, as provided in Equation 2.17.

nvPM Mission Emissions Estimation Methodology (MEEM)

There exist other methods for determining nvPM emissions. One such method was developed by Arhens et al. [3] and coined the nvPM Mission Emissions Estimation Methodology (MEEM). The method itself is based on the FOA4 method, as well as the method of Peck et al. [39]. As mentioned previously, Peck et al. do not consider the nvPM number. An earlier study by Durdina et al. [16] improved the method of Peck et al., updating the interpolation method and including the nvPM emissions. The study makes use of measurements and an engine performance model for two Boeing 737NG engines, the specific variant unnamed for proprietary reasons. This makes the method specific to these engines, and could lead to greater error among other engines. The MEEM study, therefore, looks to provide a general approach for a fleet-wide nvPM emission estimation method [3].

The approach consists of the same initial steps as those of the Peck et al. [39] method mentioned previously, thus from Equation 2.7 to Equation 2.10. There are two main differences, however: In Equation 2.7 the thrust setting is approximated by a pressure coefficient Π_{Alt}, which is essentially the ratio of the pressure ratio at cruise to the operating pressure ratio π_{00}; and in Equation 2.8 the compressor efficiency is different. These parameters are flight phase dependent and listed in Table 2.3. In climb Π_{alt} varies with altitude as displayed in Equation 2.28, above 3000ft, as that's when climbout ends, and above this altitude is no longer considered LTO.

Table 2.3: Compressor efficiency and pressure coefficient parameters for MEEM [3].

Flight phase	Compressor efficiency [-]	Pressure coefficient [-]
Climb	0.88	0.85 - 1.15
Cruise	0.88	0.95
Descent	0.7	0.12

$$\Pi_{\text{Alt}} = 0.85 + (1.15 - 0.85)\frac{h - 3000}{h_{\text{cruise}} - 3000} \tag{2.28}$$

In the above steps, the values of P_3 and T_3 are validated against proprietary manufacturer engine deck data. The authors have access to thirteen engines present in the ICAO EDB, covering small business jets to large aircraft [3]. This is performed in order to find values of Π_{Alt} and η_{comp} which minimise errors in P_3 and T_3.

The next step involves interpolating the cruise nvPM EI from the ICAO ground measurements, if the nvPM mass and number measurements are provided in the ICAO EDB. Otherwise, the FOA4 method is first applied to the smoke number. There are two possible interpolation methods, a 4 point and 5 point method, both of which are linear. The 5 point method is used on engines where the maximum nvPM measured value is listed in the ICAO databank. This peak value does not contain an associated thrust setting, so the method applies it at a 57.5% thrust setting. This is illustrated in Figure 2.10.

Finally, the cruise EI is determined using the Döpelheuer and Lecht correlation (Equation 2.13) [14]. In this case, the BC concentration can be replaced with EI nvPM mass. Using the proprietary engine information at their disposal, the authors concluded that the adiabatic flame temperature term was negligible, and that the ratio of equivalence ratios in Equation 2.13 should be set to 1.1 rather than 1 (as done in Peck et al.'s method [39]), as combustors tend to burn richer at altitude relative to ground [3]. This leads to the correction equation given in Equation 2.29.

$$EI_{\text{nvPM,mass}} = EI_{\text{nvPM,ref}} \left(\frac{P_{3,\text{cruise}}}{P_{3,\text{ref}}} \right)^{1.35} 1.1^{2.5} \tag{2.29}$$

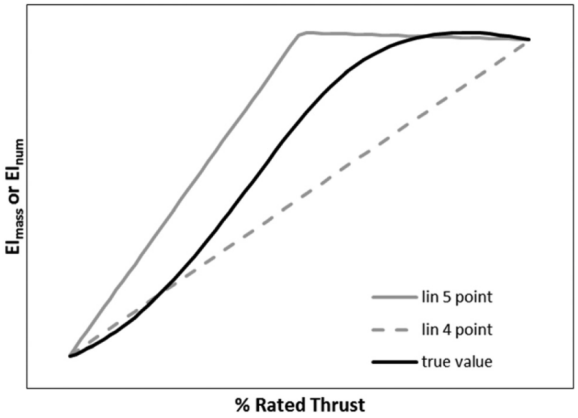

Figure 2.10: Linear interpolation between approach and climbout ICAO points, with and without peak point. Figure taken from Ahrens et al. [3].

The corresponding nvPM number emission index is calculated as follows, as it is assumed particle diameter is only a function of T_3 [16].

$$\mathrm{EI}_{\mathrm{nvPM,number}} = \mathrm{EI}_{\mathrm{nvPM,mass}} \frac{\mathrm{EI}_{\mathrm{nvPM,number,ref}}}{\mathrm{EI}_{\mathrm{nvPM,mass,ref}}} \tag{2.30}$$

2.6. Results of 2019 Inventories

The implementations used in this comparison are inventories covering the year 2019. These include inventories developed by Quadros et al [44] and Teoh et al [60]. Differences lie in the three models, discussed in the previous section for the current implementation. Table 2.4 gives an overview of the results of each inventory, with a focus on the NO_x and nvPM emissions.

Table 2.4: Comparison of the results of global emission inventories for the year 2019.

Metric	Rik Kroon [30]	Teoh et al. [60]	Quadros et al. [44]
Fuel burn [Tg]	272	283	297
NO_x [Tg]	5.3	4.49	4.62
nvPM mass [Gg]	6.8	21.4	9.68
nvPM number [#]	–	2.83E+26	3.57E+26
EI NO_x [g kg-1]	17.716	15.866	15.556
nvPM mass [g kg-1]	0.021	0.076	0.033
nvPM number [# kg-1]	–	1.00E+15	1.20E+15

3

Research Goal

This chapter discusses the research gaps identified in the current work and other implementations in the literature. Firstly, an overview of an ideal emission inventory is presented in section 3.1, followed by the gaps present in the current emission inventories. Finally, the research questions of this study will be posed in section 3.7.

3.1. Ideal Emission Inventory

Before assessing the research gaps, it is important to establish a clear understanding of the desired research outcome. This process involves developing a template for an ideal emission inventory, which serves as a benchmark for evaluating current inventories. As such, these inventories can be compared to this standard to identify the research gaps. Table 3.1 summarises the main elements of an ideal emission inventory. Within the table the main global inventories for the year 2019 are assessed [30] [60] [44].

Table 3.1: Characteristics of an Ideal Emission Inventory

Criterion	*Rik Kroon*	*Teoh et al.*	*Quadros et al.*
Coverage & Resolution			
Provides global emission estimates	✓	✓	✓
Provides regional resolution	✓	✓	✓
Includes seasonal variation	-	✓	✓
Provides fleet-level emissions	✓	✓	✓
Includes flight-specific engine assignments	-	✓	-
Includes both LTO and CCD emissions	✓	-	✓
Modeling & Methods			
Uses precise flight trajectories	-	✓	-
Incorporates weather data	-	✓	✓
Uses precise aircraft take-off mass	-	-	-
Uses up-to-date performance models	-	✓	-
Uses up-to-date emission models	-	✓	-

As mentioned previously, the base model for this study is the inventory developed by Rik Kroon [30]. The other two inventories are included as they cover the same year and serve as benchmarks in areas where they outperform the base model. It should be noted that the base model has been updated

internally at the TUDelft prior to this research, thus the results used as baseline differ from those of Rik Kroon's original work.

While all the inventories work towards a common goal of accurately estimating emissions and developing tools that can be used for predicting future emissions, their methodologies, assumptions, and data sources can vary. Understanding these differences and highlighting the range of possible outcomes provides insight into the scope of the uncertainty present in estimating global emissions, and attempting to reproduce results using the same methodologies offers a way to validate and corroborate existing findings.

Accordingly, the primary goal is to build upon the existing capabilities present in the inventory of Rik Kroon [30], preserving the computational efficiency. A secondary goal is to investigate the sources of discrepancy between emission estimates across inventories. The following sections will focus in more detail on the specific gaps of the base model, and compare it to the other two models.

3.2. Engine Assignment

Firstly, the flight-specific engine assignment will be addressed. A precise engine assignment is important as different engines can vary in terms of combustion technologies and performance characteristics. This leads to differences in the emission output of these engines, and often, one aircraft type will have multiple variants using different engines. An example of this is provided for the A320 aircraft in Figure 3.1, with the engines taken from the share derived by Cirium for Teoh et al. [60].

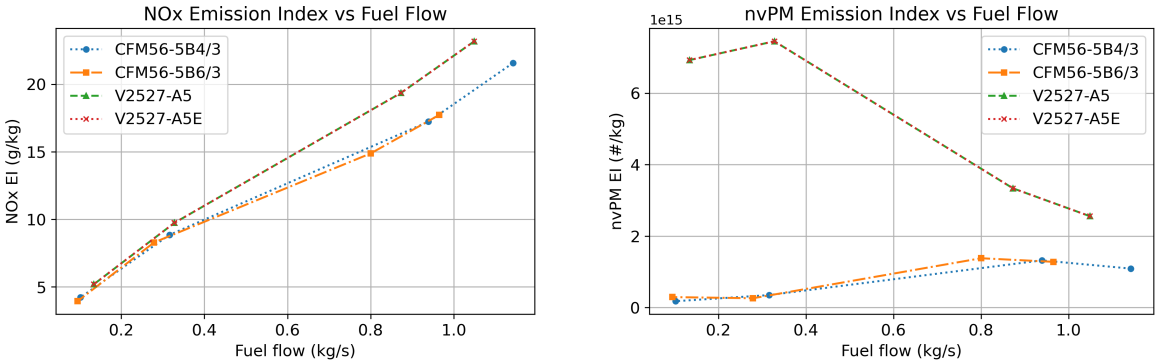

Figure 3.1: Comparison of NO_x (left) and nvPM (right) emission indices as a function of fuel flow across four main A320 engine types from Teoh et al.'s market share [60].

Teoh et al. approach this ideal most closely. By licensing the commercial Cirium fleet database[1], they link registrations found in schedule and ADS-B data to the corresponding engine type, achieving flight-specific assignments for 79% of all jet aircraft flights [60].

Quadros et al. adopt a different strategy. They compile aircraft and engine manufacturer data, as well as crowdsourced fleet data, to derive a global market-share for each engine family per aircraft type, and then distribute emissions proportionally [44]. This method is aircraft-specific rather than flight-specific, as it doesn't provide information on the engine type of a given flight, nor of the predominant engine(s) for a given route.

In the baseline inventory, each aircraft is paired with the single "reference" engine listed in BADA 3. While convenient, this one-to-one mapping ignores the fact that, like for the A320 displayed in Figure 3.1, many aircraft types operate with multiple engine variants, each with their own performance and emission characteristics. Ideally, the engine assignment would be resolved at the flight level, using the aircraft's registration (tail number) to query national registries and determine, as best as possible, the exact engine used by this specific aircraft.

Consequently, the present study inherits the BADA 3 assignment but recognises the need to move toward a more representative engine distribution on a flight level, as demonstrated by Teoh et al. [60]. Incorporating registry-based matching or, where coverage is incomplete, supplementing with market-share weighting, as done by Quadros et al. [44], is a first step in closing the engine-selection gap identified in Table 3.1.

[1] `https://www.cirium.com`

3.3. Flight Trajectories

The next aspect is the flight trajectories. Indeed, to effectively model the fuel burn and emissions of a flight, the path it takes from the departure airport to the arrival airport must be known, and the same for the altitude at which it flies. This is also important for the spatial distribution of the emissions, which are used for climate impact assessments.

Again, Teoh et al. [60] come closest to the ideal. This is due to their implementation of ADS-B data to build the trajectories for most of the flights analysed in their inventory, as opposed to Quadros et al. [44] and Rik Kroon [30], as discussed in section 2.2.

In the case of Rik Kroon's inventory, the values for lateral inefficiency are derived from limited data obtained from a single airline. This data set encompasses only about 23 flights, which represent less than 0.001% of all analysed flights [30]. This limited sample size could lead to inaccuracies in the en-route multipliers that are used in the performance model. A histogram of the flights in question and their distance compared to the great-circle distance is shown in Figure 3.2.

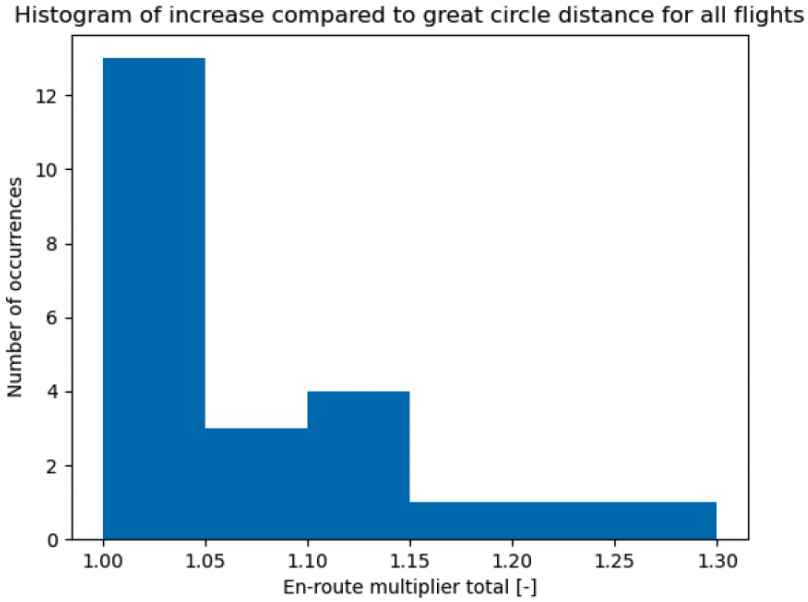

Figure 3.2: Histogram of the increased flight distance compared to the great circle distance for all flights, illustrating the distribution of en-route multipliers, by Rik Kroon [30].

In addition to the lateral inefficiency, the modelling of flight altitude is another area in need of refinement. As mentioned in section 2.2, the cruise altitude is currently dynamically allocated to each flight once it surpasses a rate of climb (ROC) threshold of 500 feet per minute. The ROC is determined through BADA. This simplification is a promising start as it takes into account the weight of a given aircraft. Indeed, the closer the take-off mass of an aircraft is to its take-off mass, the lower its rate of climb will be, due to increased drag. However, it may overlook the variations in climb rates between aircraft types, and the variations in cruise level beyond simply aircraft mass, such as flight distance, traffic, or weather. Keeping the dynamic assignment of cruise altitude through the use of ROC is desired, but fine-tuning the value itself and validating it with ADS-B or other real-world flight altitude data would improve the fidelity of both fuel burn and emissions estimates.

3.4. Take-Off Mass

As discussed in section 2.2, all inventories broadly follow the same formulation to determine take-off mass (TOM), defined as the sum of the operating empty mass (OEM), payload mass, and fuel mass, although the methods used to estimate each component differ across inventories.

Since precise take-off masses or payload factors for individual flights are not publicly available, no inventory can fully achieve this ideal. Nevertheless, accurately estimating each component remains essential for producing a reliable emission inventory. Thus, the gaps associated with the current inventory are discussed.

The first of these is the operating empty mass (OEM). Currently, the OEM is determined by simply

multiplying the maximum take-off mass by a factor of 0.5. This factor has a standard deviation of 0.25, which is large, and it was only determined based on 9 aircraft types.

Secondly, the method for determining initial fuel mass is likely inconsistent with the mass of fuel and altitude determined through trajectory analysis. As mentioned in section 2.2, the initial fuel mass for a given flight is calculated by assuming a cruise over the geodesic distance from departure to arrival, at maximum take-off weight and a cruise altitude offset by 7000 ft from the maximum altitude specified in BADA. This 7000 ft offset has been used to assign cruise altitudes in other emission inventories [54]. However, the performance model during trajectory analysis determines the cruise altitude using a rate of climb threshold, as mentioned previously, and uses a TOM other than MTOM. Thus, ultimately, the total fuel consumption will be different to the fuel consumption in the initial estimate. This introduces uncertainty into the performance model and is an aspect to be addressed in this research.

3.5. Performance Model

In terms of the performance model, as mentioned in section 2.2, all three inventories use EUROCONTROL's BADA model [37]. The methodology followed in BADA is already described in section 2.2. The most up-to-date version of BADA is BADA4, leveraging the increase in high-quality aircraft performance reference data and computational capabilities to form a more complex model, which improves accuracy. For a given aircraft, the number of coefficients used to model the performance in BADA4 exceeds 50, whereas only about 20 coefficients are used in BADA3 [40]. Additionally, BADA4 includes variant-specific aircraft performance models, thus the performance now becomes engine dependent, whereas previously it was solely based on the aircraft type. This is illustrated in Figure 3.3.

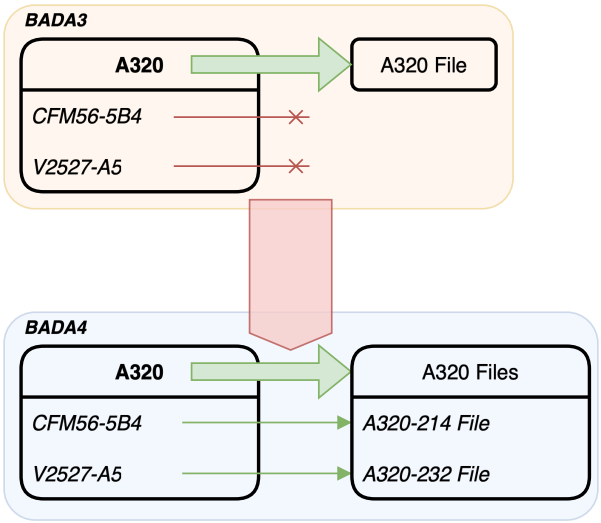

Figure 3.3: Transition to aircraft variant performance modeling from BADA3 to BADA4.

Teoh et al. use BADA4 when possible, and complete the performance of the aircraft not covered by BADA4 with BADA3.

3.6. Emission Model

The goal of the emission model is to accurately estimate the emissions of a given engine in flight. In order to do so, a model that is recent, that factors in changes and updates in engine technologies and makes use of engine/flight measurement data is ideal. The two main emissions focused on in this study are nvPM emissions and NO_x emissions.

3.6.1. nvPM Emissions

The methods used by each inventory in determining the nvPM emissions are described in section 2.2; the current method used by Rik Kroon in the baseline inventory does not cover nvPM number emissions. This is one of the main gaps of the inventory. Furthermore, the FOA3 SN correlation used in the inventory is outdated. This correlation, according to Durdina et al. [16], overestimates the black carbon emission index, especially at low thrust settings. According to the article the FOA4 method would provide an SN-BC correlation more aligned with their measurements. On the other hand, measured data by Abrahamson et al. [2] suggest an underestimation of BC emission indices at higher thrust

settings for the FOA3 method.

Quadros et al. [44] use the updated FOA4 correlation described in section 2.2, and include nvPM emissions for both mass and number. However, their study makes use of the method of Peck et al. [39], which has been updated by both Durdina et al. [16] and Ahrens et al. [3] as described in section 2.2.

Finally, Teoh et al. [60] come closest to the ideal of up-to-date emission inventory as they employ the T4T2 method. [61], which incorporates more recent ground and cruise measurements for the validation of the method.

None of the inventories mentioned in Table 3.1 apply the MEEM approach developed by Ahrens et al. [3], which is validated over a wide range of engines, and coincides well with A359 data from the ECLIF 3 measurement campaign, shown in Figure 3.4 [10].

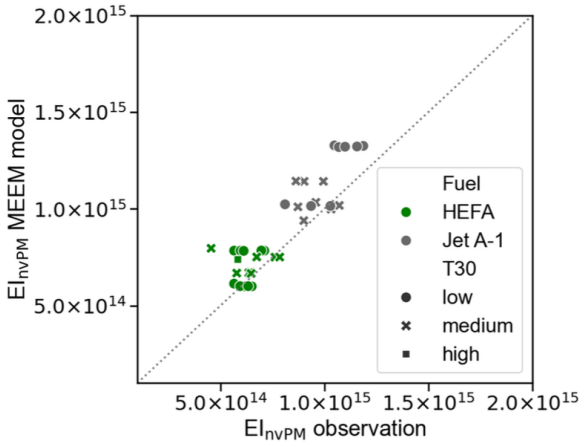

Figure 3.4: Comparison of nvPM measurements to estimated nvPM model values from MEEM, based on fuel type and T_3. Figure taken from Dischl et al. [10].

3.6.2. NO_x Emissions

As mentioned in section 2.2, all three methods apply the BFFM2 for estimating NO_x emissions. The BFFM2 method remains a good approach as it corresponds well with recent ECLIF2 and ECLIF3 measurement campaigns, as illustrated by Figure 3.5 [20].

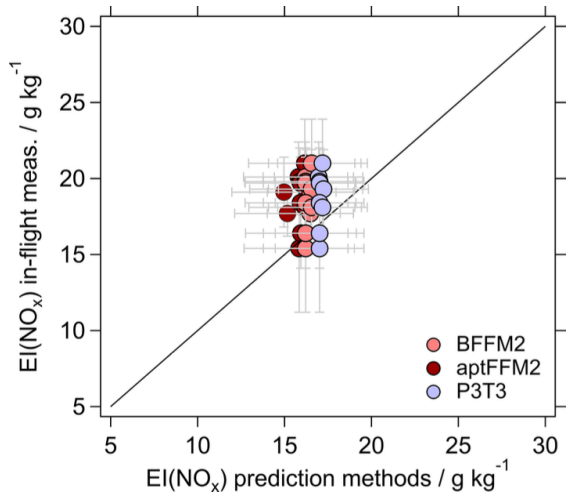

Figure 3.5: Comparison of EI(NO_x measurements to estimated EI(NO_x values from BFFM2. Figure taken from Harlass et al. [20].

The A359 in the measurement data shown in Figure 3.5 is equipped with a pair of modern RQL engines, Trent XWB-84. When it comes to NO_x emissions of lean-burn engines, using TAPS technology, for example, the BFFM2 method may slightly overestimate the cruise emissions. Comparing Figure 3.6 and Figure 3.7, a clear difference in trend can be observed. This is important as the cruise thrust setting finds itself between 40% and 80% thrust.

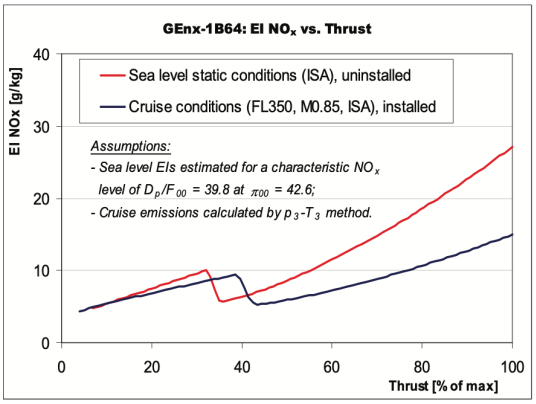

Figure 3.6: EI(NO_x) compared to thrust setting using the p3-T3 method of the GEnx TAPS combustor engine. Figure taken from Schaefer et al. [45].

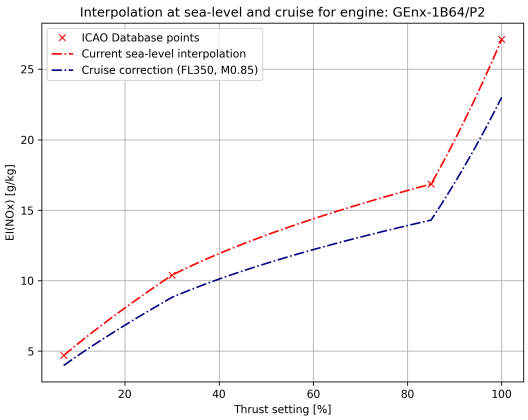

Figure 3.7: EI(NO_x) compared to thrust setting using the BFFM2 method of the GEnx TAPS combustor engine.

However, no large-scale study on a fuel flow method adaptation or correction for lean-burn engines currently exists, and validating such a method would require in-flight measurement campaigns on lean-burn technology engines. Thus, this research will stick to the BFFM2 as applied in other studies.

3.7. Research Questions

The ultimate goal of an emission inventory is to estimate the emissions as accurately as possible to provide a reliable climate impact assessment. As such, the goal of this research is to evaluate and improve the existing implementations of aviation emission inventories for more accurate emission estimates, while maintaining computational efficiency.

This leads to the main research question: **To what extent can the current emission inventory be improved through the use of updated methods for performance and emission modelling, without compromising on computational efficiency?** A series of three sub-questions can be formulated to help achieve this main goal:

1. What performance model inputs are the results most sensitive to?
2. What is the updated uncertainty of the model?
3. How do the improvements impact the global emission estimate and how do they compare to current emission inventories?

4

Methodology

To achieve the goal of the research effectively, a methodology has to be put in place. This section gives an overview of the steps that will be taken to answer the research questions mentioned previously. This research plans to use data generated through the research of Teoh et al. [60] as they have provided an expansive database of information openly.

4.1. Engine Assignment

The first aspect covered in the methodology is the market share analysis and the incorporation of an aircraft-route pair-specific engine distribution.

As discussed in section 3.1, it is common for an aircraft to come in different configurations, which may come with different engines, to meet the goal of the airline or customer. To mediate this, a market share analysis was performed. This was done using the OpenSky Network aircraft database, which agglomerates national registry data[1]. The procedure also involves the flight schedule database provided by FlightRadar24, currently used to determine the aircraft-route pairs. This database also includes information on the aircraft registration number, however, it lacks engine data for the specific aircraft. This is where the OpenSky Network aircraft database is used, as it provides engine data for particular aircraft, identified with their registration number. This procedure is best illustrated with the help of Figure 4.1.

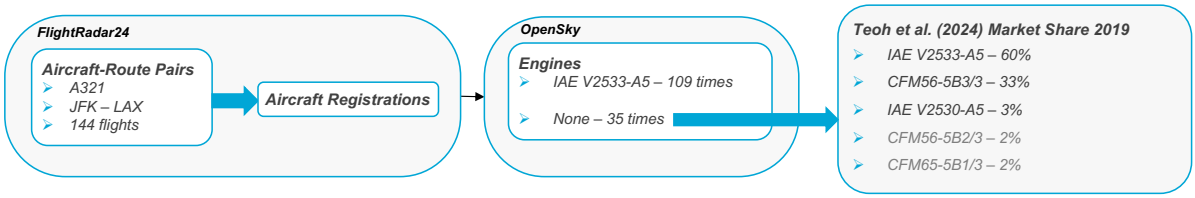

Figure 4.1: Engine allocation procedure per aircraft route pair.

The A321 is a common aircraft flown across different continents, with varied configurations, and the route JFK - LAX using the A321 is the most flown route covered in the representative week, when considering flown kilometres. In Figure 4.1, there is a possibility that a given registration is missing engine information, in which case the market share analysis performed by Teoh et al. [59] is used to cover the remaining engine locations. If Teoh et al.'s market share does not cover the aircraft, the BADA engine is used. The market share analysis by Teoh et al. remains important even after the OpenSky Network market share analysis, as coverage is limited within OpenSky, and even with covered aircraft, some do not include a valid engine. This is illustrated by the share each source has in determining the selected engine shown in Figure 4.2. In contrast, the current implementation solely takes one engine, thus the distribution is simply 100%.

The next aspect that must be considered is incorporating this engine share per aircraft-route pair in the emission calculations. The emissions are greatly dependent on the engine. Each engine will have a different set of measured emission indices and a different fuel consumption. Thus, the average emission

[1]Confirmed through internal communication with Dr. J. Sun at the TUDelft.

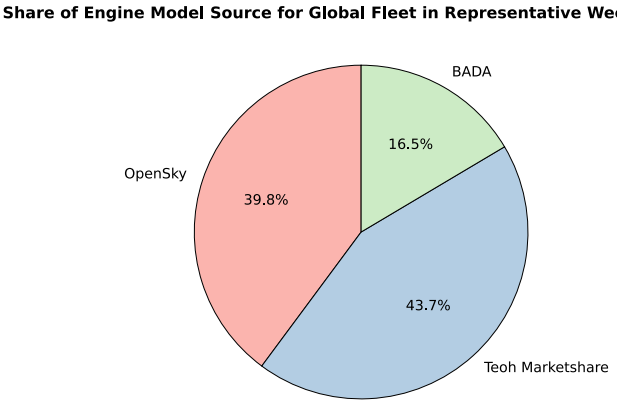

Figure 4.2: Pie chart illustrating the share of engines from each source.

index of all the engines used on this specific aircraft-route pair is taken for the emission calculations, as described by Equation 4.1.

$$EI = \sum_{k}^{n} EI_k \cdot p_k \tag{4.1}$$

Where n is the number of engines, k is the specific engine and p is the percentage of the total share of engine k.

4.2. Flight Trajectory and Altitude

As discussed in section 3.1, the flight trajectory is currently taken as the great circle distance corrected by a lateral inefficiency based on data from 23 flights. From these 23 flights, two correction factors are determined, one for short-haul, and another for long-haul flights. However, with ADS-B data, it is possible to analyse a greater number of trajectories to determine more accurate multipliers.

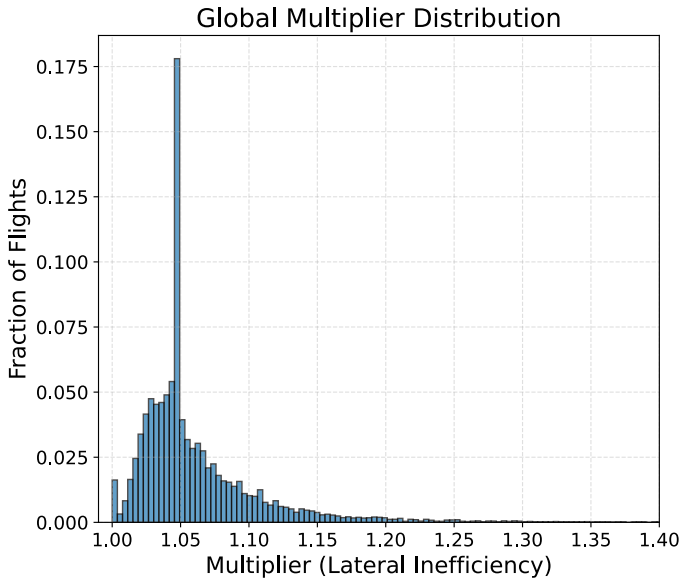

Figure 4.3: Distribution of multipliers acquired from Teoh et al. supplementary data [59].

For the calendar year 2019, this analysis has already been performed by Teoh et al. [60], with the data being publicly available. The multipliers are presented as mean multipliers for routes between two airports, as well as between two countries. These multipliers are therefore incorporated into the

inventory presented in this research. When the multiplier for a given route is not available, the multiplier between the countries where the two airports are located is used. The updated distribution of lateral inefficiency multipliers is given in Figure 4.3.

In terms of flight altitude, the dynamic allocation of flight altitude through the use of ROC threshold is kept, however, the values themselves are updated, as well as the method of allocation. These new ROC threshold values are determined through observation of the FlightRadar24 publicly available playback feature, provided up to 7 days after the flight. The flight number and date are recorded for reproducibility. From these observations, the start of cruise altitude is recorded, and an analysis is performed to assess for each aircraft-route pair the associated ROC threshold. As the flight altitude can vary depending on range, four range categories are determined, and the mean ROC threshold for each range category is selected for use in the updated emission inventory. These are provided in Table 4.1.

Table 4.1: ROC threshold values based on aircraft range from FR24 analysis.

Range category	Flight distance range [nm]	ROC threshold [ft/min]
Regional	< 300	1545
Short	300 - 1000	1107
Medium	1000 - 2000	982
Long	> 2000	668

The full distribution of the ROC threshold values is discussed further in the uncertainty analysis section of the report (chapter 6).

4.3. Performance Model

The BADA4 performance model, described in section 2.2, is applied to the current inventory, where possible, and BADA3 is used to complete the analysis for aircraft not yet available in BADA4 (found to be 11% of the total distance flown). As mentioned in section 3.1, BADA4 contains files for different variants of an aircraft based on the engine model, as illustrated in Figure 3.3 [35] [36]. Thus, for each aircraft-route pair and for each engine provided by the market share analysis (Figure 4.1), the corresponding aircraft file is determined. The engines corresponding to each file are recorded, and the route is assessed once per aircraft file, and the outcome is multiplied by the total number of flights associated with each file for that route.

In each case, the Total Energy Model (TEM) described in section 2.2 is used for computing aircraft performance across all CCD flight phases. These include thrust, drag, airspeed, fuel consumption, and climb/descent rates, all parameters displayed in Equation 4.25. The working principle of the method is the same for both BADA3 and BADA4.

The TEM relies on aircraft performance parameters extracted from the BADA files, which provide:

- Aircraft mass parameters
- Flight envelope parameters
- Aerodynamic coefficients
- Thrust coefficients
- Fuel consumption coefficients

Afterwards, each parameter in Equation 4.25 can be determined, as well as the fuel consumption.

Thrust Computation

The thrust calculation in the model differs between BADA4 and BADA3. In BADA4 [35], the available thrust is obtained by scaling a non-dimensional thrust coefficient C_T by the local pressure ratio δ, the reference mass and gravity:

$$T = \underbrace{\frac{p}{p_0}}_{\delta} \underbrace{m_{\text{ref}}\, g}_{\text{weight scale}} \; C_T. \tag{4.2}$$

The thrust coefficient itself is a double polynomial in Mach and *throttle setting* $\Delta\tau$:

$$C_T = \sum_{k=0}^{5} \sum_{j=0}^{5} a_{6k+j}\, M^j\, (\Delta\tau)^k, \tag{4.3}$$

where a_i $(i = 0, \ldots, 35)$ are the thrust coefficients retrieved from the BADA file.

The throttle setting $\Delta\tau$ is also computed as a double polynomial in Mach number M and pressure ratio δ:

$$\Delta\tau = \sum_{k=0}^{5} \sum_{j=0}^{5} c_{6k+j}\, M^j\, \delta^k, \tag{4.4}$$

where

- c_i $(i = 0, \ldots, 35)$ are the throttle coefficients,
- j indexes powers of M (from 0 to 5),
- k indexes powers of δ (from 0 to 5).

Thus, overall, the required inputs from the BADA 4 file [35] are:

- Throttle coefficients $\{c_0, \ldots, c_{35}\}$
- Thrust coefficients $\{a_0, \ldots, a_{35}\}$
- Mach number M
- Ambient pressure p and sea-level p_0
- Reference mass m_{ref} and gravitational acceleration g

A different set of thrust and throttle coefficients exists for different engine settings, and for climb the set corresponding to maximum climb (MCMB) is taken. In descent, the idle rating coefficients are selected. In cruise, the thrust is set to equal the drag.

In BADA3, the method differs [36]. In climb, the maximum thrust is also determined; however, in this case, the relation has fewer coefficients and parameters:

$$(T_{\text{max,climb}})_{\text{ISA}} = C_{T,c1} \cdot \left(1 - \frac{h_{\text{feet}}}{C_{T,c2}} + C_{T,c3} \cdot h_{\text{feet}}^2\right), \tag{4.5}$$

where $C_{T,c1}$, $C_{T,c2}$, and $C_{T,c3}$ are thrust coefficients obtained from the BADA OPF file, and h_{feet} is the altitude in feet.

For cruise and descent phases, thrust is computed as:

$$T_{\text{cruise}} = \min(C_{T,cr} \cdot T_{\text{max,climb}}, D_{\text{cruise}}), \tag{4.6}$$

where $C_{T,cr} = 0.95$ is a cruise thrust reduction factor and D_{cruise} is the drag experienced during cruise.

Similarly, descent thrust is calculated using:

$$T_{\text{des}} = C_{T,des} \cdot T_{\text{max,climb}}, \tag{4.7}$$

where $C_{T,des}$ is an altitude-dependent coefficient that scales thrust for descent.

Aerodynamics Computations

The aerodynamic forces are computed based on lift and drag coefficients [36][35]. The drag force is given by:

$$D = C_D \frac{\rho V_{\text{TAS}}^2 S}{2}, \tag{4.8}$$

where C_D is the drag coefficient, ρ is the air density, V_{TAS} is the true airspeed, and S is the wing reference area.

The drag coefficient computation is where the methods differ. In BADA4, the drag coefficient C_D uses a Mach-dependent drag polar of the form

$$C_0(M) = b_1 + \frac{b_2}{\sqrt{1-M^2}} + \frac{b_3}{1-M^2} + \frac{b_4}{(1-M^2)^{3/2}} + \frac{b_5}{(1-M^2)^2}, \tag{4.9}$$

$$C_2(M) = b_6 + \frac{b_7}{(1-M^2)^{3/2}} + \frac{b_8}{(1-M^2)^3} + \frac{b_9}{(1-M^2)^{9/2}} + \frac{b_{10}}{(1-M^2)^6}, \tag{4.10}$$

$$C_6(M) = b_{11} + \frac{b_{12}}{(1-M^2)^7} + \frac{b_{13}}{(1-M^2)^{15/2}} + \frac{b_{14}}{(1-M^2)^8} + \frac{b_{15}}{(1-M^2)^{17/2}}, \tag{4.11}$$

$$C_D = b_0 \left[C_0(M) \; + \; C_2(M)\, C_L^2 \; + \; C_6(M)\, C_L^6 \right], \tag{4.12}$$

where $\{b_0, \ldots, b_{15}\}$ are the drag-polynomial coefficients extracted from the aircraft file [35].

In the case where the aircraft is not in clean configuration (only possible in approach conditions between 3000 and 8000 ft in the descent phase), the following equation is used:

$$C_D = d_1 + d_2 C_L + d_3 C_L^2, \tag{4.13}$$

where d_1, d_2, d_3 are non-clean drag coefficients for the approach condition [35].

Again, BADA3 uses a simpler method, where the drag coefficient is computed as:

$$C_D = C_{D0} + C_{D2} C_L^2 \tag{4.14}$$

where C_{D0} is the zero-lift drag coefficient and C_{D2} is the induced drag coefficient, extracted from the aircraft file. These also depend on aircraft configuration, but again, in CCD, it is almost always clean [36].

The lift coefficient in both cases is determined by:

$$C_L = \frac{2mg}{\rho V_{\text{TAS}}^2 S} \tag{4.15}$$

where C_L is the lift coefficient, ensuring equilibrium between aerodynamic lift and aircraft weight [36].

Airspeed Determination

True airspeed V_{TAS} is determined by correcting calibrated airspeed V_{CAS} to the appropriate atmospheric conditions. The correction from calibrated airspeed to true airspeed is achieved through Equation 4.16.

$$V_{\text{TAS}} = \left[\frac{2p}{\mu\rho} \left\{ 1 + \frac{(p_0)_{\text{ISA}}}{p} \left[\left(1 + \frac{\mu}{2} \frac{(\rho_0)_{\text{ISA}}}{(p_0)_{\text{ISA}}} V_{\text{CAS}}^2 \right)^{\frac{1}{\mu}} - 1 \right]^{\mu} - 1 \right\} \right]^{\frac{1}{2}} \tag{4.16}$$

The selection of V_{CAS} follows:

1. $V_{\text{CAS}} = 1.3 V_{\text{stall}} \frac{m}{m_{\text{ref}}} + dV$
2. $V_{\text{CAS}} = \min(V_{\text{CAS,LO}}, V_{\text{other}})$
3. $V_{\text{CAS}} = V_{\text{CAS,HI}}$
4. Mach-limited speed

where V_{stall} is the stall speed, m_{ref} is the reference mass, and dV is an adjustment factor. Table 4.2 illustrates more precisely the different calibrated airspeeds based on altitude range and flight phase.

[1] Transition altitude corresponds to the altitude where $V_{\text{CAS,HI}}$ and M_{phase} lead to the same V_{TAS}.

[2] This value corresponds to BADA4; in BADA3, this value is 220 kt.

Table 4.2: Speed Schedule by Flight Phase and Altitude used in BADA3 [36] and BADA4 [35].

	Climb	Cruise	Descent
3,000 to 3,999 ft	$1.dV = 30$ kt	$2.\min(V_{\text{CAS,LO}}, 220\text{ kt})$	$2.\min(V_{\text{CAS,LO}}, 180\text{ kt}^2)$
4,000 to 4,999 ft	$1.dV = 60$ kt	$2.\min(V_{\text{CAS,LO}}, 220\text{ kt})$	$2.\min(V_{\text{CAS,LO}}, 180\text{ kt}^2)$
5,000 to 5,999 ft	$1.dV = 80$ kt	$2.\min(V_{\text{CAS,LO}}, 220\text{ kt})$	$2.\min(V_{\text{CAS,LO}}, 180\text{ kt}^2)$
6,000 to 9,999 ft	$2.\min(V_{\text{CAS,LO}}, 250\text{ kt})$	$2.\min(V_{\text{CAS,LO}}, 250\text{ kt})$	$2.\min(V_{\text{CAS,LO}}, 250\text{ kt})$
10,000 ft to 13,999 ft	$3.V_{\text{CAS,HI}}$	$2.\min(V_{\text{CAS,LO}}, 250\text{ kt})$	$3.V_{\text{CAS,HI}}$
14,000 ft to transition [1]	$4.M_{\text{cl}}$	$3.V_{\text{CAS,HI}}$	$4.M_{\text{des}}$
Above transition	$4.M_{\text{cl}}$	$4.M_{\text{cr}}$	$4.M_{\text{des}}$

Fuel Consumption Computation

Similarly to the thrust and drag, in BADA4 [35], the fuel mass flow rate $\dot{m}_f$ [kg/s] is obtained by scaling a non-dimensional fuel coefficient C_F by pressure ratio, temperature ratio, reference mass and lower heating value (LHV):

$$\dot{m}_f = \delta \sqrt{\theta}\, \frac{m_{\text{ref}}\, g\, a_0}{\text{LHV}}\, C_F, \quad \delta = \frac{p}{p_0},\ \theta = \frac{T}{T_0}. \tag{4.17}$$

This fuel coefficient is selected as the larger of the two following coefficients, idle and rated fuel coefficients, $C_{F,\text{idle}}$ and $C_{F,\text{gen}}$:

$$C_F = \max\left(C_{F,\text{idle}},\, C_{F,\text{gen}}\right). \tag{4.18}$$

The idle coefficient is a polynomial in Mach M and pressure ratio δ:

$$C_{F,\text{idle}} = \frac{p_0}{p} \sqrt{\frac{T_0}{T}} \sum_{k=0}^{2} \sum_{j=0}^{2} f_{kj}\, \delta^k\, M^j, \tag{4.19}$$

where f_{kj} $(k, j = 0, 1, 2)$ are the idle fuel-flow coefficients from the aircraft file. When a rating other than idle is selected, a polynomial in thrust coefficient C_T and Mach is used:

$$C_{F,\text{gen}} = \sum_{k=0}^{4} \sum_{j=0}^{4} g_{kj}\, C_T^k\, M^j, \tag{4.20}$$

where g_{kj} $(k, j = 0 \ldots 4)$ are the fuel-flow coefficients at climb/cruise rating.

Summarising, in BADA4 [35] the required inputs are as follows:

- Idle coefficients $\{f_{kj}\}$ from the `CF_idle` block.
- Generated coefficients $\{g_{kj}\}$ from the `CF_gen` block.
- Thrust coefficient C_T, Mach M.
- Ambient pressure p, temperature T; sea-level p_0, T_0.
- Reference mass m_{ref}, gravity g, speed of sound at sea-level a_0.
- Fuel lower heating value LHV.

In BADA3 [36], the fuel mass flow rate is determined from thrust-specific fuel consumption (TSFC), defined as:

$$\eta = C_{f1} \left(1 + \frac{V_{\text{TAS}}}{C_{f2}}\right) \tag{4.21}$$

where η is the TSFC correction factor, and C_{f1} and C_{f2} are aircraft-dependent TSFC coefficients.

This leads to fuel flow computations for climb and cruise phases:

$$\dot{m}_{f,\text{climb}} = \eta T \tag{4.22}$$

$$\dot{m}_{f,\text{cruise}} = \eta T C_{T,cr} \tag{4.23}$$

where f_{climb} and f_{cruise} represent the rate of fuel consumption in climb and cruise phases, respectively. $C_{T,cr}$ is an aircraft-dependent cruise thrust correction factor.

For descent, fuel flow is computed as:

$$\dot{m}_{f,\text{min}} = C_{f3}\left(1 + \frac{h}{C_{f4}}\right) \tag{4.24}$$

where C_{f3} and C_{f4} are coefficients that depend on altitude.

Rate of Climb and Descent (ROCD)
The rate of climb or descent is derived from the energy balance equation:

$$\frac{dh}{dt} = \frac{(T-D)V_{\text{TAS}}}{mg}\left(1 + \frac{V_{\text{TAS}}}{g}\frac{dV_{\text{TAS}}}{dh}\right)^{-1} \tag{4.25}$$

where $\frac{dh}{dt}$ is the rate of climb or descent, and g is the gravitational acceleration. The left-hand side of Equation 4.25 can be split into two main terms. The first is the available energy resulting from the additional thrust after accounting for drag, and the second is the energy required to accelerate and maintain the set calibrated airspeed in climb. This second term can be seen as an energy share factor, shown in Equation 4.26.

$$f\{M\} = \left(1 + \frac{V_{\text{TAS}}}{g}\frac{dV_{\text{TAS}}}{dh}\right)^{-1} = \left\{1 + \frac{\gamma R k_T}{2g}M^2 + \left(1 + \frac{\gamma-1}{2}M^2\right)^{\frac{-1}{\gamma-1}}\left[\left(1 + \frac{\gamma-1}{2}M^2\right)^{\frac{\gamma}{\gamma-1}} - 1\right]\right\}^{-1} \tag{4.26}$$

When the speed schedule follows a constant Mach number, however, the equation is simplified (Equation 4.27, as the change in Mach with altitude no longer needs to be accounted for.

$$f\{M\} = \left\{1 + \frac{\gamma R k_T}{2g}M^2\right\}^{-1} \tag{4.27}$$

Implementation
Finally, combining all the steps discussed above, an overview of the flow of the performance model can be reassessed. This is illustrated by Figure 4.4.

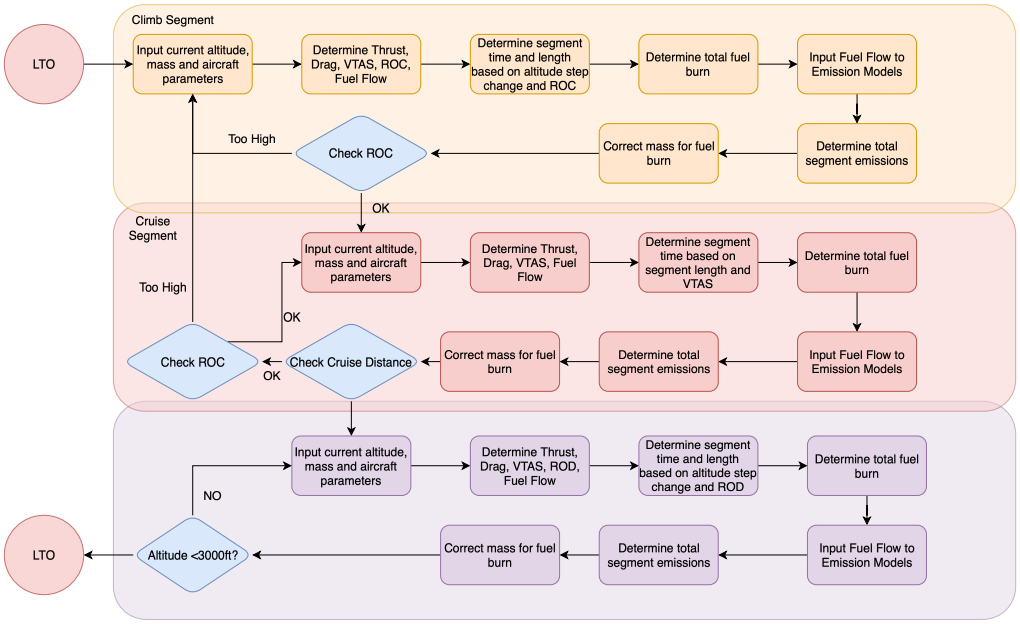

Figure 4.4: Performance model flow chart using the total energy method

4.4. Emission Model

From the research gaps discussed in section 3.1, it is clear that the emission model for nvPM emissions must be updated. It was decided to follow the MEEM approach, as it was derived by minimising error for a large set of engines, whereas other methods often focus on a single engine type. As the approach has not been implemented in any of the three inventories for the year 2019, its implementation in the current inventory enables an updated estimation of global nvPM emissions.

As mentioned previously, the MEEM method applies the FOA4 method in the case where only the smoke number is present in the ICAO databank. Thus, methodology follows the steps listed out in section 2.2 for the FOA4 method and the MEEM method.

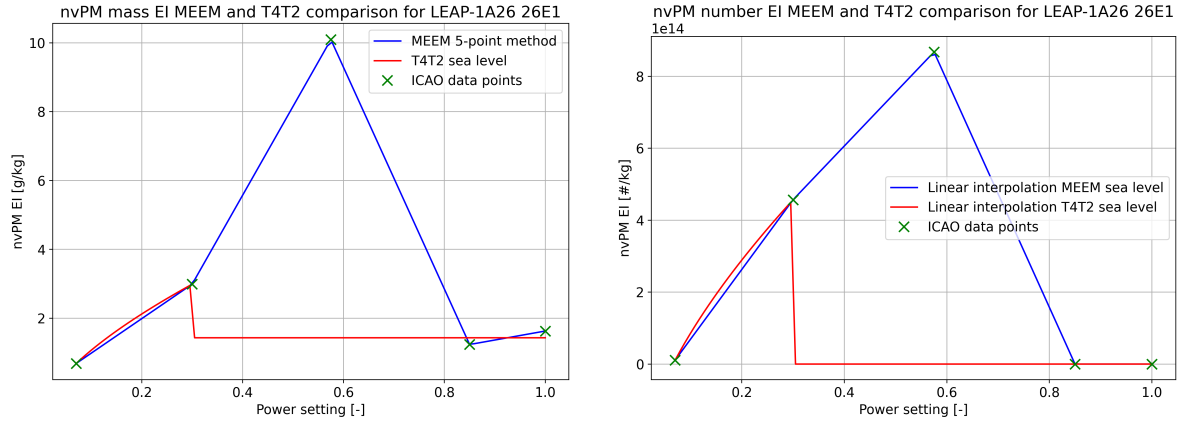

Figure 4.5: Comparison of nvPM mass EI (left) and number EI (right) from T4T2 method with step change vs MEEM 5-point method for LEAP-1A26.

One element of the MEEM method is updated in the current implementation. For engines equipped with lean-burn technology combustors, such as DAC and TAPS, an approach similar to that of Teoh et al. is used. Indeed, as mentioned in section 2.2, and shown in Figure 2.9, there is a clear step change in the nvPM emissions after the pilot stage. As such, Teoh et al. set a step change in their interpolation method, where after 30% thrust setting, the nvPM EI value is set as the average between 85% and 100% thrust setting. On the other hand, the MEEM 5-point method performs a linear interpolation up to the maximum measured point, fixed at 57.5% thrust setting. The specific engine variant used in Figure 2.9 is not available in the ICAO databank, so a LEAP-1A26 with TAPS combustor technology is selected for comparison in Figure 4.5.

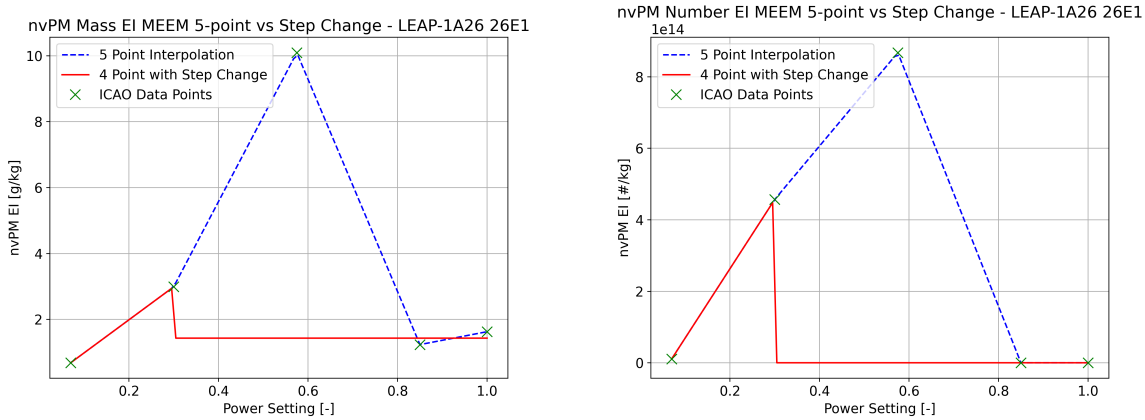

Figure 4.6: Comparison of nvPM mass EI (left) and number EI (right) between MEEM 5-point method and MEEM 4-point with step change for LEAP-1A26.

From Figure 4.5 it can be seen that the maximum measurement point from the ICAO databank may overestimate the cruise emissions of the TAPS combustor. Accordingly, a step change is performed as 30% thrust, as illustrated in Figure 4.6.

In the case of NO_x emissions, as mentioned in section 3.1, the current BFFM2 is kept in the main analysis.

4.5. Sensitivity Analysis

As part of this study, to better understand the impact of model assumptions and inputs, a sensitivity analysis is performed. This is done by systematically varying critical parameters within the performance model. The objective is to quantify how changes in these input parameters affect the predicted flight altitudes, fuel consumption, and resulting emission indices, including nvPM and NOx.

The sensitivity analysis specifically investigates the following parameters:

1. **Payload Factor:** The payload factor is varied within a range of ±10%. Quadros et al. [44] assess the sensitivity of the same parameter within a range of ±7%. This is for a single factor of 0.628 irrespective of range; thus, a broader range is selected in this study, ensuring coverage of realistic payload variations for both short-haul (0.741) and long-haul flights (0.689).
2. **Empty Weight Factor:** The operational empty mass (OEM) of aircraft, known to vary significantly based on aircraft type and configuration, is adjusted by ±5% to capture typical variations in empty weight across different wake types.
3. **ROC Threshold:** This parameter directly influences the cruise altitude determination. It is varied by ±25% to examine its sensitivity and the associated impact on cruise flight altitude.
4. **Initial Fuel Mass:** The initial fuel mass is intrinsically linked to the chosen initial flight altitude. To explore this relationship, the initial altitude is offset from the ceiling altitude using discrete altitude variations ranging from −9000 ft to −3000 ft. This provides insights into how initial altitude assumptions propagate into fuel consumption and emission predictions. The bounds were selected based on commonly observed cruise altitudes for jet aircraft, which are found between 30000 and 40000 feet.

By varying these parameters within their specified ranges, the sensitivity analysis identifies the most influential assumptions on emission estimates. This gives insight into which parameters should be more accurately represented in future research and studies.

4.6. Uncertainty Analysis

After the revision of the emission inventory, an updated uncertainty analysis must be performed. The purpose of the uncertainty analysis is to assess the confidence in the results and compare whether the improvements to the method lead to a change in the uncertainty.

To assess the uncertainty of the model, the distribution of possible values of the parameters must be assessed. For the parameters unchanged in the updated inventory, the uncertainty distributions of Rik Kroon [30] will be kept. This leaves the following parameters:

1. **Engine Selection:** As mentioned previously in section 4.1, not all flights in the database have an engine associated with them. Figure 4.2 showed that about 60% of the total flown distance does not have an associated engine, leading to uncertainty in the engine assignment. As discussed throughout the study, different engine models can have drastically different emission profiles. Furthermore, in the case of BADA4, the specific engine assigned to a route affects the performance data used. An analysis performed internally within the TUDelft using EASA registration data gives an alternate engine market share to the one currently performed. This market share will be used as the base for the uncertainty analysis.
2. **Lateral Inefficiency:** The data made available by Teoh et al. [60] will be used to determine the lateral inefficiency multipliers based on ADS-B data. The uncertainty associated with this will be assessed using the distribution of multipliers for different range categories based on their data.
3. **Flight Altitude :** The flight altitude uncertainty will be assessed through the ROC threshold. Indeed, in this model, the ROC threshold is used as a measure for flight altitude, and the distributions of ROC threshold associated with the flight altitude observations from the FlightRadar24 data will be assessed.
4. **Fuel Consumption :** The uncertainty in the fuel consumption will be assessed using the RMSE associated with the fuel consumption value calculated using BADA4 for each flight phase. These values are provided for each aircraft included in BADA4.
5. **nvPM Emissions:** Similarly to the BADA4 fuel uncertainty, the uncertainty associated with the nvPM emissions will be assessed through the error analysis provided in the MEEM method paper. This will be done per emission type (mass and number) and phase (climb/descent and cruise).

6. **Mass Estimations:** The operating empty mass of the aircraft in Rik Kroon's inventory was selected as a single value for all aircraft and the uncertainty analysis was performed on this value. In another analysis performed internally at the TUDelft, the operating empty mass has been reclassified into categories based on aircraft wake type. The uncertainty associated with these masses will be assessed in this updated uncertainty analysis.

Monte Carlo simulations will be employed to quantify the overall uncertainty in the emission inventory. This statistical approach allows for the modelling of uncertainties in input parameters and their propagation through the emission estimation process.

The first step leading to the Monte Carlo simulations is to define probability distributions for the parameters listed above. This is done by first determining a feasible histogram, following Scott's rule (Equation 4.28) [9][50], then attempting to fit a probability density function (PDF) to the data. The two can be compared visually, and a statistical test can be performed to assess how well the PDF fits the data.

$$w_{\text{bin}} = 3.49 \cdot \sigma \cdot n^{\frac{1}{3}}, \tag{4.28}$$

where w_{bin} is the bin width, σ is the standard deviation, and n is the sample size.

The statistical test performed is an Anderson-Darling (AD) goodness-of-fit test. It is one of the most commonly used in statistics and the base method in SciPy's statistics library. The idea of the AD test is that a null hypothesis, which states that the PDF represents the sample of size n. The deviation between this PDF and the sampled data is calculated and represented by the A^2 statistic. For an ordered sample $(x_1 < x_2 < ... < x_n)$, the statistic is computed as follows:

$$A^2 = -\frac{1}{n} \sum_{i=1}^{n} [(2i-1)(\ln(F_X(x_i) + \ln(1 - F_X(n+1-i)))] - n. \tag{4.29}$$

A correction is also applied, as in the case of this study, the mean and standard deviation of each distribution are estimated from the data [13].

$$A^* = A^2 \left(1 + \frac{0.75}{n} + \frac{2.25}{n^2}\right) \tag{4.30}$$

Then for a selected significance level (5% in the case of this work), it is assessed whether the null hypothesis is rejected or not, i.e. whether the PDF reasonably represents the data. For a significance level of 5%, the A^* value must be ≤ 0.752, otherwise the discrepancy between the sample data and the distribution is too large and the null hypothesis is rejected [13].

Once the PDFs are determined, a large number of simulation runs are conducted, each time randomly sampling from the defined parameter distributions. This process will generate a range of possible outcomes, providing a comprehensive view of the uncertainty in the emission estimates. These outputs can then be analysed to determine the confidence intervals of the inventory results. This gives a broader picture of the possible range of emissions, resulting from the model assumptions and input uncertainties.

Following this methodology, the necessary results and analysis will be provided to answer the research questions posed in section 3.7.

5

Performance Model Sensitivity Analysis

This chapter examines how key assumptions in the global aviation emissions inventory model influence flight performance and pollutant outputs. section 5.1 presents the input parameters and output results that are assessed. The effects of mass and altitude on the performance and emissions are discussed in section 5.2. The results of the sensitivity study are presented in section 5.3. Finally, a summary of this chapter is provided in section 5.4.

5.1. Parameters & Metrics

The main goal of the sensitivity analysis is to analyse two essential aspects of the performance model: the aircraft mass and the cruise altitude. As mentioned previously, the take-off mass of the aircraft is estimated as TOM = OEM + $M_{payload}$ + M_f. Each of these masses is itself estimated or assumed, and thus has some form of uncertainty associated with it. As mentioned in chapter 4, the sensitivity of the results on the choice of the parameter must be assessed. The second parameter is ROC threshold, which as mentioned in chapter 4, directly influences the cruise altitude of the aircraft. Table 5.1 summarises the tested parameter ranges. For the initial fuel mass, the range depends on the initial flight altitude used to estimate the initial fuel mass. The effect of this is summarised in Table 5.2 for Wake Type M.

Table 5.1: Input parameters for the sensitivity analysis along with their respective variation ranges.

Parameter	Range
Assumed Initial Altitude Offset [ft] [1]	-9000 to -3000
Payload Factor	-10% to +10%
Empty Mass Factor	-5% to +5%
ROC Threshold	-25% to +25%

The corresponding model outputs examined are:

- Cruise altitude
- Fuel consumption
- Emission indices: NO_x and nvPM specifically

The initial fuel mass is estimated by assuming the aircraft will cruise at a certain altitude, from departure to arrival, at MTOM. This altitude is an offset from the maximum altitude of the aircraft (currently -7000ft). Therefore, the variation altitude is altered, as it is the true input, and its direct effect on the initial fuel mass is analysed. The change in fuel mass resulting from this influences the take-off mass (TOM), which influences cruise altitude, fuel burn, and emissions and the cruise altitude through its impact on climb performance.

[1] The initial altitude assumption is taken as 7000 [ft] below the operating ceiling altitude of the specific aircraft, provided in BADA.

Because this analysis is performed on parameters which are assigned based on aircraft category, the sensitivity is assessed per wake types M and H (except for payload factor, which is set based on range, with the short range (< 1000 nm) assessed alongside type M aircraft, and the long range (≥ 1000 nm) alongside type H aircraft). For each aircraft, the wake type is provided by BADA [36], following from the ICAO Aircraft Type designators. There exist other wake types, however, they account for less than 2% of the total distance travelled.

5.2. Effects of Mass and Altitude on Performance and Emissions

The influence of aircraft mass and flight altitude on fuel burn and emissions operates through multiple mechanisms, dependent on the performance model. The aircraft mass has the following influence:

- In the climb phase, thrust is set independently of mass, and fuel flow is not directly affected. However, mass influences lift (C_L) and therefore drag, reducing ROC at higher mass.
- The equation $T = \frac{p}{p_0} m_{\text{ref}} g C_T(M)$ defines thrust as a function of Mach number, where C_T depends on flight conditions.
- A lower ROC due to higher mass results in reduced cruise altitudes, which affects overall fuel consumption, as illustrated by Figure 5.1.
- In cruise, where $T = D$, higher mass leads to higher drag and therefore increased fuel flow.

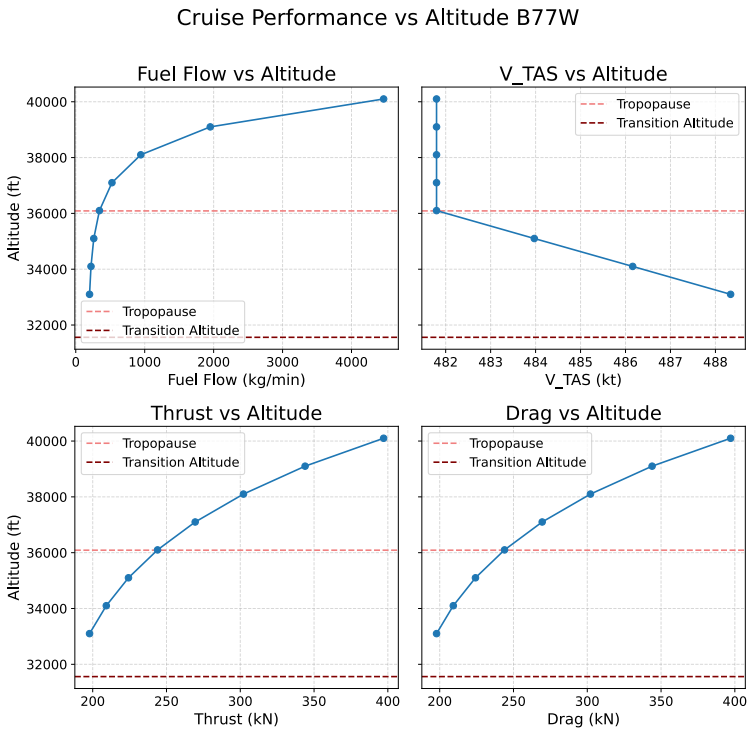

Figure 5.1: Cruise performance parameters at various altitudes using BADA4 for an example Boeing 777-300 aircraft.

In Figure 5.1, transition altitude represents the altitude above which the aircraft flies at its cruise Mach number within the BADA performance model. For the B777-300, this corresponds to a Mach number of 0.84. The thrust corresponds to aircraft thrust, thus incorporates the thrust generated by both engines, and the same holds for the fuel flow.

Additionally, drag is seen to increase with altitude. Generally drag decreases as altitude increases. However, in some cases, for a given weight and specific speed schedule (as in the BADA performance model), the opposite may happen. If the density and speed are too low to maintain sufficient lift, the lift coefficient must increase, which increases drag, thrust and fuel consumption. This is illustrated in Figure 5.2.

Regarding the flight altitude, the changes influence fuel burn and emissions in the following manner:

- Airspeed is altitude-dependent, affecting drag via both density and velocity.
- Drag directly affects fuel consumption in cruise, as explained previously and shown in Figure 5.1.
- Using MEEM, nvPM EI is independent of the fuel flow in the performance model, as the method directly estimates thrust setting based on Mach and altitude.
- Using BFFM2, NO_x EI (as well as CO and HC) is sensitive to both fuel flow and altitude. The effect is both direct (via temperature and pressure correction) and indirect (due to variation in fuel burn).

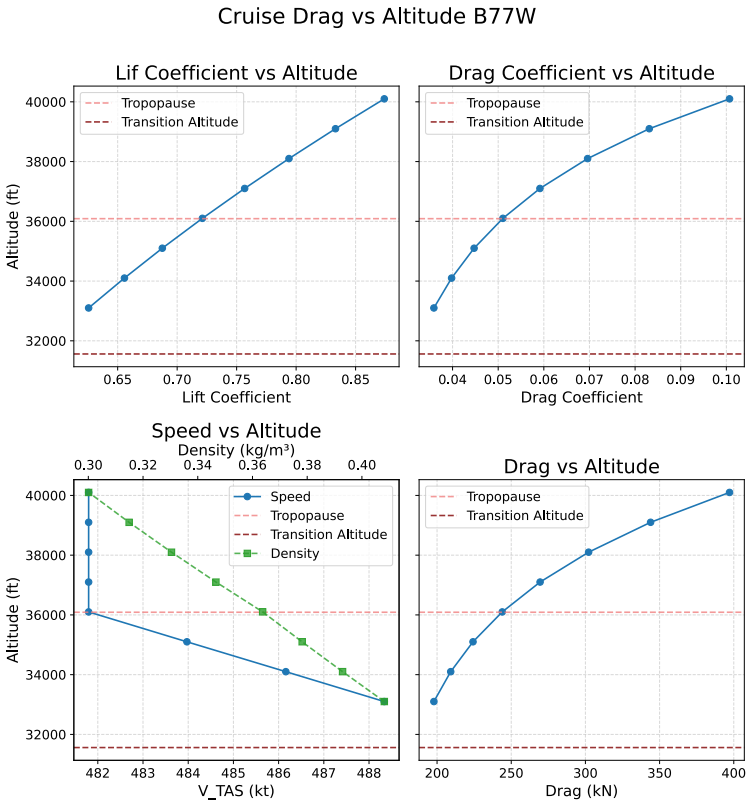

Figure 5.2: Cruise drag parameters at various altitudes using BADA4 for an example Boeing 777-300 aircraft

The interaction between fuel burn, altitude, and emission indices is nuanced:

- Higher cruise altitudes affect fuel consumption depending on aircraft design and atmospheric conditions.
- Emissions at higher altitudes vary depending on thrust setting, the time spent in climb/descent, and the engine type.
- Generally, an increase in fuel burn leads to higher NO_x EI as per the BFFM2.
- For nvPM, EI may increase or decrease with fuel flow depending on engine type, as its formation mechanism depends on combustor technology. This is illustrated in Figure 5.3

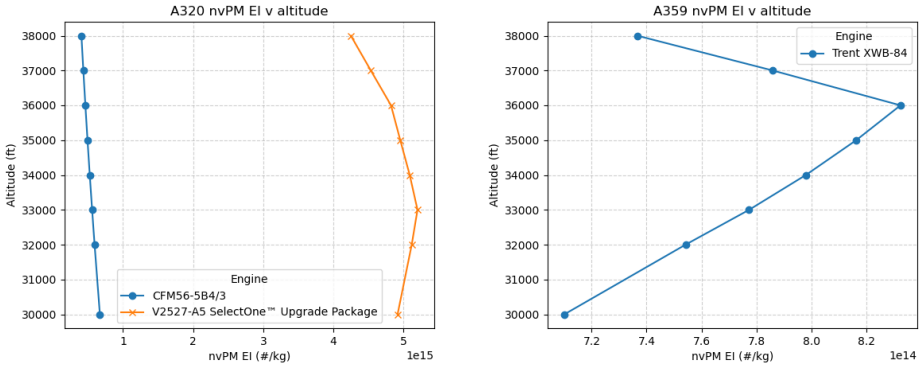

(a) A320-200 nvPM EI vs. altitude

(b) A350-900 nvPM EI vs. altitude

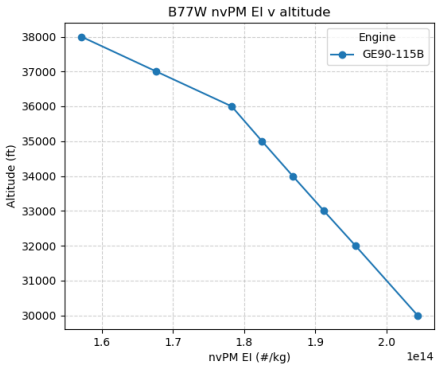

(c) B777-300 nvPM EI vs. altitude

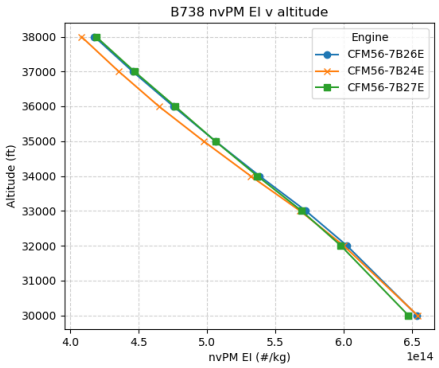

(d) B737-800 nvPM EI vs. altitude

Figure 5.3: nvPM number EI as a function of cruise altitude for different aircraft and engine combinations ((a) A320, (b) A359, (c) B77W, (d) B738).

5.3. Sensitivity Analysis Results

This section presents the sensitivity analysis results, split by wake type (M and H). Firstly, the range of initial fuel mass and corresponding take-off mass for the different variation altitudes is presented in Table 5.2 for wake type M, and Table 5.3 for wake type H. In these tables, the median masses are considered to better represent the shift in the central tendency of fuel and take-off mass values, as the mean can be very sensitive to outliers.

Table 5.2: Variation in Initial Fuel and Takeoff Mass with Altitude Offset (Wake Type M)

Altitude Offset (ft)	**Median Fuel Mass [kg]** (Variation)	**Median Takeoff Mass [kg] (Variation)**
−9000	3974.9 (+0.65%)	63307 (+0.03%)
−7000 (current)	3949.2 (-)	63284 (-)
−5000	4011.3 (1.57%)	63499 (0.34%)
−3000	4313.2 (9.21%)	64244 (1.52%)

In the case of wake type M, decreasing the altitude offset to -9000 ft does not have much impact on the initial fuel mass, and thus on the take-off mass. However, reducing the altitude offset to -3000 ft, and thus estimating a 4000 ft higher cruise flight altitude, leads to an approximately 10% increase in the initial fuel consumption.

Table 5.3: Variation in Initial Fuel and Takeoff Mass with Altitude Offset (Wake Type H)

Altitude Offset (ft)	**Median Fuel Mass [kg]** (Variation)	**Median Takeoff Mass [kg]** (Variation)
−9000	39189 (−7.83%)	194806 (−0.29%)
−7000 (current)	42519 (-)	195379 (-)
−5000	47333 (11.32%)	198472 (1.58%)
−3000	58595 (37.81%)	206034 (5.45%)

For Wake Type H, the variation in the initial fuel mass is much greater. Wake type H aircraft tend to be used for long-haul flights, thus the fuel consumption estimate is a lot more dependent on this initial cruise altitude assumption. As can be seen, the initial fuel mass estimate can vary over 37% depending on the altitude estimate, whereas for wake type M it only varies around 9%. The impact this has on the total take-off mass (TOM) is therefore more significant for larger aircraft, often flying longer ranges.

With the initial fuel mass variation determined, the sensitivity of the fuel burn and emissions to the input assumptions can now be assessed. Figure 5.4 displays the sensitivity for wake type M aircraft. In this case, the fuel consumption seems to be more sensitive than the emission indices. Furthermore, only the empty weight factor has a variation larger than ±2%. An increase in the rate of climb by over 20% can also lead to an increase in fuel consumption of over 2%, whereas a reduction in ROC threshold does not lead to a significant change.

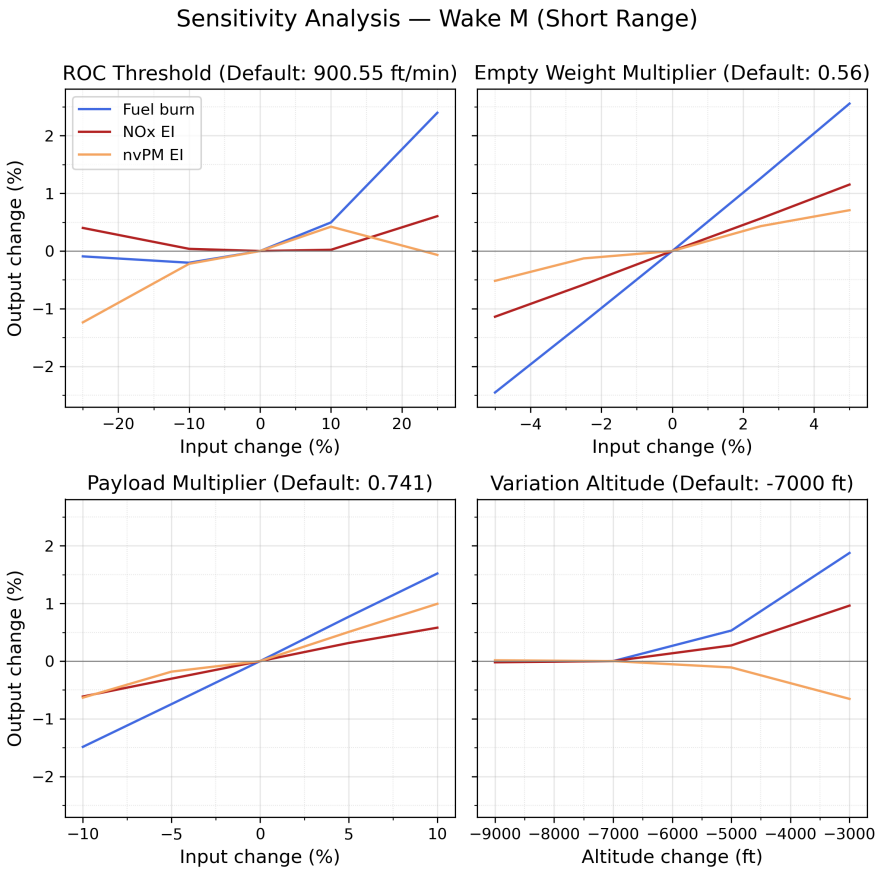

Figure 5.4: Sensitivity analysis outcome for aircraft of wake type M (or short range for Payload Multiplier).

The sensitivity of altitude distribution to ROC threshold variations is illustrated in Figure 5.5. This shows that decreasing the ROC threshold shifts the flight profile slightly to higher altitudes. However, increasing the rate of climb threshold leads to a large set of flights cruising below 30000 ft. This is highly irregular and is not seen in the data of Teoh et al. [60] in blue.

In the case of wake type H, shown in Figure 5.6, the sensitivity of the output to the empty weight factor and payload factor is pretty low. The ROC threshold and initial fuel mass, on the other hand, lead to larger variations than for wake type M aircraft. This likely reflects the longer cruise distance of these flights and the larger fraction of aircraft mass attributed to fuel mass.

The sensitivity of the altitude distribution to ROC threshold for wake type H is illustrated in Figure 5.7. Similarly to wake type M aircraft, an increase in ROC threshold leads to a shift in altitude distribution to lower altitudes, and the opposite is true for a decrease in ROC threshold. Another display of the increased impact of initial fuel mass on heavier aircraft compared to medium aircraft is the altitude distribution shown in Figure 5.8. In these figures, it is clear that the increased impact of the initial cruise estimate on the fuel mass leads to an increased variation in the altitude distribution.

Additionally, relative to the altitude distribution from Teoh et al.'s inventory, the wake-type H altitude

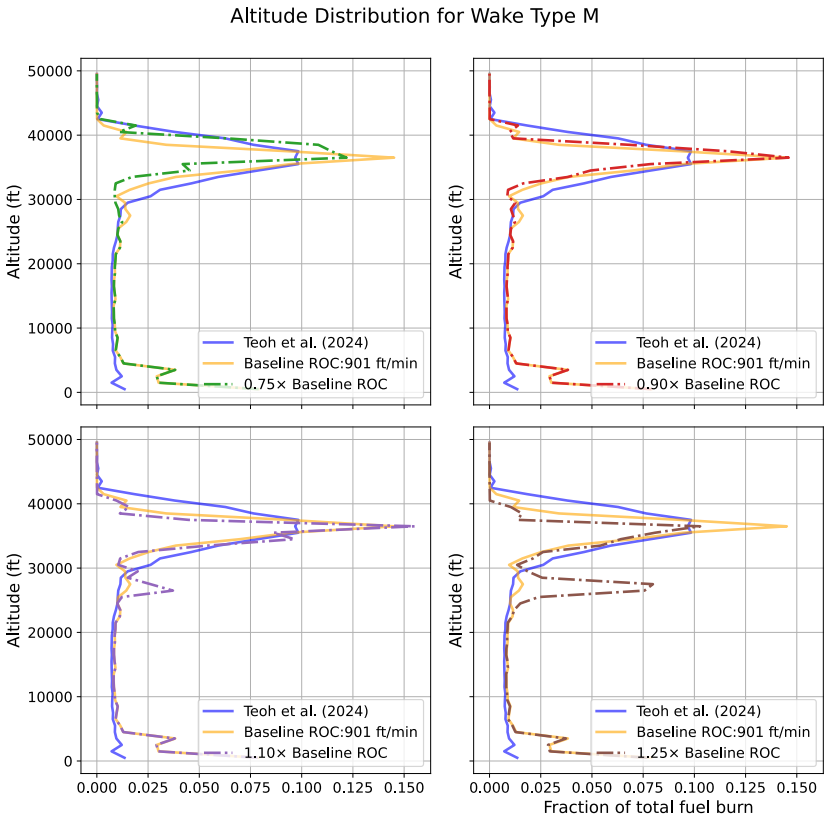

Figure 5.5: Altitude distribution variation with ROC threshold for wake type M aircraft.

distributions show multiple spikes (Figure 5.7); these are less prominent for wake-type M aircraft (Figure 5.5). This stems from using a single ROC threshold value as the measure of cruise altitude for all flights of a given wake type. Because the ROC value is a mean, it will over- and under-estimate the actual altitude for many flights, with the largest deviations for flights that are very long or very short compared with the wake-type mean stage length. Given that wake-type M aircraft generally fly shorter distances, this impact is less prominent.

Now that the sensitivity of the results to each input parameter has been visualised, the reason for these shifts can be analysed to get a better understanding of the model. Firstly, the increase in fuel burn for wake type M aircraft is a combination of an increase in take-off mass, and less time in climb, so a higher cruise mass. The NO_x EI increases with increased fuel flow in cruise due to the higher mass. The nvPM number EI, as mentioned previously and shown in Figure 5.3, greatly depends on the specific engine used.

For wake type H, the largest sensitivity is found in nvPM number EI for the ROC threshold. This is likely due to the nature of the MEEM method, which is independent of the fuel consumption in BADA, and determines a thrust setting for each altitude and Mach number. Given the large distances travelled by wake type H aircraft, this leads to a much more significant variation than the one seen for wake type M. However, in both cases, it seems that it tends to decrease with altitude. Furthermore, the wake type H aircraft flying at higher altitudes tends to increase fuel consumption and NO_x emissions. Similarly to wake type M, increasing TOM leads to an increase in both fuel consumption and NO_x in cruise.

Finally, referring to Figure 5.8, it can be seen that increasing the initial cruise altitude assumption, which increases the initial fuel mass (based on Tables 5.2 and 5.3), leads to an increase in the share of fuel burn at lower altitudes. This is due to the increase in TOM due to the increased initial fuel mass. This highlights a limitation of the method. Indeed, the higher initial cruise altitude assumption leads to a lower cruise altitude in the trajectory analysis. This means the initial fuel mass is likely overestimated. Further improvements to the model could implement an iterative process for initial fuel mass determination.

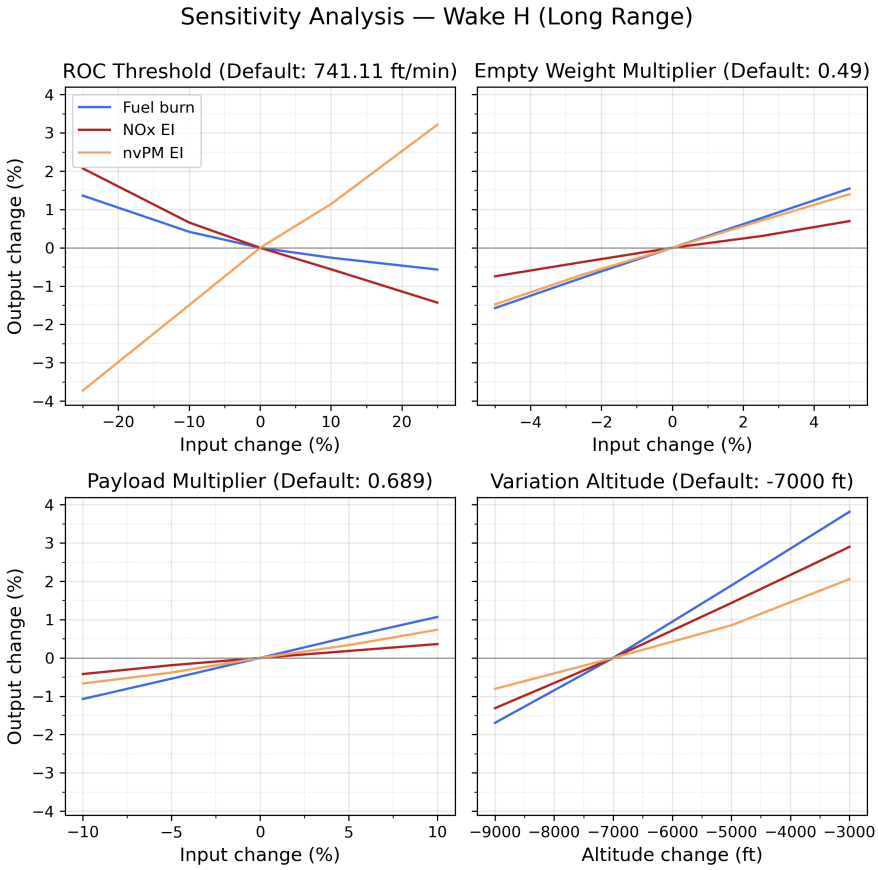

Figure 5.6: Sensitivity analysis outcome for aircraft of wake type H (or long range for Payload Multiplier).

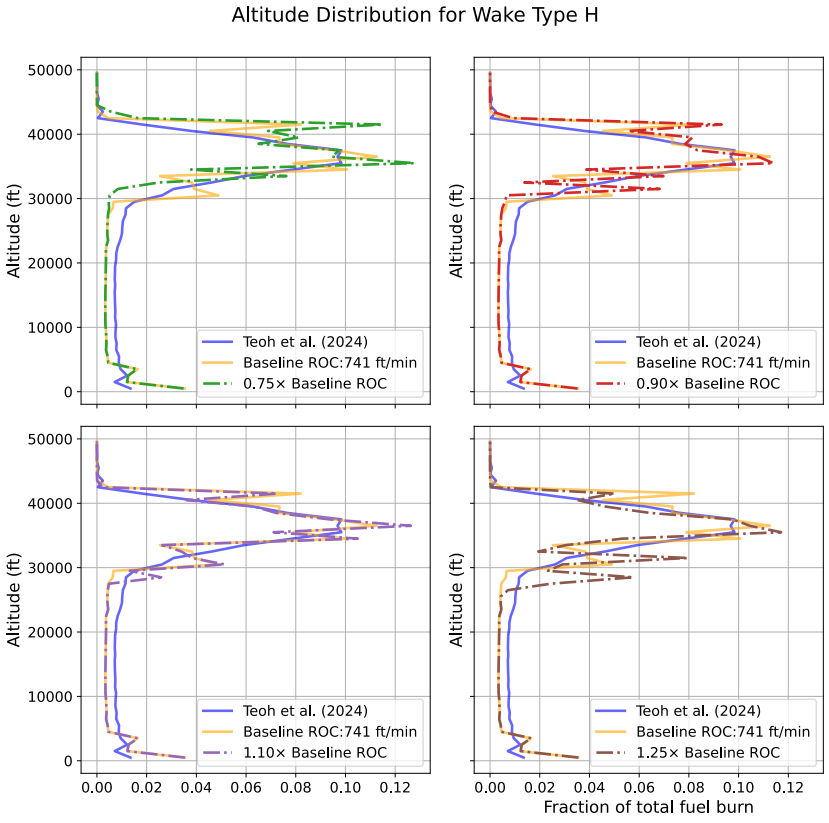

Figure 5.7: Altitude distribution variation with ROC threshold for wake type H aircraft.

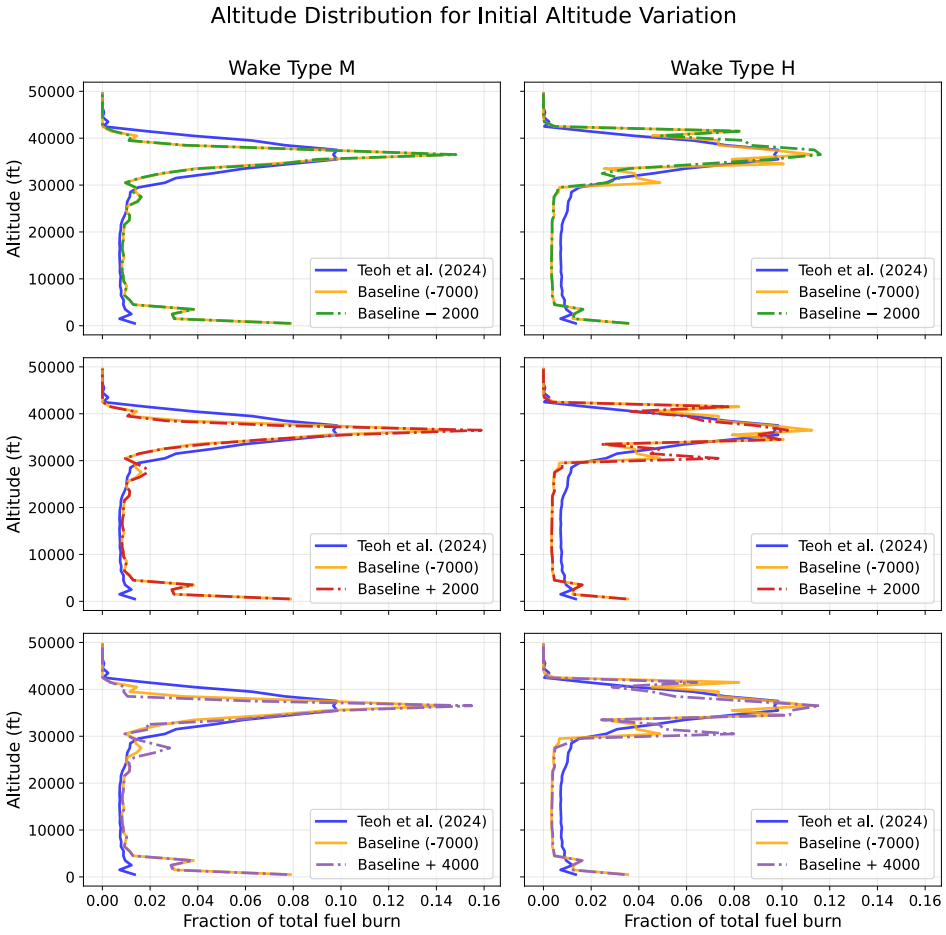

Figure 5.8: Sensitivity of altitude distribution to variation in initial altitude estimate for wake type M (left) and wake type H (right).

5.4. Summary

To summarise the analysis performed in the previous section and gather the main takeaways:

- **Wake type M :**
  - Lower variation in general. The main elements of sensitivity are the fuel burn due to OEM and ROC threshold.
  - Climb phase is more prevalent, and the impact on cruise may balance out a bit more due to this.
- **Wake type H :**
  - The cruise phase is much more prevalent. The effect on emissions is more pronounced.
  - Initial fuel mass and ROC threshold are the parameters which the results are most sensitive to.

This highlights the importance of the ROC threshold parameter. This parameter directly impacts the flight altitude, to which fuel burn and emissions are sensitive to. The current sensitivity analysis is based on the baseline ROC threshold investigated prior to this study at the TU Delft, based on wake type. This exemplifies the reason for assessing ROC thresholds based on range category instead of wake type.

Furthermore, as mentioned previously, this shows the importance of an accurate initial fuel mass estimate and serves as a base for future studies on the matter.

6

Uncertainty Analysis

This chapter presents the uncertainty in the results of the emission inventory due to the uncertainties associated with individual input parameters and model outputs. Because many inputs are represented by sample means, while their true values vary across the sample data ranges, each key parameter is modelled with an appropriate probability distribution, and its uncertainty is propagated through the inventory via Monte Carlo simulations. This results in a distribution of plausible estimates for each emission species. Each distribution can be summarised with a confidence interval, representing the range within which the true value of the emission species is expected to lie with the stated probability.

6.1. Uncertainty Distributions

This section presents the uncertainty distributions that will be used in the Monte Carlo simulations.

6.1.1. Uncertainty of Inventory Updates

The improvements made to the emission inventory in this work come with a new set of uncertainties associated with them.

Engine Assignment

As mentioned in section 4.6, the engine selection method used in the emission inventory does not always contain a matching engine for the provided registration. Furthermore, in some cases, a broad name is used for the engine in registries, which may cover numerous variants. To assess the uncertainty related to the engine selection, the selected engine for each flight is modelled as a discrete random variable whose probabilities are given by the EASA market-share data for each airframe. The procedure can be described as follows:

1. For the specific aircraft assigned to the analysed route, the EASA market share will have a set of engines. Let
$$E \in \{\text{engine}_1,\ \text{engine}_2,\ \ldots,\ \text{engine}_m\}$$
denote the engine used by this specific aircraft on the given route.
2. Then if the reported shares are s_i for engine engine_i, the probability mass function
$$P\big(E = \text{engine}_i\big) \;=\; s_i, \qquad \sum_{i=1}^{m} s_i = 1.$$
can be defined.
3. Finally, in each Monte Carlo trial, a uniform variate $u \sim U(0,1)$ is drawn and engine_i is selected according to the cumulative shares.

This procedure ensures that, across many simulations, each engine model is chosen in proportion to its observed market share.

For example, taking a hypothetical aircraft $aircraft_h$ with marketshare $s_{\text{CFM}} = 0.6$ and $s_{\text{IAE}} = 0.4$, then:

$$\text{engine}_{aircraft_h} = \begin{cases} \text{CFM56} & \text{if } 0 < u < 0.6 \\ \text{IAE} & \text{if } 0.6 \leq u < 1 \end{cases}$$

meaning roughly 60% of flights will be assigned the CFM, and 40% IAE. By propagating this discrete uncertainty through our performance and emission models, the uncertainty in fuel consumption and emissions due to the engine selection can be quantified.

Lateral Inefficiency

The lateral inefficiency multipliers are derived from the extensive dataset compiled by Teoh et al. [60], as mentioned in section 4.2. This leads to a large sample size in the data available, even after accounting for the split based on range. Given this large sample size, a non-parametric Gaussian Kernel Density Estimate (KDE) was fitted to the data rather than imposing a Normal distribution. The KDE is defined by

$$\hat{f}(x) = \frac{1}{n\,h} \sum_{i=1}^{n} K\Big(\frac{x - x_i}{h}\Big), \tag{6.1}$$

where K is the standard normal kernel, n is the sample size, and the bandwidth h follows Scott's rule, $h = n^{-1/5}$ for 1-dimensional data.

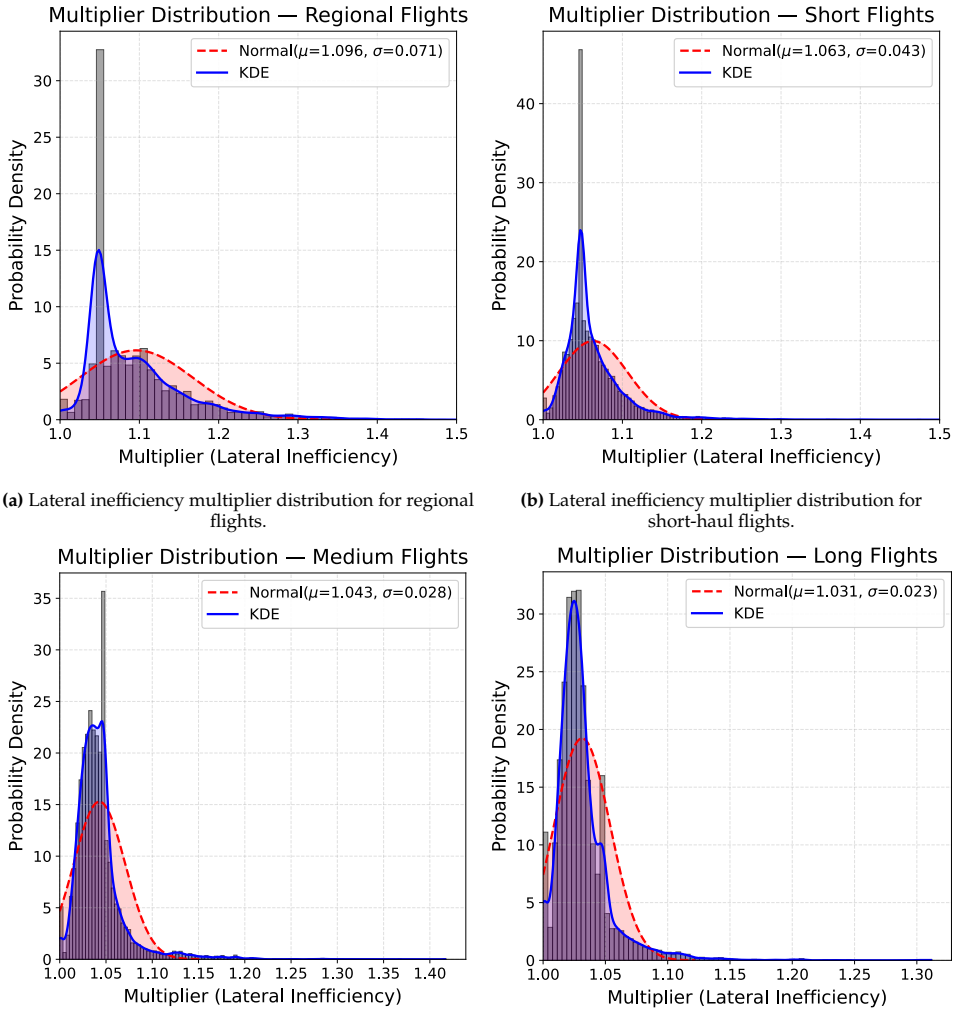

(a) Lateral inefficiency multiplier distribution for regional flights.

(b) Lateral inefficiency multiplier distribution for short-haul flights.

(c) Lateral inefficiency multiplier distribution for medium-haul flights.

(d) Lateral inefficiency multiplier distribution for long-haul flights.

Figure 6.1: Lateral inefficiency multiplier distributions overlaid with normal distribution and KDE.

As shown in Figure 6.1, the resulting density (solid line) accurately captures both the sharp peak near unity and the extended tail of the data from Teoh et al. [60], outperforming a simple Normal approximation (dashed red line).

Given that a Gaussian KDE is essentially a weighted sum of multiple normal distributions with variation h^2 around each sample, at each Monte Carlo iteration, one of the n observed lateral-inefficiency values (x_i) is uniformly selected at random. A perturbation is added to this sample based on a normal distribution ($\varepsilon \sim \mathcal{N}(0, h^2)$), and added to the selected lateral inefficiency, $x^* = x_i + \varepsilon$. This is the method by which Python yields samples following the KDE defined by Equation 6.1.

ROC Threshold

The uncertainty in the ROC threshold is characterised by fitting three candidate PDFs, a Normal, Skew-Normal and Triangular distribution, to the empirical ROC data for each flight range (regional, short, medium, long). These are shown in Figure 6.2, illustrating the histogram of observed ROC values overlaid with the three fitted curves.

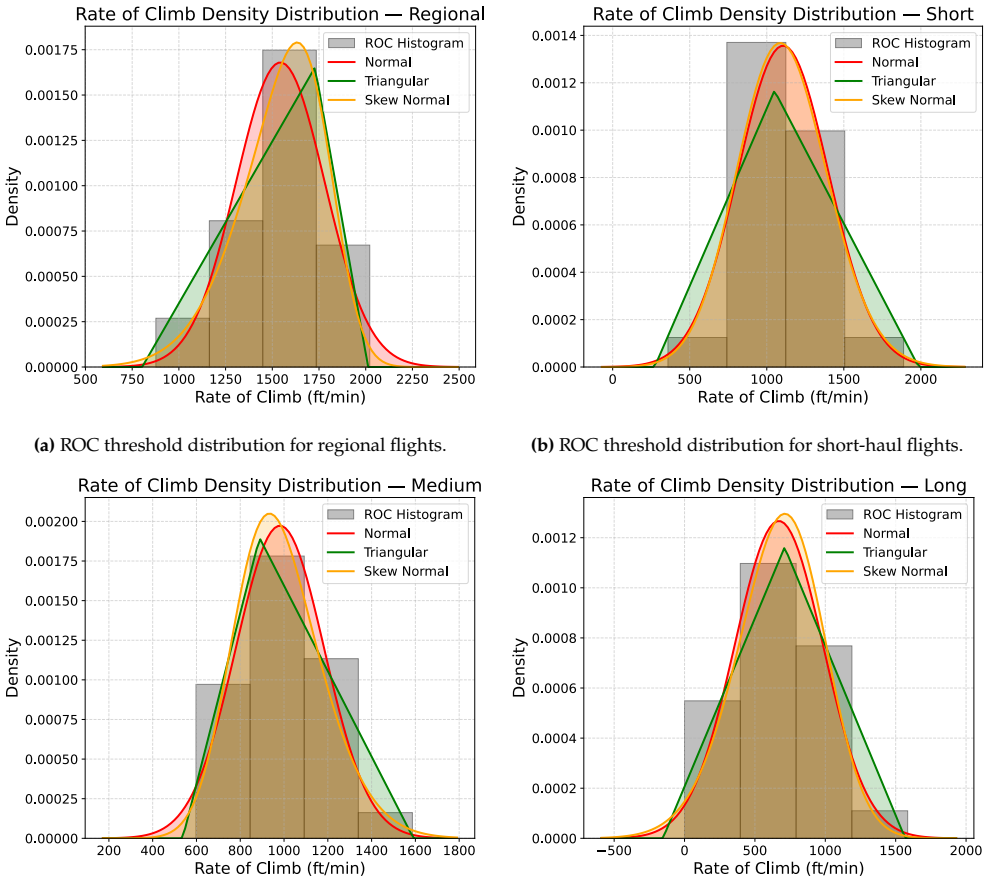

(a) ROC threshold distribution for regional flights.

(b) ROC threshold distribution for short-haul flights.

(c) ROC threshold distribution for medium-haul flights.

(d) ROC threshold distribution for long-haul flights.

Figure 6.2: ROC threshold distributions overlaid with PDFs (Normal, Skew-Normal, triangular).

The goodness of each fit with respect to the data was assessed via the Anderson–Darling test, explained in section 4.6. Table 6.1 lists the p-values, and Table 6.2 gives the corresponding A^2 statistics. A distribution was considered acceptable if $p \geq 0.05$, and among those, the one with the smallest A^2 was chosen.

Table 6.1: p-values from Anderson–Darling test for ROC threshold fits

Distribution	Regional	Short	Medium	Long
Skew-Normal	0.944	0.305	0.917	0.154
Normal	0.770	0.288	0.825	*0.002*
Triangular	0.515	0.515	0.620	0.237

For regional flights, all distributions are deemed acceptable considering the p-value. Examining the AD statistic, the Skew-Normal distribution yields the best fit ($A^2 = 0.153 < 0.241 < 0.472$) and is therefore adopted. The same holds for both short- and medium-haul flights. Finally, for long-haul, the Normal distribution is rejected, and the Skew-Normal is selected for the same reasons.

Table 6.2: A^2 statistics from Anderson–Darling test for ROC threshold fits

Distribution	Regional	Short	Medium	Long
Skew-Normal	0.153	0.394	0.160	1.107
Normal	0.241	0.432	0.218	–
Triangular	0.472	0.875	0.425	1.450

Operating Empty Mass Factor

The sample of OEM fractions was first tested with both Skew–Normal and Normal fits, but the Skew–Normal proved unreliable given the limited number of observations and absence of a clear mode (Figure 6.3). Anderson–Darling tests on the Normal distributions yield p=0.736, 0.661 and 0.528 for light, medium and heavy wake types, respectively. These are well above the $p = 0.05$ threshold, indicating no significant deviation from normality.

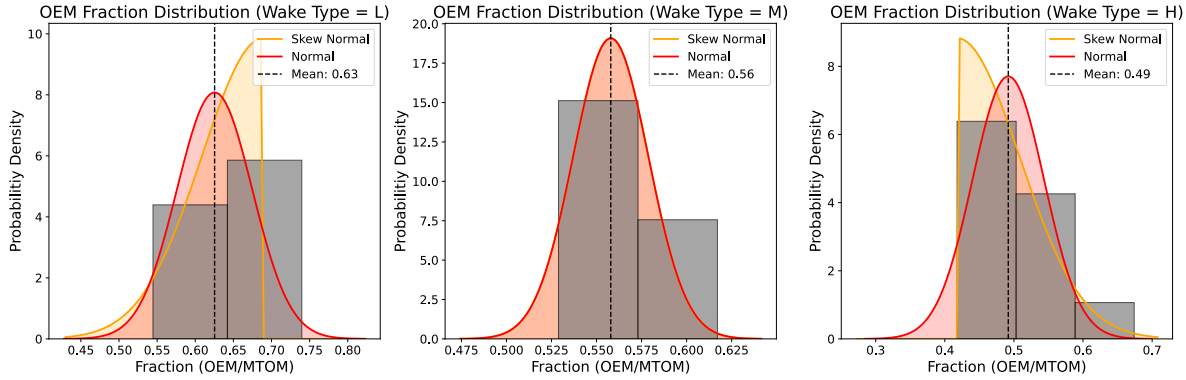

Figure 6.3: Histograms of OEM fractions with fitted Normal (red) and attempted Skew–Normal (orange) PDFs.

BADA4 Performance Model

A source of uncertainty for the model fuel consumption stems from the BADA4 performance model errors. Data on these errors is available for each aircraft, under different conditions and flight phases. The underlying distribution shape is unspecified, however. Thus, the error is modelled as a zero-mean Normal distribution with standard deviation equal to the RMSE of the BADA4 errors:

$$\varepsilon_{\text{fuel}} \sim \mathcal{N}\left(0,\ \text{RMSE}^2\right).$$

The error terms for climb, cruise and descent phases for each aircraft type, thus three distributions per aircraft.

In the Monte Carlo simulations, a random normalised error term is retrieved from a standard normal distribution ($\varepsilon^* \sim \mathcal{N}(0,1)$), and multiplied by the RMSE to get the error term for the simulation.

nvPM Emission Model

A source of uncertainty for the nvPM emission estimate lies in the method applied. The MEEM methodology is validated by the authors on a medium engine and a large engine using the P3T3 method, with proprietary manufacturer data [3]. These are shown in Figure 6.4. In each panel:

- The solid red line is the 1:1 line (perfect agreement).
- The dashed red lines mark a ±20 % error band.
- Blue markers are climb and descent points, green markers are cruise points.

Both Normal and Skew-Normal PDFs were fitted to each distribution. Similarly to the ROC threshold, the goodness-of-fit was assessed via the Anderson–Darling test. The resulting p-values are given in

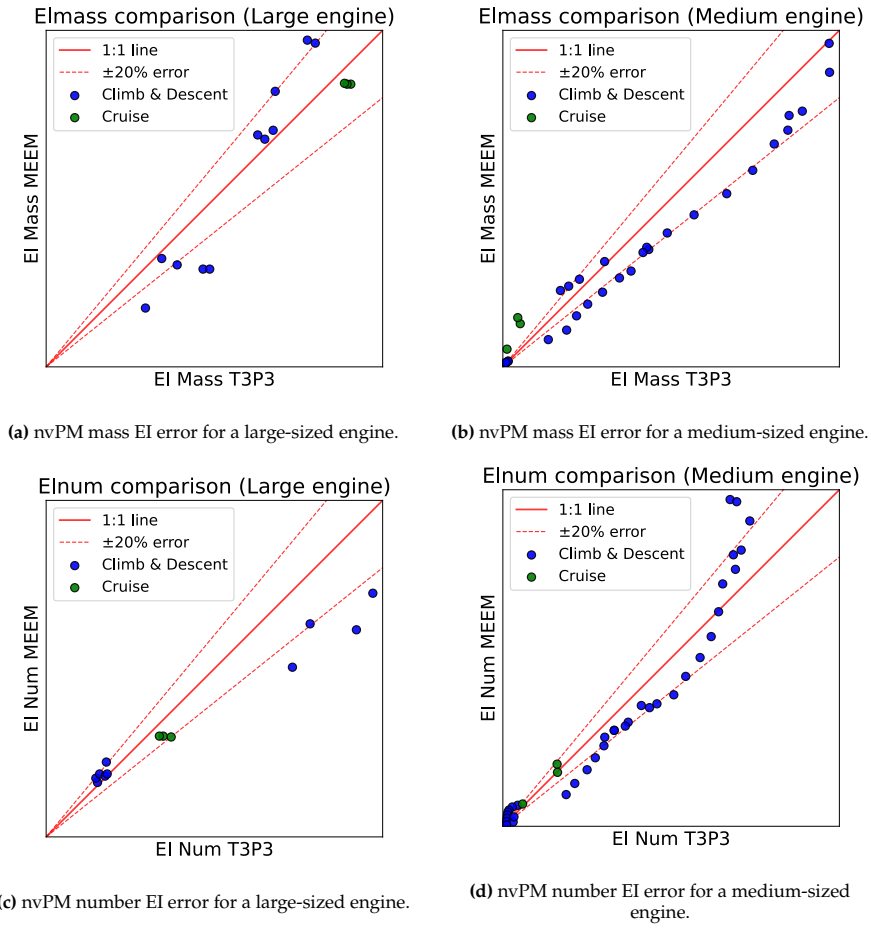

(a) nvPM mass EI error for a large-sized engine.

(b) nvPM mass EI error for a medium-sized engine.

(c) nvPM number EI error for a large-sized engine.

(d) nvPM number EI error for a medium-sized engine.

Figure 6.4: Comparison of MEEM vs. P3T3 EI values for nvPM mass and number, classified by engine size and flight phase [3].

Table 6.3. From there it is clear that all Skew-Normal PDFs are rejected, except for nvPM mass in climb and descent phase, where the normal distribution is rejected.

Table 6.3: Anderson–Darling p-values for fitted EI error distributions.

Distribution	Mass (Climb/Descent)	Mass (Cruise)	Number (Climb/Descent)	Number (Cruise)
Skew-Normal	0.295	0.000	–	0.000
Normal	0.033	0.155	0.222	0.474

A limitation of this data is that there are only six points for cruise per distribution emission type. These are too few, and other validation data should be considered to more accurately estimate the uncertainty due to the MEEM method.

6.1.2. Uncertainty of Base Inventory

Certain aspects of base inventory remain unchanged. These aspects must still be incorporated into the uncertainty analysis of the updated inventory to fully represent the extent of the results. These are based on the work of Rik Kroon [30].

Payload Factor

The first element is the payload factor. This represents the fraction of the maximum payload weight an aircraft uses for a flight. As mentioned in section 4.5, the parameter is set at 0.741 for short-haul and 0.689 for long-haul flights. The uncertainty associated with each of these parameters is represented by a triangular distribution for short-haul and a normal distribution for long-haul. The exact parameters are provided in Table 6.4.

Engine Ageing
Another aspect considered in the work of Rik Kroon is engine ageing. This considers the fact that certain engine components degrade over time as the engine is used. From literature, the associated degradation of each parameter is estimated and represented with a distribution. Monte Carlo simulations are performed using these degradation factors to get a distribution for the TSFC multiplier for a set of engines. These result in a normal distribution as described in Table 6.4 [30].

BADA3 Fuel Consumption
In the updated inventory, there are cases where the aircraft for a specific flight is not covered by BADA4. This occurs for 11% of the total flown distance, which is still a significant portion. Therefore, the uncertainty associated with the BADA3 model must be incorporated. Unlike BADA4, which includes RMSE values associated with their fuel consumption, BADA3 does not include such information. Fortunately, extensive research on the uncertainty propagation of various elements impacting the fuel consumption was carried out by the FAA [18]. These are carried out for various aircraft types (large single aisle and small twin aisle aircraft) on two sample route lengths.

Following the uncertainty propagation, uncertainty distributions for the aircraft types and route length combinations are determined. These are simply distributions over the total fuel consumption, and Rik Kroon converts these into a single fuel flow multiplier distribution to be used in the emission inventory. This multiplier is represented by a triangular distribution described in Table 6.4

BFFM2 Emission Indices
Similarly to the nvPM emission indices in the MEEM methodology, the authors of the BFFM2 validate their method against the P3T3 method for a variety of engines [15]. The spread of the error compared to the validation data is shown in Figure 6.5.

Based on the analysis by Dubois et al. [15], Rik Kroon determines three triangular distributions, one for each emission species, with parameters listed in Table 6.4.

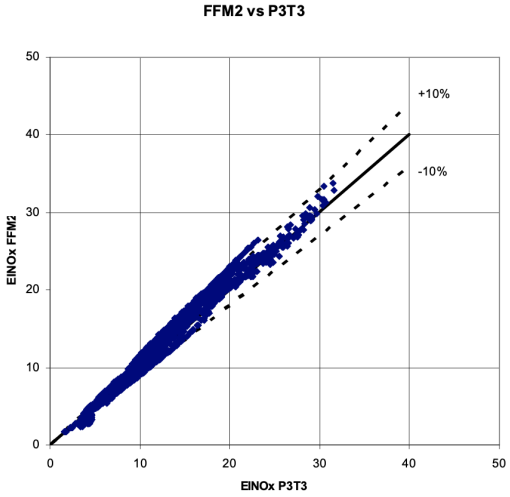

(a) EI NO_x from BFFM2 vs P3T3

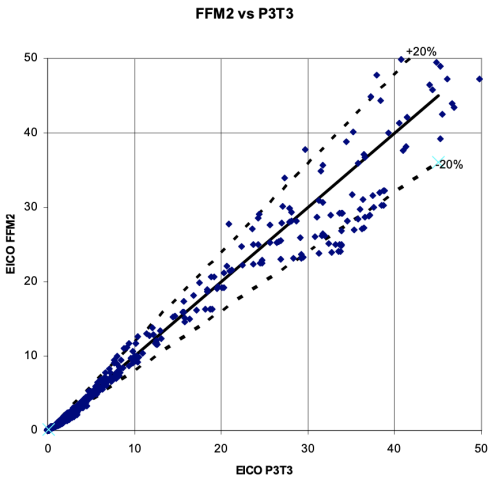

(b) EI CO from BFFM2 vs P3T3

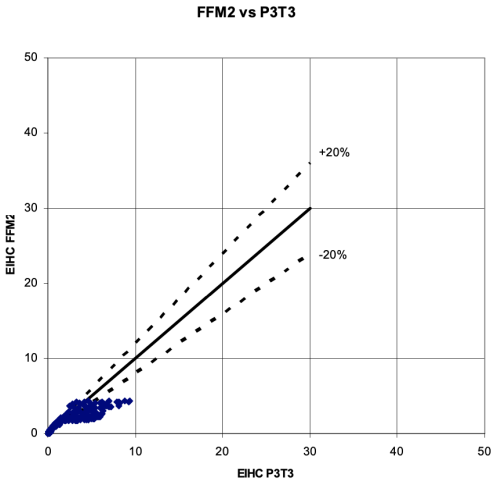

(c) EI HC from BFFM2 vs P3T3

Figure 6.5: Comparison of BFFM2 vs. P3T3 EI values for NO_x, CO and HC [15].

6.1.3. Summary of Parametric Distributions

A summary of all parametric distributions is provided in Table 6.4.

Table 6.4: Summary of all uncertainty distributions used in the Monte Carlo analysis

Source of Uncertainty	Category / Phase	Distribution	Parameters	Source
NO_x EI multiplier	All phases	Triangular	(0.9, 1.0, 1.1)	Rik Kroon [30]
CO EI multiplier	All phases	Triangular	(0.8, 1.0, 1.2)	Rik Kroon [30]
HC EI multiplier	All phases	Triangular	(0.9, 1.0, 1.8)	Rik Kroon [30]
nvPM mass EI error	Climb/Descent	Skew-Normal	(4.29, -0.4, 0.4)	This Work
	Cruise	Normal	(1.15, 1.32)	This Work
nvPM number EI error	Climb/Descent	Normal	(-0.08, 0.26)	This Work
	Cruise	Normal	(-0.03, 0.13)	This Work
BADA4 fuel flow error	All phases	Normal	(0, RMSE)	This Work
BADA3 fuel flow multiplier	All phases	Triangular	(0.92, 0.98, 1.2)	Rik Kroon [30]
Engine aging TSFC multiplier	All phases	Normal	(1.004, 0.006)	Rik Kroon [30]
ROC threshold	Regional	Skew-Normal	(-2.65, 1809.6, 356.3)	This Work
	Short haul	Skew-Normal	(0.97, 911.3, 352.9)	This Work
	Medium haul	Skew-Normal	(1.89, 781.1, 284.6)	This Work
	Long haul	Skew-Normal	(-1.39, 934.9, 411.5)	This Work
Payload fraction	Short haul	Triangular	(0.65; 0.74; 0.83)	Rik Kroon [30]
	Long haul	Normal	(0.69, 0.06)	Rik Kroon [30]
OEM multiplier	Light wake	Normal	(0.63, 0.05)	This Work
	Medium wake	Normal	(0.56, 0.02)	This Work
	Heavy wake	Normal	(0.49, 0.05)	This Work
Lateral inefficiency	Regional	Gaussian KDE	*non-parametric*	This Work
	Short	Gaussian KDE	*non-parametric*	This Work
	Medium	Gaussian KDE	*non-parametric*	This Work
	Long	Gaussian KDE	*non-parametric*	This Work
Engine Selection	All phases	Discrete	*non-parametric*	This Work

6.2. Monte Carlo Simulation Results

A total of 100 Monte Carlo simulations were run on the first 10,000 flights in the database. Each simulation draws random samples for all uncertain inputs, listed in Table 6.4 and propagates them through the performance and emissions models. Some distributions present the values of the parameters themselves; in other cases, they are multipliers applied to the output of a model (performance or emission model). When the distribution is in the form of errors, the error (ε) is turned into a multiplier ($f = 1 + \varepsilon$). Additionally, the non-parametric uncertainty, namely the engine selection uncertainty and the lateral inefficiency, is also included in the uncertainty.

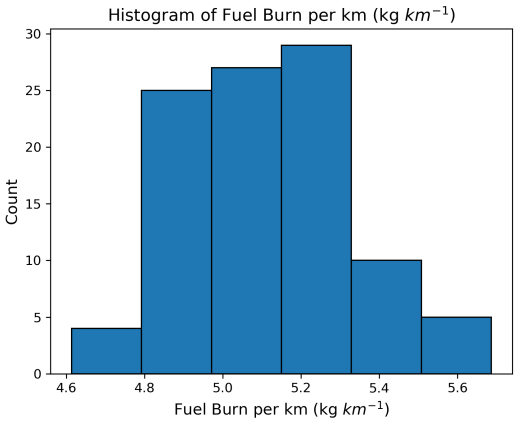

Figure 6.6: Histogram of simulated fuel burn per kilometre (kg km^{-1}).

The outputs of the Monte Carlo simulations are distributions of the target parameters. Figure 6.6 and Figure 6.7 present histograms of the simulated fuel burn per kilometre and emission indices, respectively. They directly provide insight into the range of possible fuel consumption and emission indices for each species, as well as the likelihood for each quantity.

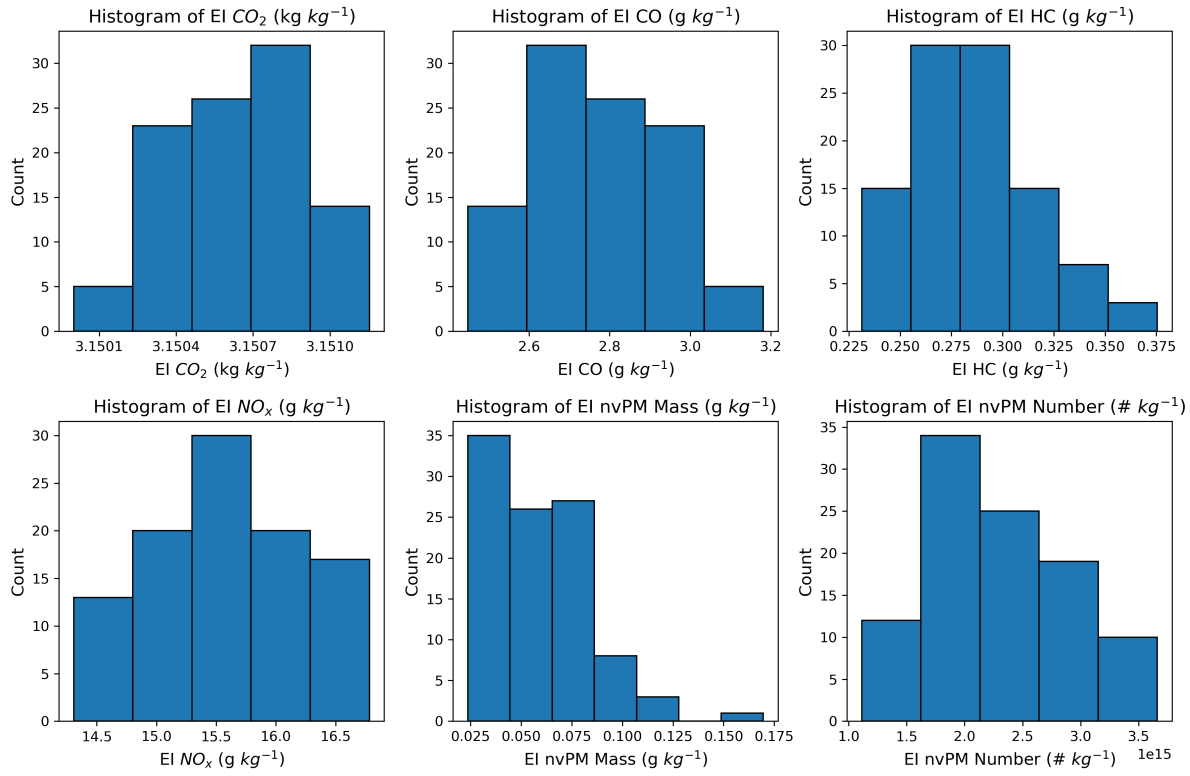

Figure 6.7: Histogram of simulated EI for various species of emissions. The vertical line denotes the baseline value.

Given that each Monte Carlo simulation analyses the first 10,000 aircraft-route pairs, it only analyses a subset of the total flight data. Thus, to scale the uncertainty to the entire inventory, a multiplier

distribution is considered. This is determined by dividing the output of each Monte Carlo iteration by the baseline result for the same 10,000 flights. Because emissions can span different orders of magnitude depending on the species, this also provides a consistent measure for the spread across the different emission species. Figure 6.8 highlights the uncertainty in terms of these multipliers compared to the baseline for key metrics used to assess the results and compare to literature in the next chapter.

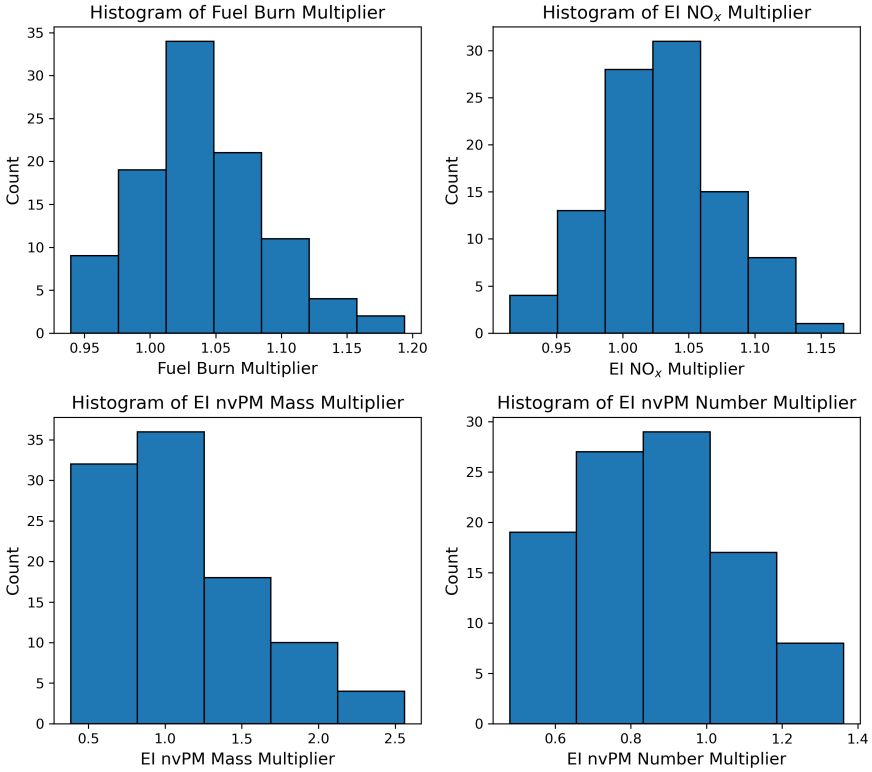

Figure 6.8: Histogram of simulated multipliers for key output values.

From each simulated distribution, empirical 95% confidence intervals are obtained by taking the 2.5th and 97.5th percentiles of the sample. This is applied to the multiplier distributions, allowing it to be applied to the results of the main analysis. Thus, Table 6.5 provides the mean multiplier and associated uncertainty due to the propagation of the uncertainty associated with the input and models of the inventory.

Table 6.5: Monte Carlo results: means and 95% confidence intervals for key multipliers

Metric	Mean	CI Lower	CI Upper	CI Width
Fuel burn per km	1.0189	0.9394	1.1151	0.1757
CO_2 EI	0.9989	0.9987	0.9990	0.0003
CO EI	1.0224	0.9062	1.1403	0.2342
HC EI	1.3229	1.1049	1.6094	0.5045
NO_x EI	1.0077	0.9348	1.0775	0.1427
nvPM mass EI	0.9897	0.4448	1.9239	1.4791
nvPM number EI	0.8861	0.4967	1.3531	0.8564

As Table 6.5 shows, the nvPM mass multiplier exhibits an exceptionally wide 95% confidence interval (CI width ≈ 1.5), reflecting very large variability in the simulated outcomes. The nvPM number multiplier also shows a substantial spread (CI width ≈ 0.85), though less extreme. This large uncertainty is most likely a consequence of the poor distribution due to the limited sample size of the nvPM EI values in cruise. Additionally, given the large variation in nvPM emissions between engine types, the engine model uncertainty may translate to a large spread in the nvPM emissions.

7

Results and Discussion

The results gathered over the course of this thesis project will be presented and discussed in this chapter.

7.1. Final Results and Comparison

The final results are presented in Table 7.1, using fuel burn per kilometre and the emission indices as metrics as it removes the dependency on the total number of flights analysed and distance travelled. These results are also visualised for the fuel burn and the key emissions analysed in this study (NO_x and nvPM) in Figure 7.11. The total emission estimate values can be found in Appendix A, in Table A.1 and in Figure A.1 for the key emissions. The global distribution of NO_x emissions is shown in Figure 7.5. The current model encompasses the updated engine selection method, updated lateral inefficiency multipliers and flight altitude determination, the addition of the BADA4 performance model, and the MEEM method for nvPM emission estimates.

Table 7.1: Final result of updated inventory compared to literature.

Descriptor	Current Work	Rik Kroon [30]	Teoh et al. [60]	Quadros et al. [44]
Fuel burn (Tg)	250	254	283	297
Fuel burn per km (kg km^{-1})	**5.13**	**5.23**	**4.64**	-
EI CO_2 (kg kg^{-1})	3.151	3.151	3.152	3.155
EI CO (g kg^{-1})	2.397	2.403	1.413	2.741
EI HC (g kg^{-1})	0.199	0.200	0.120	0.143
EI NO_x (g kg^{-1})	**15.974**	**17.764**	**15.866**	**15.556**
EI nvPM (g kg^{-1})	0.053	0.020	0.076	0.033
EI nvPM (# kg^{-1})	**2.52E+15**	-	**1.00E+15**	**1.20E+15**

The updated results show notable differences in fuel consumption and emissions when compared to the other 2019 global inventories. These differences stem from the approach used in either the information, performance or emission model in each of the inventories. In this study, the focus is placed on the fuel consumption, NO_x and nvPM emissions. The discrepancies in each of these species between the inventories will be discussed in this section.

To get a better overview of the differences encountered between this study and the literature, Figure 7.1 illustrates the relative difference in fuel consumption per kilometre and key emissions. In terms of fuel burn per kilometre, Figure 7.1 shows that, compared to the updated result of this work, Rik Kroon's inventory has a 2% higher fuel consumption per kilometre, whereas Teoh et al.'s estimate is 9.6% lower. The value from Quadros et al. [44] is not available.

The EI NO_x of both Teoh et al.'s and Quadros et al.'s studies are within 2.5% of the estimated value of this study. On the other hand, Rik Kroon's inventory shows an 11.2% higher EI NO_x compared to the updated inventory.

Figure 7.1 also shows large discrepancies in nvPM emissions for both mass and number between the studies. Regarding the EI nvPM mass, Rik Kroon's inventory shows a much lower estimate, by over 62%, and Quadros et al. by 39%. Yet Teoh et al. estimate a higher EI nvPM mass, 43% larger than the estimate

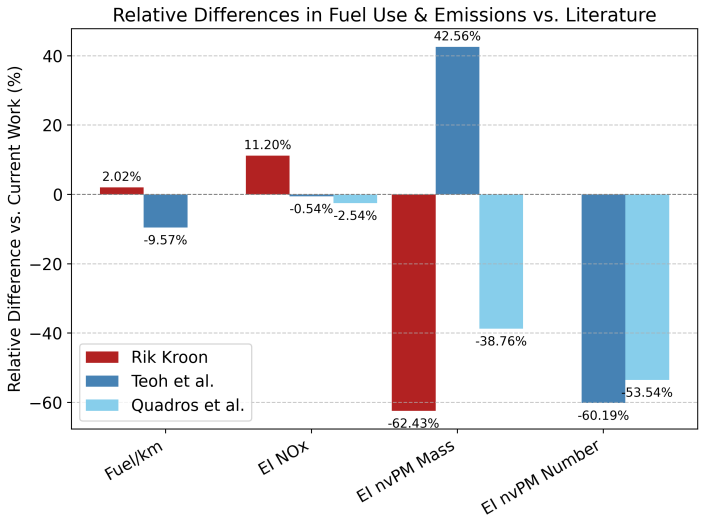

Figure 7.1: Relative difference in fuel consumption and ley emissions between current inventory and literature.

in this study. For nvPM number, Rik Kroon does not have an estimate. In both the works of Teoh et al. and Quadros et al., a significantly lower EI nvPM number is estimated (-60.4% and -53.7% respectively).

To thoroughly assess the climate impact of aviation, it is essential to consider not only total emissions but also their global spatial distribution. First, the altitude distribution of emissions can be considered, which is shown in Figure 7.2. The geographical distribution of emissions is illustrated with Figures 7.5 and 7.6. These are compared with the results of Teoh et al.'s inventory, as they make use of high-resolution ADS-B data.

7.2. Comparison with Teoh et al.

In this section, the differences between the current inventory and that of Teoh et al. are explored further. To begin with, the spatial distribution of emissions is compared, followed by the global emission estimates.

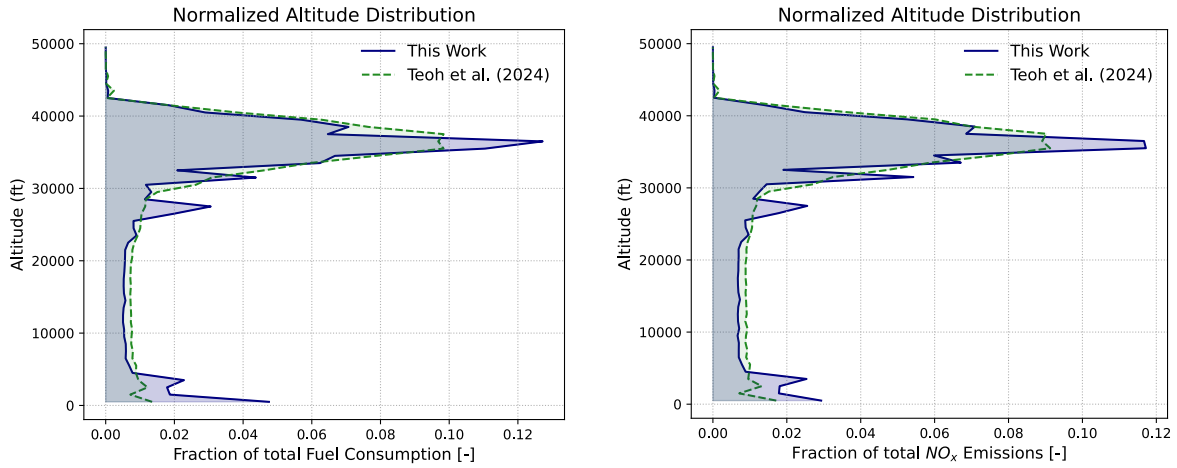

Figure 7.2: Normalised altitude distribution of fuel consumption (left) and NO_x emissions (right) comparing results from this study with those from Teoh et al.

Firstly, by comparing the altitude distribution of fuel consumption, it becomes clear that the ROC thresholds used in this work produce a profile well aligned with theirs. The fuel consumption distribution is a good measure of the flight altitude distribution of the aircraft. In the data from this work, a peak emerges between 25,000 and 30,000 feet, which is not present in the data from Teoh et al.'s inventory. This reflects a limitation of using ROC thresholds for flight altitude determination. Indeed, as the ROC threshold for each range category is a single mean value, it will overestimate the ROC for some flights, leading to lower cruise altitudes. This can be seen when comparing with the observed cruise

altitudes in Figure 7.3. To mitigate this, larger samples are required to reduce the impact of outliers on the mean. Additionally, the range categories can be further refined, and the data within each category can be stratified by wake type.

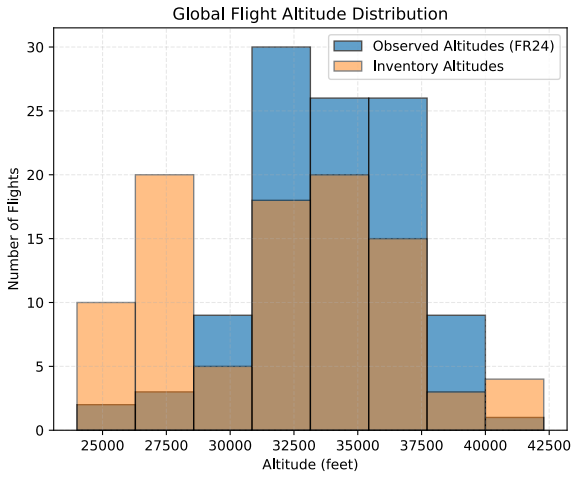

Figure 7.3: Histogram comparing the distribution of the observed cruise altitudes of various flights from FlightRadar24 compared to the cruise altitudes resulting from the mean range-based ROC thresholds.

The altitude distribution of NO_x emissions in Figure 7.2 on the right follows from the fuel consumption distribution. Again, there is good alignment overall, except for a small percentage of outliers. In both the results from this study and those of Teoh et al., the fraction of NO_x emissions is slightly lower than that of fuel consumption at its peak, and slightly higher at lower altitudes. This likely reflects the higher EI NO_x in the climb phase.

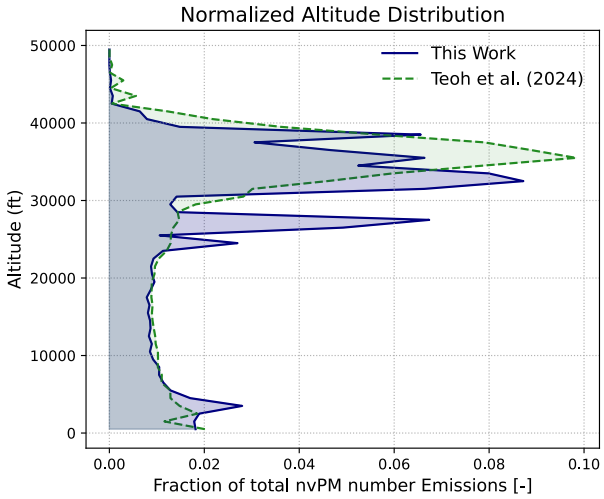

Figure 7.4: Normalised altitude distribution of nvPM number emissions comparing results from this study with those from Teoh et al.

The altitude distribution of nvPM emissions is shown in Figure 7.4. In this case, the distribution differs greatly. From the output of the sensitivity analysis performed in chapter 5, it was found that nvPM emissions can vary greatly with altitude. In the distribution obtained from this work, a substantial share of nvPM emissions occurs at the altitude ranges where the ROC threshold values fail to represent the flight's actual cruise altitude. This leads to a greatly overestimated nvPM emission estimate at lower altitudes.

In terms of the geographical distribution of emissions, the NO_x emission output is illustrated with Figure 7.5. This can be compared to the work of Teoh et al., used as reference [60]. Similar heat maps of emissions can be found in Appendix B for fuel consumption and nvPM emissions.

Although the resolution in the work of Teoh et al. is much higher (Figure 7.5 (bottom)), it can be seen

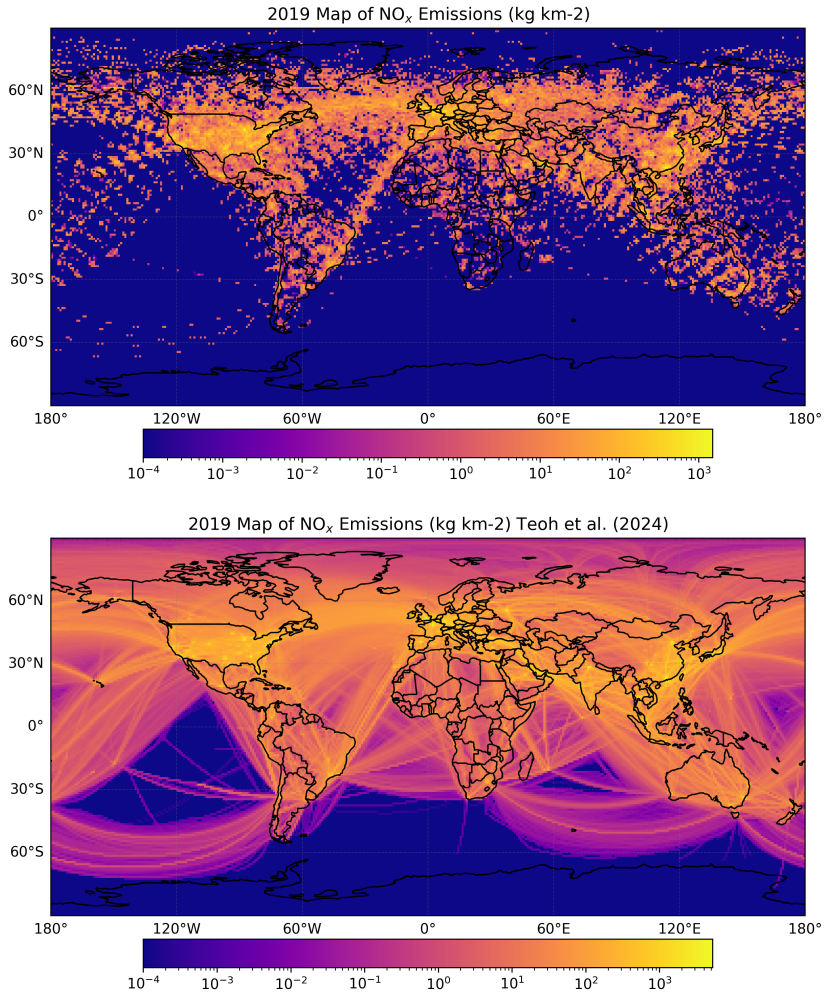

Figure 7.5: Geographical distribution of NO_x emissions estimate from this inventory (top) and the inventory of Teoh et al. (bottom).

that the current inventory (Figure 7.5 (top)) portrays the same major routes. In both maps, it is also possible to see the same major hubs, characterised by the very bright yellow due to the large NO_x emissions concentrated in those areas. However, certain important traffic routes are not covered by the current inventory. Many routes to and from South Africa are missing when compared to the work of Teoh et al., covering flights throughout the whole year. This is a limitation of the representative week, which may not include many flights for those routes, or simply have poor information on them. Thus, emissions are under-represented in the southern hemisphere by the current implementation of the inventory.

Finally, the altitude distribution can be compared across latitude and longitude to assess the concentration of emissions more precisely. Figure 7.6, shown for this work (a) and Teoh et al. (b), again show good agreement. There is a concentration of NO_x emissions at cruise altitude in the Northern Hemisphere, and a larger share of ground emissions in the Northern Hemisphere as well. This is expected, as a majority of air traffic occurs in the Northern Hemisphere, which includes the majority of large economies. The difference in the fraction of emissions is shown in Figure 7.6c and broadly mirrors the peaks seen in Figure 7.2. The largest discrepancies are seen in the Northern Hemisphere, reflecting the concentration of flights and associated NO_x there. In the Southern Hemisphere, where traffic density is lower, the differences are also smaller. However, it is still clear that the fraction of global NO_x is underestimated there relative to Teoh et al.'s work, as established by Figure 7.5. A final difference in the altitude distribution is the larger near-ground share of NO_x emissions in this work. This stems from the different scopes of each study: Teoh et al. [60] exclude LTO emissions from their analysis, whereas these are included in this work, which increases the low-altitude contribution in the normalized distribution.

Following the analysis of the geographical distribution of emissions, the comparison now focuses on differences in their magnitudes. Firstly, Teoh et al. [60] don't consider LTO emissions in their analysis,

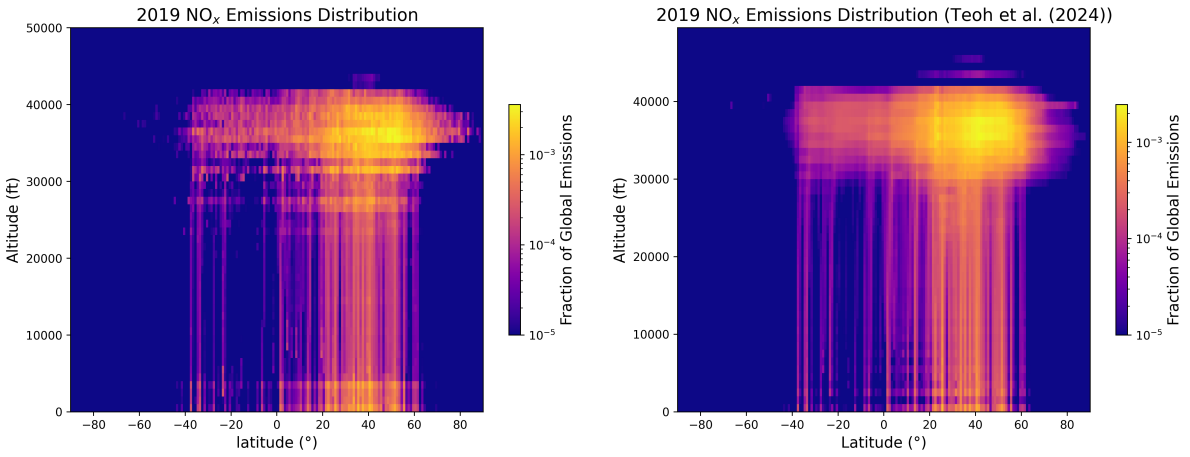

(a) Altitude distribution of NO_x emissions from this study.

(b) Altitude distribution of NO_x emissions from Teoh et al.

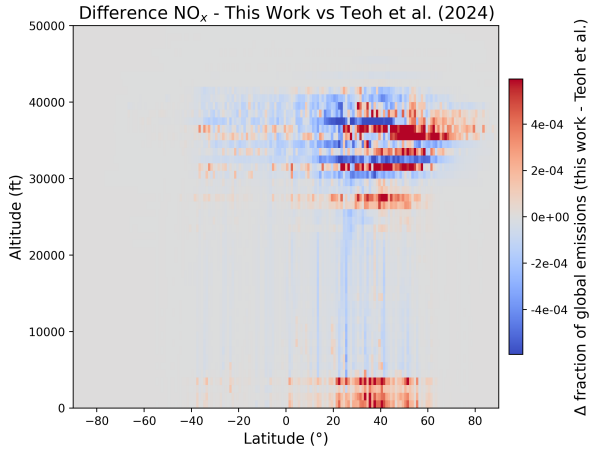

(c) Difference in the altitude distribution of NO_x emissions across latitude.

Figure 7.6: Comparison of altitude distribution of NO_x emissions across latitude between this study and Teoh et al. [60].

as mentioned previously. LTO emissions can account for almost 9% of total fuel consumption in the year 2019, according to Quadros et al. [43]. This may lead to a large reduction in fuel burn per kilometre. Additionally, the nvPM emission estimate is achieved through different methods. As explained in chapter 2, Teoh et al. use their T4T2 method for nvPM mass and number emissions.

To effectively compare the differences between the methodologies, a global fleet analysis is performed, omitting LTO emissions and applying the T4T2 methodology instead of the MEEM. The results relative to those of the main updated inventory (LTO included and MEEM) are presented in Table 7.2. This shows that the fuel burn per kilometre becomes much more comparable. In fact, in this case, the value in this study becomes slightly lower, but this may be due to several aspects: the wind data used in Teoh et al., the difference in engine allocation per route, and the difference in flight altitude.

Table 7.2: Effect of performance and emission model changes on the final results

Descriptor	Current	Current no-LTO	Current no-LTO T4T2	Teoh et al. [60]
Fuel burn (Tg)	250	250	220.47	283
Fuel burn per km (kg km^{-1})	**5.13**	**4.58**	**4.58**	**4.64**
EI CO_2 (kg kg^{-1})	3.151	3.153	3.153	3.152
EI CO (g kg^{-1})	2.397	1.337	1.337	1.413
EI HC (g kg^{-1})	0.199	0.117	0.117	0.120
EI NOx (g kg^{-1})	**15.974**	**16.305**	**16.305**	**15.866**
EI nvPM (g kg^{-1})	0.053	0.053	0.043	0.076
EI nvPM (# kg^{-1})	**2.97E+15**	**2.59E+15**	**7.17E+14**	**1.00E+15**

In terms of nvPM emissions, applying the T4T2 shows a large reduction in the nvPM number EI. Simply

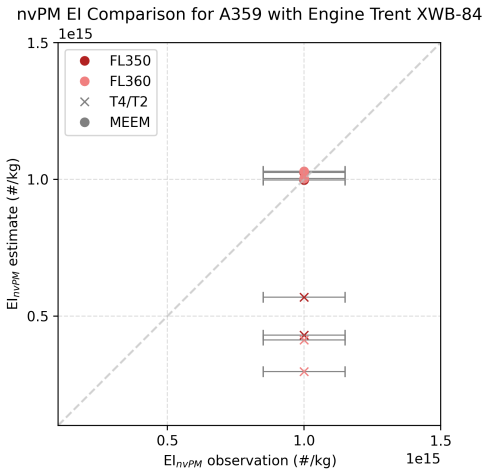

Figure 7.7: MEEM and T4T2 nvPM estimation compared to A359 ECLIF campaign measurements at FL350 and FL360.

removing LTO emissions leads to a slight reduction, however, the order of magnitude remains the same. When applying T4T2 on top, the nvPM number reduces by over 70%, and becomes even lower than Teoh et al.'s estimate (by about 28%). This clearly shows that the major difference between the nvPM number emission estimates is the method.

In the case of the nvPM mass EI, however, the discrepancy grows when applying the T4T2 method. This can be due to numerous reasons. When nvPM measurements are not available in the ICAO databank, in this work, nvPM mass emissions are estimated using the EASA FOA4.0 methodology. As explained in chapter 2, this approach first estimates ground-level nvPM mass based on the Engine Smoke Number (SN), and then applies the Döpelheuer and Lecht (Equation 2.13) [14] scaling factor to adjust the emissions to cruise altitude conditions. In contrast, the method used by Teoh et al. is based on the ImFOX model (Abrahamson et al. [2]). This model estimates nvPM mass by modelling the formation and oxidation rates of soot directly, using engine-specific combustor conditions such as the air–fuel ratio (AFR) and combustor exit temperature (T4). As a result, emissions are calculated explicitly at cruise, without relying on scaling from ground-level values. These methodological differences may contribute to the discrepancies observed in Table 7.2. This also applies to the nvPM number, as when no measurements are available in the ICAO databank, both methods rely on the nvPM mass EI estimate to determine the nvPM number EI. Abrahamson et al. note that the cruise correction applied in SN-based approaches, such as FOA4.0, can underestimate nvPM mass emissions. Abrahamson et al. base their results on measured data from a Douglas DC-8 aircraft equipped with four CFM56-2C turbofan engines [2]. However, as mentioned in chapter 3, the MEEM method, which uses the Döpelheuer and Lecht correction, is validated on a broader set of engines and corresponds well with A359 ECLIF measurement data [10].

Additionally, both the MEEM method and T4T2, as applied in this work, are compared with respect to the A359 ECLIF campaign measurement data. When applying the altitude and Mach number associated with the test data, the estimates presented in Figure 7.7 are found for both methods. This shows that in this case, the MEEM method corresponds more closely to the measurement conditions, and the T4T2 slightly underestimates the measurement data. It should be noted that the raw data were not made publicly available over the duration of this research; thus, the observation values were taken around a mean determined visually, and error bars are included to account for the spread.

Finally, it should be noted that there remain other sources of discrepancies that cannot easily be accounted for. These include:

- The precise flight altitude distribution.
- The incorporation of weather data.
- The specific allocation of engines per flight.
- The inclusion of non-jet aircraft with engines not present in the ICAO EDB (6.4% of total distance flown [60]), assigned constant emission indices.

7.3. Comparison with Rik Kroon and Quadros et al.

In this section, the differences between the current inventory and the baseline inventory for this work (Rik Kroon's inventory) and that of Quadros et al. are discussed.

Firstly, regarding Rik Kroon's inventory, from Figure 7.1, it is clear there is a large difference in NO_x emission index. This is due to the revision of the performance model and the acceleration correction applied in climb. This acceleration correction led to an overestimation of the fuel flow, resulting in unrealistic EI NO_x values during climb. This is illustrated in Figure 7.8a, which shows the method used in the current work, and Figure 7.8b using the acceleration correction.

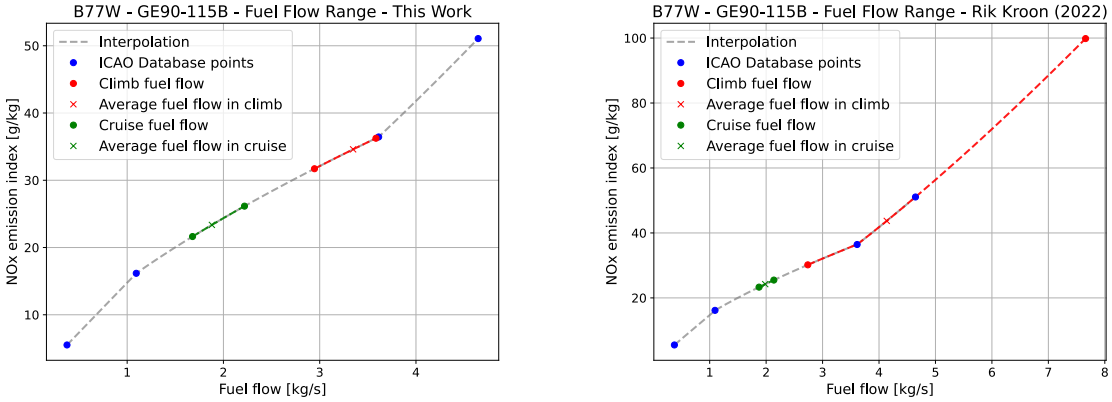

(a) Fuel flow range without acceleration correction.

(b) Fuel flow range with acceleration correction.

Figure 7.8: Comparison of NO_x Emission Index vs. Fuel Flow for B77W - GE90-115B using different methodologies.

Additionally, the altitude distribution of NO_x emissions between this study and the original inventory can be compared, as done in Figure 7.9. This clearly shows a peak in early climb NO_x due to the acceleration correction, which is not present in other emission inventories. Removing the acceleration correction (shown on the right in Figure 7.9 leads to a similar NO_x emission profile in climb, but a skewed cruise distribution. This likely reflects the fact that the ROC threshold was originally set considering the fuel correction.

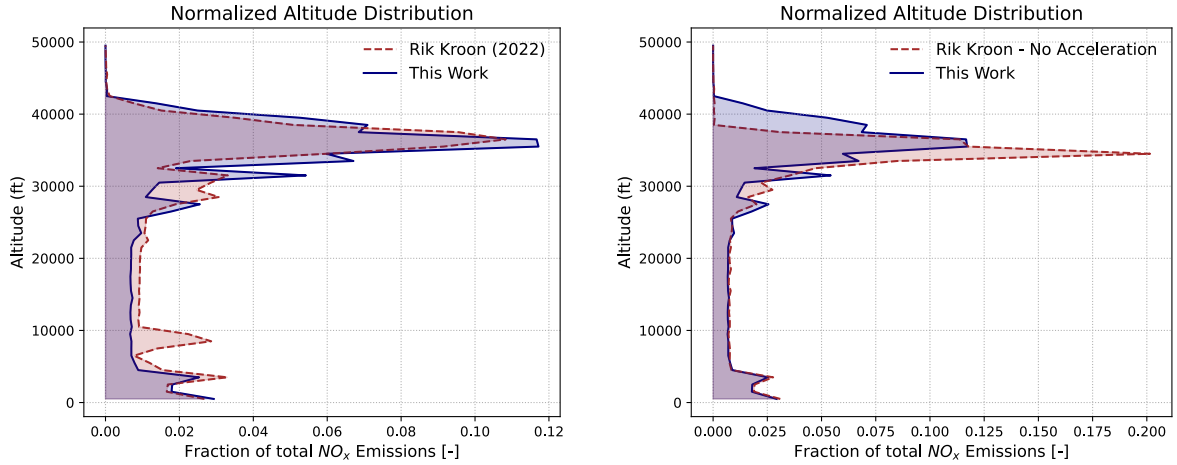

Figure 7.9: Comparison of altitude distributions of NO_x emissions between this study and the original implementation (left), and the updated original study (right).

Finally, regarding the nvPM emissions, large discrepancies are also present. To assess the changes due to methodology, the updated inventory is reverted fully to the BADA3 performance model and the Peck et al. nvPM interpolation method. The FOA4 method is kept to replicate the methodology of Quadros et al. [44]. The outcome is shown in Figure 7.10.

This shows that for nvPM mass emissions, Quadros et al.'s results align well with those of this inventory when the methods are reverted. In terms of nvPM number emissions, the difference reduces but still remains rather large. This is likely due again to a combination of factors:

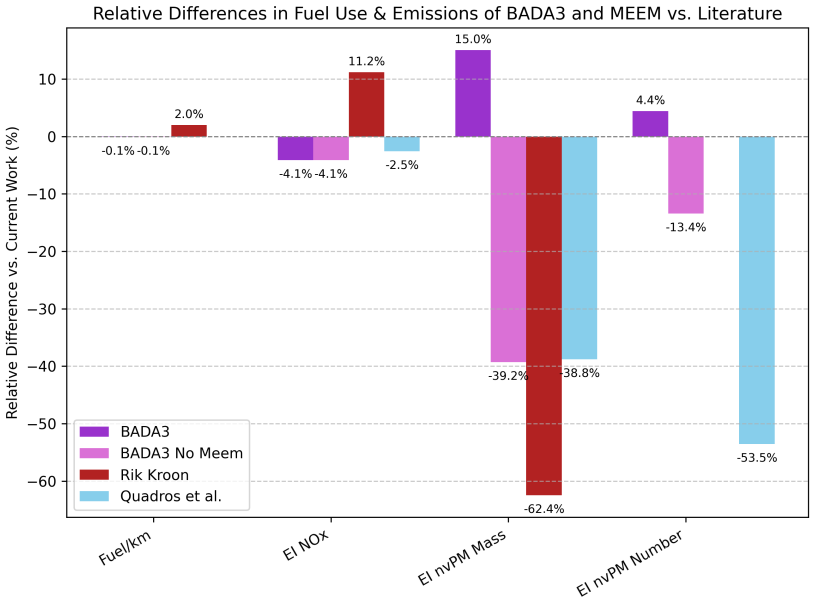

Figure 7.10: Relative differences of BADA3 and Peck et al. methods compared to current inventory and literature.

- The flight altitude distribution.
- The incorporation of weather data.
- The specific allocation of engines per flight.
- The inclusion of non-jet aircraft with engines not present in the ICAO EDB, assigned constant emission indices.

7.4. Uncertainty of the Updated Inventory Results

As discussed in section 6.1, a set of multipliers was derived from the Monte Carlo simulations for the key emissions discussed in this work. These are applied to the final emission results in order to estimate the uncertainty range for the total fleet fuel consumption and emissions. The corresponding results with 95% confidence are shown in Table 7.3.

Table 7.3: Fuel consumption and emission indices with 95% confidence intervals, compared to Teoh et al. (2024).

Descriptor	This Work	95% CI Lower	95% CI Upper	Teoh et al.
Fuel consumption per km (kg km^{-1})	5.13	4.82	5.72	4.64
EI NO_x (g kg^{-1})	15.974	14.923	17.200	15.866
EI nvPM Mass (g kg^{-1})	0.053	0.024	0.103	0.076
EI nvPM Number (x10^{15} kg^{-1})	2.52	1.30	3.42	1.00

This table illustrates the increased uncertainty related to the nvPM emission estimates. This wide spread reflects the sensitivity of nvPM estimates to model assumptions and parameter variability, reinforcing the need for a more refined method or measurement data to quantify nvPM uncertainty. As noted, the current approach lacks cruise validation data to form a proper distribution for uncertainty propagation.

The results shown in Table 7.3 are visualised, and compared to literature, in Figure 7.11. An analogous comparison for total emissions is provided in Appendix A, highlighting the comparatively large relative uncertainty associated with nvPM emission estimates.

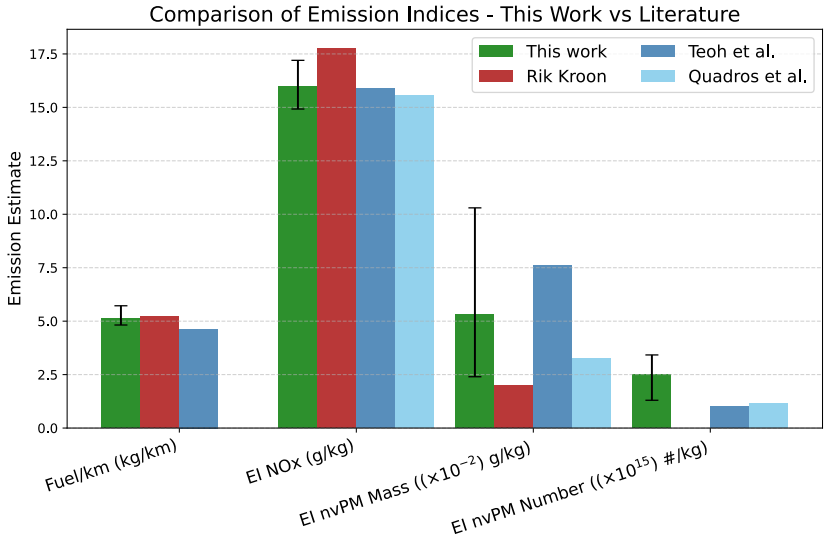

Figure 7.11: Emission indices with 95% confidence intervals compared to literature.

8

Conclusion

The goal of this study was to build upon existing emission inventories to develop a method for computationally efficient and accurate estimation of global fuel consumption and emissions. As a benchmark, an ideal emission inventory and its characteristics were outlined, and the works of Rik Kroon [30], Teoh et al. [60], and Quadros et al. [44] were compared to this benchmark. Therefore, elements from different inventories that best matched the benchmark were used as a tangible reference.

To best assess the extent to which the goal set out for this study was met, a set of research questions was posed, which we will attempt to answer here. The main research question was **To what extent can the current emission inventory be improved through the use of updated methods for performance and emission modelling, without compromising on computational efficiency?** And to answer this main question, three sub-questions were posed:

What performance model inputs are the results most sensitive to?

The sensitivity analysis demonstrated that the performance model results are most sensitive to two critical inputs: the rate of climb (ROC) threshold and the initial fuel mass estimate. It was found that the variation in output was greater when considering heavier aircraft (wake type H aircraft), as they tend to cruise longer distances. In the case of medium-sized aircraft that mostly fly short-haul, the LTO and climb phases account for a larger share of the emissions, thus the impact of changes in cruise altitude and mass is lower.

The ROC threshold has a direct influence on the determination of cruise altitude. The cruise altitude can have a large impact on the fuel burn and emissions. The largest sensitivity was seen for the nvPM emissions of wake type H aircraft, for which a ±25% change in ROC threshold led to a change of almost ±4%.

The initial fuel mass estimate, closely related to the assumed initial cruise altitude, also shows a substantial sensitivity. Variations in initial altitude assumptions directly affect the initial fuel mass estimate, with deviations causing significant changes, up to approximately 37% in wake type H aircraft. This led to an increase in fuel burn for these aircraft of up to 4%. These findings highlight the importance of precise ROC threshold selection and accurate initial fuel mass estimation within performance models.

What is the updated uncertainty of the model?

The updated uncertainty analysis, using Monte Carlo simulations, indicated that the total uncertainty in fuel consumption estimates for the emission inventory is around ±9%, with emission indices showing uncertainties in the range of ±9% for $NO_x$to ±40% and ±95% for nvPM number and nvPM mass, respectively. The large uncertainty related nvPM emissions is attributed to the poor validation data used for cruise, and the poor distribution following from it. Furthermore, the engine selection uncertainty can also have a large impact on the uncertainty of the nvPM emissions.

How do the improvements impact the global emission estimate and how do they compare to current emission inventories?

The improvements implemented in this thesis significantly impact the global emission estimates, specifically concerning nvPM emissions. Compared to existing global emission inventories for 2019, this updated model estimates total fuel burn at 250 Tg, slightly lower than Rik Kroon's inventory (254

Tg), but notably lower than those by Teoh et al. (283 Tg) and Quadros et al. (297 Tg). When analysed in terms of fuel burn per kilometre, a better measure as it removes dependency on total number of analysed flights, the current work shows a 2% lower estimate than Rik Kroon's and a 9.6% higher estimate compared to Teoh et al.

In terms of specific emission indices, the NO_x emission index in this thesis closely aligns with those of Teoh et al. and Quadros et al., differing by less than 2.5%. However, it is approximately 11% lower compared to Rik Kroon's inventory, primarily due to corrections in the performance model.

The nvPM emission results show greater discrepancies, with significant differences emerging due to methodological variations. For nvPM mass emissions, Rik Kroon and Quadros et al. report estimates lower than this study by 62% and 39%, respectively, whereas Teoh et al.'s estimate is 43% higher. For nvPM number emissions, the current work reports substantially higher values compared to Teoh et al. (-60%) and Quadros et al. (-54%), highlighting the high sensitivity and variability of nvPM emissions to methodological assumptions and engine-specific differences.

Geographically, this study captures similar emission hotspots and distribution patterns as Teoh et al., despite limitations arising from using a representative week of data. This constraint leads to under-representation of certain routes, particularly in the southern hemisphere, highlighting an area for future improvement.

Overall, to answer the main research question, the inventory can be included in the comparison table representing an ideal emission inventory for comparison, in Table 8.1.

Table 8.1: Characteristics of an Ideal Emission Inventory for the Updated Inventory

Criterion	*Updated Inventory*	*Rik Kroon*	*Teoh et al.*	*Quadros et al.*
Coverage & Resolution				
Provides global emission estimates	✓	✓	✓	✓
Provides regional resolution	✓	✓	✓	✓
Includes seasonal variation	-	-	✓	✓
Provides fleet-level emissions	✓	✓	✓	
Includes flight-specific engine assignments	✓	-	✓	-
Includes both LTO and CCD emissions	✓	✓	-	✓
Modeling & Methods				
Uses precise flight trajectories	-	-	✓	-
Incorporates weather data	-	-	✓	✓
Uses precise aircraft take-off mass	-	-	-	-
Uses up-to-date performance models	✓	-	✓	-
Uses up-to-date emission models	✓	-	✓	-

From Table 8.1, it can be seen that improvements made to the initial inventory of Rik Kroon offer more robust emission estimates due to the refined engine assignments, updated performance modelling, and updated nvPM emission modelling. Although not included in the table as it does not represent an ideal, a more accurate altitude distribution of emissions was achieved by redefining the ROC thresholds. All the while maintaining computational efficiency and flexibility within the emission inventory.

Limitations and Recommendations

There remain limitations to this work and emission inventory that can be addressed in future implementations, both in terms of coverage and modelling.

Firstly, regarding the seasonal variation and flight coverage, it was found in the geographical distribution of results that there was an under-representation of the true air traffic density in the southern hemisphere. To mitigate this, and at the same time include the seasonal variation, multiple representative weeks can be included throughout the year, representing different periods of both low- and high-season travel.

Additionally, when determining the range-based ROC thresholds, a limited sample size of between 20 and 30 flights per category is used. This can introduce sample biases, as the selected flights may not be fully representative of the entirety of flights in the representative week. Furthermore, small sample sizes are more sensitive to outliers, which can disproportionately influence the calculated thresholds. Moreover, the range categories are currently broad, which can lead to a wide spread in ROC values for the same cruise altitude. It is therefore recommended to refine the categories and/or stratify the data by wake type, and to expand the sample sets to determine more representative ROC thresholds for each category.

Next, as was shown in the sensitivity analysis, the initial fuel estimate can have an important impact on emissions. Currently, this initial fuel mass estimate may deviate largely from the actual fuel used during the flight. It is determined at a fixed cruise altitude for maximum take-off mass (MTOM). This may lead to an overestimation of the fuel used, and by applying an iterative approach to determine a converged value for initial fuel mass, the actual take-off mass of the aircraft can be better represented.

Finally, there remain large uncertainties related to the nvPM emission estimate. More measurement data, or engine simulation data, should be acquired to better assess the true uncertainty of the model when it comes to nvPM emissions.

Moreover, the uncertainty of the model is assessed based on 100 Monte Carlo simulations of 10,000 aircraft-route pairs. The entire representative week includes just over 100,000 aircraft-route pairs and is thus not fully represented. This is due to limitations in the computational resources and time available for this study. With additional resources, the entire representative week can be included, and the number of simulations can be increased to more accurately assess the higher confidence levels.

Bibliography

[1] European aviation environmental report 2016. Technical report, EEA, 2016.

[2] Joseph P. Abrahamson, Joseph Zelina, M. Gurhan Andac, and Randy L. Vander Wal. Predictive Model Development for Aviation Black Carbon Mass Emissions from Alternative and Conventional Fuels at Ground and Cruise. *Environmental Science and Technology*, 50(21):12048–12055, 11 2016.

[3] Denise Ahrens, Yoann Méry, Adrien Guénard, and Richard C. Miake-Lye. A New Approach to Estimate Particulate Matter Emissions From Ground Certification Data: The nvPM Mission Emissions Estimation Methodology. *Journal of Engineering for Gas Turbines and Power*, 145(3), 3 2023.

[4] Steven L Baughcum, Terrance G Tritz, Stephen C Henderson, and David C Pickett. Scheduled Civil Aircraft Emission Inventories for 1992: Database Development and Analysis. Technical report, NASA, 1996.

[5] Adam M. Boies, Marc E.J. Stettler, Jacob J. Swanson, Tyler J. Johnson, Jason S. Olfert, Mark Johnson, Max L. Eggersdorfer, Theo Rindlisbacher, Jing Wang, Kevin Thomson, Greg Smallwood, Yura Sevcenco, David Walters, Paul I. Williams, Joel Corbin, Amewu A. Mensah, Jonathan Symonds, Ramin Dastanpour, and Steven N. Rogak. Particle emission characteristics of a gas turbine with a double annular combustor. *Aerosol Science and Technology*, 49(9):842–855, 1 2015.

[6] Benjamin T. Brem, Lukas Durdina, Frithjof Siegerist, Peter Beyerle, Kevin Bruderer, Theo Rindlisbacher, Sara Rocci-Denis, M. Gurhan Andac, Joseph Zelina, Olivier Penanhoat, and Jing Wang. Effects of Fuel Aromatic Content on Nonvolatile Particulate Emissions of an In-Production Aircraft Gas Turbine. *Environmental Science and Technology*, 49(22):13149–13157, 10 2015.

[7] Copernicus Climate Change Service. ERA5 hourly data on single levels from 1940 to present. Technical report, Copernicus Climate Change Service (C3S) Climate Data Store (CDS), 2023.

[8] Emily Schwartz Dallara, Ilan M. Kroo, and Ian A. Waitz. Metric for comparing lifetime average climate impact of aircraft. *AIAA Journal*, 49(8):1600–1613, 8 2011.

[9] F M Dekking, C Kraaikamp, H P Lopuhaä, and L E Meester. *Modern Introduction to Probability and Statistics: Understanding Why and How*. Springer, Delft, 2005.

[10] Rebecca Katharina Dischl, Daniel Sauer, Christiane Voigt, Theresa Harlaß, Felicitas Sakellariou, Raphael Satoru Märkl, Ulrich Schumann, Monika Scheibe, Stefan Kaufmann, Anke Roiger, Andreas Dörnbrack, Charles Renard, Maxime Gauthier, Peter Swann, Paul Madden, Darren Luff, Mark Johnson, Denise Ahrens, Reetu Sallinen, Tobias Schripp, Georg Eckel, Uwe Bauder, and Patrick Le Clercq. Measurements of particle emissions of an A350-941 burning 100 % sustainable aviation fuels in cruise, 4 2024.

[11] DLR. *Research Topics in Aerospace*. Springer, Berlin, 2012.

[12] Frédéric Dobruszkes. Why do planes not fly the shortest routes? A review. *Applied Geography*, 109, 8 2019.

[13] Yadolah Dodge. *The Concise Encyclopedia of Statistics*. Springer, 2008.

[14] Andreas Döpelheuer and M. Lecht. Influence of engine performance on emission characteristics. 1998.

[15] Doug Dubois and Gerald C Paynter. "Fuel Flow Method2" for Estimating Aircraft Emissions. Technical report, SAE, 2006.

[16] Lukas Durdina, Benjamin T. Brem, Ari Setyan, Frithjof Siegerist, Theo Rindlisbacher, and Jing Wang. Assessment of Particle Pollution from Jetliners: From Smoke Visibility to Nanoparticle Counting. *Environmental Science and Technology*, 51(6):3534–3541, 3 2017.

[17] C J Eyers, P Norman, J Middel, M Plohr, S Michot, K Atkinson, and R A Christou. AERO2k Global Aviation Emissions Inventories for 2002 and 2025. Technical report, QinetiQ, Farnborough, 12 2004.

[18] FAA. Aviation Environmental Design Tool Version 2b Uncertainty Quantification Report. Technical report, 2017.

[19] A. Gettelman and C. Chen. The climate impact of aviation aerosols. *Geophysical Research Letters*, 40(11):2785–2789, 6 2013.

[20] Theresa Harlass, Rebecca Dischl, Stefan Kaufmann, Raphael Märkl, Daniel Sauer, Monika Scheibe, Paul Stock, Tiziana Bräuer, Andreas Dörnbrack, Anke Roiger, Hans Schlager, Ulrich Schumann, Magdalena Pühl, Tobias Schripp, Tobias Grein, Linda Bondorf, Charles Renard, Maxime Gauthier, Mark Johnson, Darren Luff, Paul Madden, Peter Swann, Denise Ahrens, Reetu Sallinen, and Christiane Voigt. Measurement report: In-flight and ground-based measurements of nitrogen oxide emissions from latest-generation jet engines and 100 % sustainable aviation fuel. *Atmospheric Chemistry and Physics*, 24(20):11807–11822, 10 2024.

[21] Markus Hilpert, Bernat A.dria Mora, Jian Ni, Ana M. Rule, and Keeve E. Nachman. Hydrocarbon Release During Fuel Storage and Transfer at Gas Stations: Environmental and Health Effects, 12 2015.

[22] IATA. IATA Annual Review 2020. Technical report, International Air Transport Association, 2020.

[23] IATA. Global Outlook for Air Transport A local sweet spot. Technical report, International Air Transport Association, 12 2023.

[24] International Civil Aviation Organization. Airport air quality manual. Technical report, ICAO, 2011.

[25] International Civil Aviation Organization. Airport Air Quality Manual. Technical report, ICAO, 2020.

[26] IPCC. Climate Change 2014: Synthesis Report. Contribution of Working Groups I, II and III to the Fifth Assessment Report of the
}Intergovernmental Panel on Climate Change. Technical report, IPCC, Geneva, Switzerland, 2014.

[27] IPCC. Climate Change 2023: Synthesis Report. Contribution of Working Groups I, II and III to the Sixth Assessment Report of the Intergovernmental Panel on Climate Change. Technical report, IPCC, Geneva, Switzerland, 7 2023.

[28] Christopher J. Smith, Ryan J. Kramer, Gunnar Myhre, Kari Alterskjr, William Collins, Adriana Sima, Olivier Boucher, Jean Louis Dufresne, Pierre Nabat, Martine Michou, Seiji Yukimoto, Jason Cole, David Paynter, Hideo Shiogama, Fiona M. O'Connor, Eddy Robertson, Andy Wiltshire, Timothy Andrews, Cecile Hannay, Ron Miller, Larissa Nazarenko, Alf Kirkevg, Dirk Olivi, Stephanie Fiedler, Anna Lewinschal, Chloe MacKallah, Martin Dix, Robert Pincus, and Piers M. Forster. Effective radiative forcing and adjustments in CMIP6 models. *Atmospheric Chemistry and Physics*, 20(16):9591–9618, 8 2020.

[29] Jan Klenner, Helene Muri, and Anders H. Strømman. Domestic and international aviation emission inventories for the UNFCCC parties. *Environmental Research Letters*, 19(5), 5 2024.

[30] Rik Kroon. Aviation Emission Inventory. Technical report, TUDelft, 2022.

[31] D. S. Lee, D. W. Fahey, A. Skowron, M. R. Allen, U. Burkhardt, Q. Chen, S. J. Doherty, S. Freeman, P. M. Forster, J. Fuglestvedt, A. Gettelman, R. R. De León, L. L. Lim, M. T. Lund, R. J. Millar, B. Owen, J. E. Penner, G. Pitari, M. J. Prather, R. Sausen, and L. J. Wilcox. The contribution of global aviation to anthropogenic climate forcing for 2000 to 2018. *Atmospheric Environment*, 244, 1 2021.

[32] David S. Lee, David W. Fahey, Piers M. Forster, Peter J. Newton, Ron C.N. Wit, Ling L. Lim, Bethan Owen, and Robert Sausen. Aviation and global climate change in the 21st century. *Atmospheric Environment*, 43(22-23):3520–3537, 7 2009.

[33] Liam Megill, Kathrin Deck, and Volker Grewe. Alternative climate metrics to the Global Warming Potential are more suitable for assessing aviation non-CO2 effects. *Communications Earth and Environment*, 5(1), 12 2024.

[34] Binod Neupane, Michael Jerrett, Richard T. Burnett, Thomas Marrie, Altaf Arain, and Mark Loeb. Long-term exposure to ambient air pollution and risk of hospitalization with community-acquired pneumonia in older adults. *American Journal of Respiratory and Critical Care Medicine*, 181(1):47–53, 1 2010.

[35] A Nuic and V Mouillet. USER MANUAL FOR THE BASE OF Aircraft DATA (BADA) FAMILY 4. Technical report.

[36] Angela Nuic. USER MANUAL FOR THE BASE OF AIRCRAFT DATA (BADA). Technical report, EUROCONTROL, 2004.

[37] Angela Nuic, Damir Poles, and Vincent Mouillet. BADA: An advanced aircraft performance model for present and future ATMsystems. *International Journal of Adaptive Control and Signal Processing*, 24(10):850–866, 10 2010.

[38] Bethan Owen, David S. Lee, and Ling Lim. Flying into the future: Aviation emissions scenarios to 2050, 4 2010.

[39] Jay Peck, Oluwayemisi O. Oluwole, Hsi Wu Wong, and Richard C. Miake-Lye. An algorithm to estimate aircraft cruise black carbon emissions for use in developing a cruise emissions inventory. *Journal of the Air and Waste Management Association*, 63(3):367–375, 2013.

[40] Damir Poles, Angela Nuic, and Vincent Mouillet. ADVANCED AIRCRAFT PERFORMANCE MODELING FOR ATM: ANALYSIS OF BADA MODEL CAPABILITIES. Technical report, EUROCONTROL, 10 2010.

[41] D. I.A. Poll and U. Schumann. An estimation method for the fuel burn and other performance characteristics of civil transport aircraft in the cruise. Part 1 fundamental quantities and governing relations for a general atmosphere. *Aeronautical Journal*, 125(1284):257–295, 2 2021.

[42] C. Arden Pope and Douglas W. Dockery. Health effects of fine particulate air pollution: Lines that connect. *Journal of the Air and Waste Management Association*, 56(6):709–742, 2006.

[43] Flávio D A Quadros, Mirjam Snellen, Junzi Sun, and Irene C Dedoussi. Supplemental material Global civil aviation emissions estimates for 2017-2020 using ADS-B Data. Technical report.

[44] Flávio D.A. Quadros, Mirjam Snellen, Junzi Sun, and Irene C. Dedoussi. Global Civil Aviation Emissions Estimates for 2017–2020 Using ADS-B Data. *Journal of Aircraft*, 59(6):1394–1405, 11 2022.

[45] Martin Schaefer. Development of a Forecast Model for Global Air Traffic Emissions. Technical report, DLR, 2012.

[46] Martin Schaefer and Sebastian Bartosch. IB-325-11-13 Overview on fuel flow correlation methods for the calculation of NO x , CO and HC emissions and their implementation into aircraft performance software Overview on fuel flow correlation methods for the calculation of NO X , CO and HC emissions and their implementation into aircraft performance software. Technical report, DLR, 2013.

[47] Tobias Schripp, Bruce E. Anderson, Uwe Bauder, Bastian Rauch, Joel C. Corbin, Greg J. Smallwood, Prem Lobo, Ewan C. Crosbie, Michael A. Shook, Richard C. Miake-Lye, Zhenhong Yu, Andrew Freedman, Philip D. Whitefield, Claire E. Robinson, Steven L. Achterberg, Markus Köhler, Patrick Oßwald, Tobias Grein, Daniel Sauer, Christiane Voigt, Hans Schlager, and Patrick LeClercq. Aircraft engine particulate matter emissions from sustainable aviation fuels: Results from ground-based measurements during the NASA/DLR campaign ECLIF2/ND-MAX. *Fuel*, 325, 10 2022.

[48] U Schumann. THE IMPACT OF NITROGEN OXIDES EMISSIONS FROM AIRCRAFT UPON THE ATMOSPHERE AT FLIGHT ALTITUDES-RESULTS FROM THE AERONOX PROJECT. Technical Report 12, 1997.

[49] Ulrich Schumann. Formation, properties and climatic effects of contrails. *Comptes Rendus Physique*, 6(4-5 SPEC. ISS.):549–565, 2005.

[50] David W Scott. On Optimal and Data-Based Histograms. *Biometrika Trust*, 66(3):605–610, 1979.

[51] Icao Secretariat. ICAO Standards and Recommended Practices: Annex 16, Volume II. Technical report.

[52] K. Seymour, M. Held, G. Georges, and K. Boulouchos. Fuel Estimation in Air Transportation: Modeling global fuel consumption for commercial aviation. *Transportation Research Part D: Transport and Environment*, 88, 11 2020.

[53] D Shindell, F-m Bréon, W Collins, J Fuglestvedt, J Huang, D Koch, J-f Lamarque, D Lee, B Mendoza, T Nakajima, A Robock, G Stephens, T Takemura, H Zhang, D Qin, G-k Plattner, M Tignor, SK Allen, J Boschung, A Nauels, Y Xia, V Bex, and PM Midgley. Anthropogenic and Natural Radiative Forc-ing. In: Climate Change 2013: The Physical Science Basis. Contribution of Working Group I. Technical report, IPCC, 2013.

[54] Nicholas W. Simone, Marc E.J. Stettler, and Steven R.H. Barrett. Rapid estimation of global civil aviation emissions with uncertainty quantification. *Transportation Research Part D: Transport and Environment*, 25:33–41, 2013.

[55] Marc E.J. Stettler, Adam M. Boies, Andreas Petzold, and Steven R.H. Barrett. Global civil aviation black carbon emissions. *Environmental Science and Technology*, 47(18):10397–10404, 9 2013.

[56] Junzi Sun, Luis Basora, Xavier Olive, Martin Strohmeier, Matthias Schafer, Ivan Martinovic, and Vincent Lenders. OpenSky Report 2022: Evaluating Aviation Emissions Using Crowdsourced Open Flight Data. In *AIAA/IEEE Digital Avionics Systems Conference - Proceedings*, volume 2022-September. Institute of Electrical and Electronics Engineers Inc., 2022.

[57] Junzi Sun and Irene Dedoussi. Evaluation of Aviation Emissions and Environmental Costs in Europe Using OpenSky and OpenAP †. *Engineering Proceedings*, 13(1), 2021.

[58] Junzi Sun, Jacco M. Hoekstra, and Joost Ellerbroek. OpenAP: An open-source aircraft performance model for air transportation studies and simulations. *Aerospace*, 7(8), 8 2020.

[59] Roger Teoh, Zebediah Engberg, Marc Shapiro, Lynnette Dray, and Marc E J Stettler. Supporting Information A high-resolution Global Aviation emissions Inventory based on ADS-B. Technical report.

[60] Roger Teoh, Zebediah Engberg, Marc Shapiro, Lynnette Dray, and Marc E.J. Stettler. The high-resolution Global Aviation emissions Inventory based on ADS-B (GAIA) for 2019-2021. *Atmospheric Chemistry and Physics*, 24(1):725–744, 1 2024.

[61] Roger Teoh, Ulrich Schumann, Edward Gryspeerdt, Marc Shapiro, Jarlath Molloy, George Koudis, Christiane Voigt, and Marc E.J. Stettler. Aviation contrail climate effects in the North Atlantic from 2016 to 2021. *Atmospheric Chemistry and Physics*, 22(16):10919–10935, 8 2022.

[62] C L Townsend and R L Maynard. Effects on health of prolonged exposure to low concentrations of carbon monoxide. *Occupational and Environmental Medicine*, 59:708–711, 2002.

[63] James H Ware, Lawrence A Thibodeau, Frank E Speizer, Steven Colome, and Benjamin G Ferris. Assessment of the Health Effects of Atmospheric Sulfur Oxides and Particulate Matter: Evidence from Observational Studies. Technical report, 1981.

[64] D. K. Wasiuk, M. H. Lowenberg, and D. E. Shallcross. An aircraft performance model implementation for the estimation of global and regional commercial aviation fuel burn and emissions. *Transportation Research Part D: Transport and Environment*, 35:142–159, 3 2015.

A

Total Emission Values

Table A.1: Final total fuel and emission estimates of updated inventory compared to literature.

Descriptor	Current Work	Rik Kroon [30]	Teoh et al. [60]	Quadros et al. [44]
Fuel burn (Tg)	250	254	283	297
CO_2 (Tg)	788	801	892	937
CO (Gg)	599	697	400	814
HC (Gg)	49.8	65.9	33.9	42.6
NO_x (Tg)	3.99	4.51	4.49	4.62
nvPM mass (Gg)	13.3	5.28	21.4	9.68
nvPM number(#)	6.29E+26	-	2.83E+26	3.47E+26

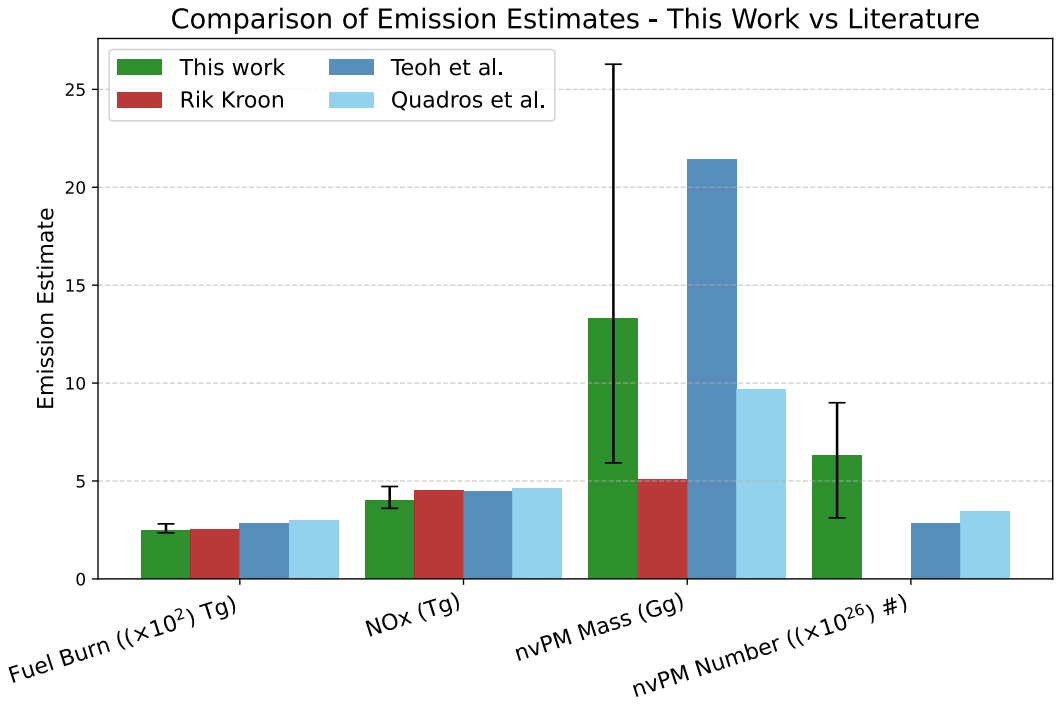

Figure A.1: Emission estimates with 95% confidence intervals compared to literature.

B

Emission Distribution Plots

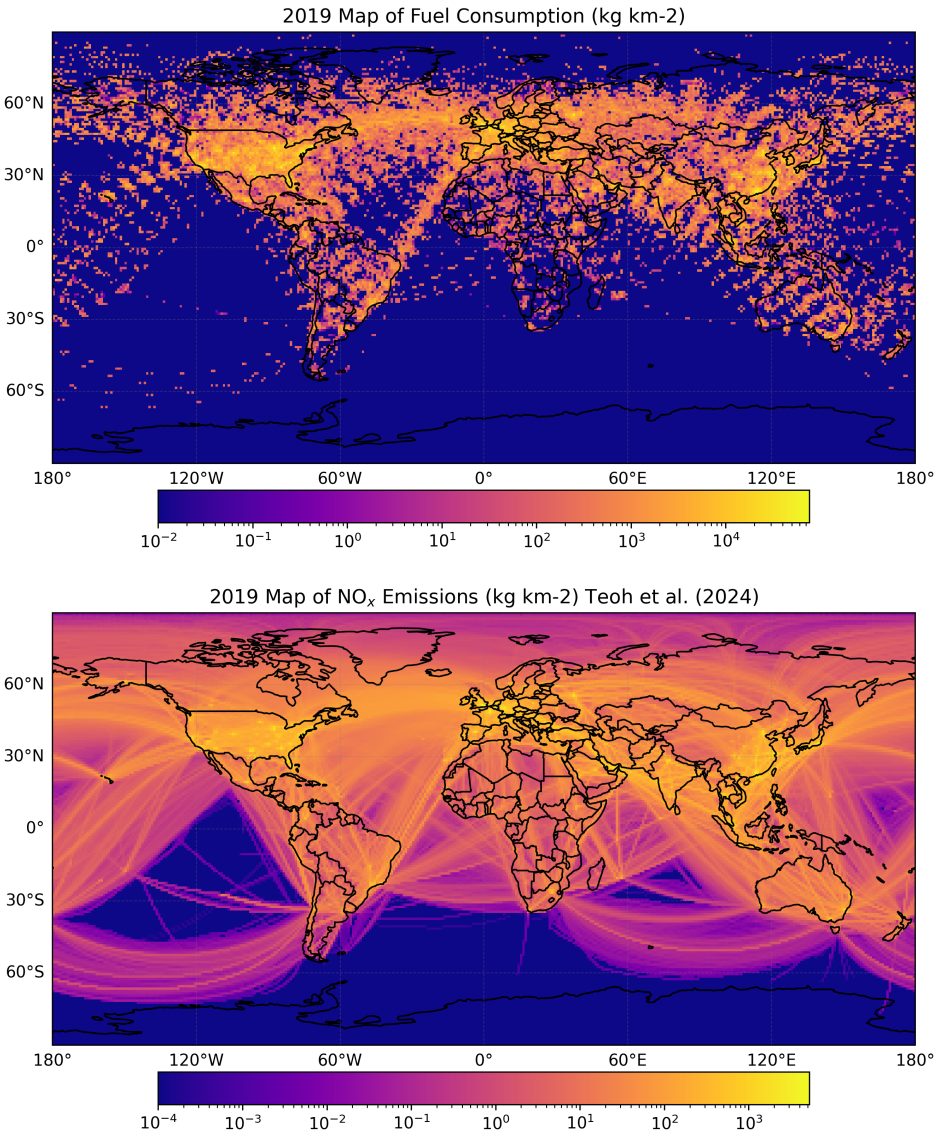

Figure B.1: Geographical distribution of fuel consumption estimate from this inventory (top) and the inventory of Teoh et al. (bottom).

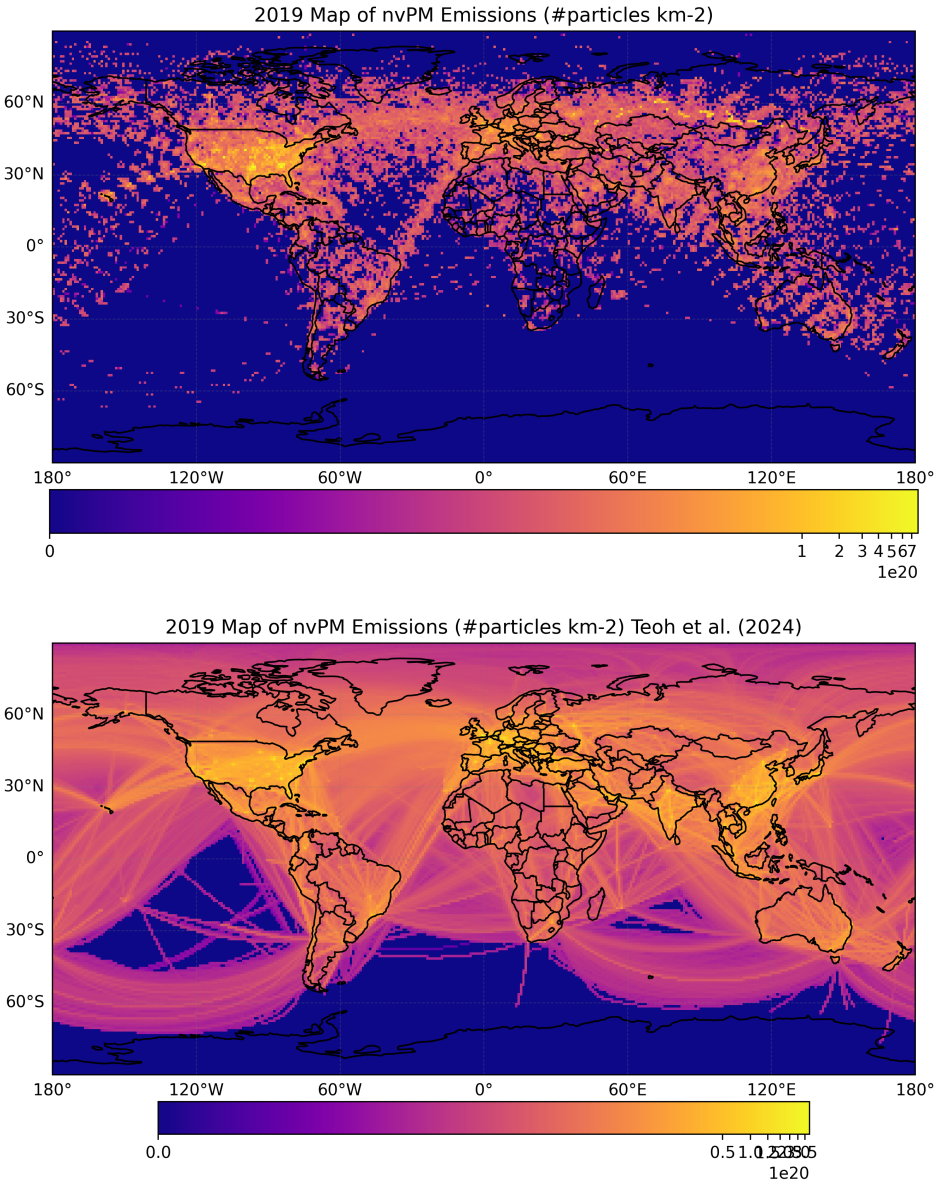

Figure B.2: Geographical distribution of nvPM number emissions estimate from this inventory (top) and the inventory of Teoh et al. (bottom).